From Elementary Excitations to Microstructures:

The thermodynamics of metals and alloys across length scales

Thesis by

Michael Edward Manley

In Partial Fulfillment of the Requirements

for the Degree of

Doctor of Philosophy

California Institute of Technology

Pasadena, California

2001

(Defended April 25, 2001)

To the memory of my father, Edward W. Manley

Acknowledgements

I would like to begin by acknowledging the love and support I have received from my wife, Ann, without which I could never have made it this far. Ann, who has been by my side the whole the way through graduate school, has made it all worthwhile. I would also like to acknowledge the love support I received from my entire family, both by blood and by my marriage into the Lee family.

It gives me great pleasure to acknowledge the guidance and support I received from my advisor, Brent Fultz. Despite the fact that I spent the second half of my graduate student career at Los Alamos, he managed to boost my spirits and my scientific career through regular communication. I would also like to acknowledge support from the entire Fultz group and from the Materials Science option. In particular, I received essential help with theoretical and/or experimental ideas from Channing Ahn, Peter Bogdanoff, and Laura Nagel. Special thanks go to my officemates, Haein Choi-Yim, Jay Hannan, and Nathan Good, who where always willing to listen.

This would not be complete without acknowledging the guidance and support I received from my mentor at Los Alamos National Laboratory, Rob McQueeney. There were many others who helped at Los Alamos including, Jim L. Smith, Larry Hults, Dan Thoma, and Jason Cooley. I also benefited from the expertise of scientist at various user facilities including, Ray Osborn of Argonne National Laboratory, Lee Robertson of Oak Ridge National Laboratory, and Craig Brown and Dan Neumann of NIST.

Abstract

An experimental investigation has been made into the components that determine the phase stability of metals and alloys. Contributions were found to be important across many length scales from electronic excitations to atomic vibrations and finally microstructural strains at the continuum level. The metals and alloy that have been studied are U, Ce, and Pd_3V.

Time-of-flight (TOF) inelastic neutron scattering spectra were measured on the three crystalline phases of uranium at temperatures from 50 K to 1213 K. Phonon density of states (DOS) curves were obtained from these spectra. For the α-phase, a large decrease in phonon energies with increasing temperature was observed over the entire temperature range. Analysis of the vibrational power spectrum showed that the phonon softening originates with continuous softening of a harmonic solid, as opposed to vibrations in anharmonic potentials. Without anharmonicty, it must be that thermal excitations of the electronic structure are changing the interatomic forces. State-of-the-art electronic band structure calculations are based on the assumption that temperature effects on the electronic structure can be neglected when compared to volume effects (where the volume effects are just a manifestation of anharmonicity). The present results turn that problem upside down by showing that temperature effects are actually more important than volume effects. Vibrational entropies of the phase transitions were $(S^{\beta}\text{-}S^{\alpha})_{vib}$ = (0.15±0.1) k_B/atom and $(S^{\gamma}\text{-}S^{\beta})_{vib}$ = (0.36±0.1) k_B/atom. The former accounts for about 35% and the latter 65% of the total entropy of the phase transition. The remaining entropy must be electronic.

TOF inelastic neutron scattering spectra were measured on cerium at temperatures near the fcc (γ) to bcc (δ) transition temperature. Phonon DOS curves were extracted from data acquired over a wide range of momentum transfers. A large softening of the phonon DOS was found in going from γ-cerium to δ-cerium, and this accounts for an increase in vibrational entropy of (0.71 ± 0.05) k_B/atom. To be consistent with the latent heat of the γ-δ transition, this increase in vibrational entropy must be accompanied by a large decrease in electronic entropy. The results not only confirm the recent discovery of a significant electronic contribution to the γ-δ transition but also suggest that it may be twice as large as previously reported.

TOF inelastic neutron scattering spectra were measured on β-cerium (dhcp) and γ-cerium (fcc) near the phase transition temperature. Phonon densities of states (DOS) were extracted from the TOF spectra. A softening of the phonon DOS occurs in the transition from β-cerium to γ-cerium, accounting for an increase in vibrational entropy of $\Delta S_{vib}^{\gamma-\beta}$ = (0.09 ± 0.05) k_B/atom. Crystal field levels were extracted from the magnetic scattering for both phases. The entropy calculated from the crystal field levels and a fit to calorimetry data from the literature was significantly larger in β-cerium than γ-cerium below room temperature. The difference was found to be negligible at the experimental phase transition temperature. There was a contribution to the specific heat from Kondo spin fluctuations that was consistent with the quasielastic magnetic scattering, but the difference between phases was negligible. To be consistent with the latent heat of the β–γ transition, the increase in vibrational entropy at the phase transition may be accompanied by a decrease in electronic entropy not associated with

the crystal field splitting or spin fluctuations. At least three sources of entropy need to be considered for the β–γ transition in cerium.

Differences in the heat capacity and thermal expansion of cubic (fcc-disordered) and tetragonal (DO_{22}-ordered) Pd_3V were measured from 40 K to 315 K. Below 100 K the heat capacity difference was consistent with harmonic vibrations. At higher temperatures, however, the data show significant anharmonic effects. Measurements of elastic constants, densities, and thermal expansion showed that the anharmonic volume expansion contribution (C_p–C_V) could account for only about one-third of this anharmonic heat capacity difference. The remainder may originate with elastic and plastic deformation of the polycrystalline microstructure. Strain energy from anisotropic thermal contractions of grains in the tetragonal ordered phase contributes to the heat capacity, but some of this strain energy is eliminated by plastic deformation. The vibrational entropy difference of disordered and ordered Pd_3V was estimated to be $S^{dis} - S^{ord} = (+0.035 \pm 0.001)\ k_B$/atom at 300 K, with 70% of this coming from anharmonic effects.

The microstructural contribution to the heat capacity of α–uranium was determined by measuring the heat capacity difference between polycrystalline and single crystal samples from 77 K to 320 K. When cooled to 77 K and then heated to about 280 K, the uranium microstructure released (3±2) J/mol of strain energy. On further heating to 300 K the microstructure absorbed energy as the microstructure began to redevelop microstrains. Neutron diffraction measurements on polycrystals predicted the total strain energy stored in

the microstructure to be (3.7±0.5) J/mol at 77 K and (1±0.5) J/mol at room temperature in good agreement with the calorimetry.

List of publications

(1) "Phonon densities of states of γ-cerium and δ-cerium measured by inelastic neutron scattering,"

J. L. Robertson, H. N. Frase, P. Bogdanoff, M. E. Manley, B. Fultz, and R. J McQueeney,

Phil. Mag. Letters, Vol. 79, No. 5, 297 (1999).

(2) "Dynamic magnetic susceptibility of γ-cerium, β-cerium and low density Cerium alloys,"

R. J. McQueeney, M. E. Manley, B. Fultz, G. Kwei, R. Osborn, and P. Bogdanoff,

Phil. Mag. B, in press.

(3) "Heat capacity and microstructure of ordered and disordered Pd_3V,"

M. E. Manley, B. Fultz, and L. J. Nagel,

Phil. Mag. B., Vol. 80, 1167 (2000).

(4) "Phonon densities of states of γ-cerium and δ-cerium measured by TOF inelastic neutron scattering,"

M. E. Manley, J. L. Robertson, B. Fultz, R. J. McQueeney, and D. A. Neumann,

Phil. Mag. Letters, Vol. 80, 591 (2000).

(5) "Large harmonic softening of the phonon density of states of uranium,"

M. E. Manley, B. Fultz, R. J. McQueeney, C. M. Brown, W. L. Hults, J. L. Smith, D. J. Thoma, R. Osborn, and J. L. Robertson,

Phys. Rev. Letters, Vol. 86, 3076 (2001).

(6) "On the nature of the phonon softening in α-uranium,"

M. E. Manley,

Los Alamos Science, Number 26, 202 (2000).

(7) "Vibrational and electronic entropy of γ-cerium and β-cerium measured by inelastic neutron scattering,"

M. E. Manley, R. J. McQueeney, B. Fultz, G. Kwei, R. Osborn, and P. Bogdanoff,

to be submitted.

(8) "Microstructural strain and strain energy of α-uranium determined by neutron diffraction and calorimetry,"

M. E. Manley, B. Fultz, J. Cooley, W. L. Hults, J. L. Smith,

to be submitted.

Contents

List of Figures

Chapter One Introduction

Predicting the most stable phase of a solid at a given temperature, pressure, and composition is a long standing goal of materials science. Predictions are important because in many cases, direct measurements of the most stable phase are impractical or impossible. Consider all possible combinations of elements, extreme pressures and temperatures. Only by understanding the relevant degrees of freedom (vibrational, configurational, electronic, magnetic, etc.) can phase stability be predicted reliably in regions of thermodynamic parameter space where data are unavailable.

Theoretical and experimental work has been done in recent years to improve the reliability of first principle phase stability predictions for the d-electron transition metals and their alloys [1-4]. In some cases these advances have even proved useful in engineering applications [5, 6]. However, for the f-electron bonded systems there has been less success because the underlying physics is poorly understood. The electronic structure of f-electron bonded systems remains one of the last frontiers in solid-state physics. Results presented in Chapter 2 of this thesis shows why a theoretical understanding must account for how thermally induced electronic excitations affect interatomic interactions. State-of-the-art electronic structure theory treats atomic interactions and electronic excitations as separate problems. This is the first example presented in this thesis of how working across length scales sheds new light on problems.

The importance of vibrational entropy to solid-state phase transitions has become well established over the past decade. Considerable experimental [3,7-11] and theoretical [11-

16] work has gone into investigating the vibrational entropy of phase transitions in metallic alloys. In alloys, the vibrational entropy is often compared with a significant configurational contribution. For elements, however, entropy can only be vibrational, electronic and magnetic. In Chapters 2 and 3 it is shown that vibrational entropy makes a significant contribution to phase transitions in uranium and cerium.

Electronic entropy is not normally expected to make a significant contribution to high temperature phase transitions. Electronic entropy is, therefore, often neglected in phase stability calculations. However, results presented in Chapters 2 and 3 show that the electronic entropy of uranium and cerium is thermodynamically significant. Furthermore, a detailed study of the electronic contribution in two phases of cerium (Chapter 3.3) shows that the electronic entropy of cerium can be broken down into a contribution from localized electrons and spatially extended conduction band electrons. The conduction band contribution comes from the usual excitations of electrons across the Fermi-energy. Localized electronic states of an atom, which are degenerate for isolated atoms, are split into various crystal field levels when the atom is in a crystal. It is shown that changes in crystal symmetry at phase transitions can change the crystal field entropy. In addition, hybridization of the spins of the localized f-electrons with the conduction band electrons causes Kondo-type fluctuations of the localized f-electron spins. The effect on the measured crystal field levels is a smearing out of the states in energy. It can also be viewed as an enhancement of the effective mass of the conduction band electrons. Regardless of the view taken, this hybridization results in another contribution to the electronic entropy.

A scale often neglected in first principle phase stability calculations is the microstructural scale. Nevertheless, a connection can be made between the anharmonic components of thermal vibrations and the elastic energy stored in a polycrystalline microstructure. The anharmonic component of vibrations leads to thermal expansion. If a polycrystalline microstructure is made up of crystallites having anisotropic thermal expansion, then changes in temperature lead to a build-up or release of microstructural strain energy due to the forces that crystallites exert on one another. As shown in Chapters 4 and 5, the elastic microstructural contribution can make an important contribution to the thermodynamics. Additionally, the forces between crystallites can become large enough to induce plastic deformation. The onset of plastic deformation cuts off the buildup of elastic strain energy stored in the microstructure. Plasticity causes irreversible changes in the state of the strain energy stored in the microstructure.

Figure 1.1 shows the different areas of research that should be combined to develop a more complete understanding of the thermodynamics of metals and alloys. The top two experimental areas are dealt with in this thesis. As will be demonstrated, it is the connections between these areas that turn out to be most interesting and promising for future work. For clarity the interesting connections are highlighted at the beginning of each chapter with a few italic sentences. Also the chapters are ordered so that the problems move from the smallest scales (electronic and atomic) to the largest scales (from atomic to microstructural). It is hoped that this thesis will help stimulate further study between the areas shown in Figure 1.1. Specifically, as the computational methods become more accessible, it would make sense for a single research group to complete the triangle. It is my belief that this will lead to a rapid

development of accurate equations of state of metals and alloys and hence more reliable predictions of materials properties.

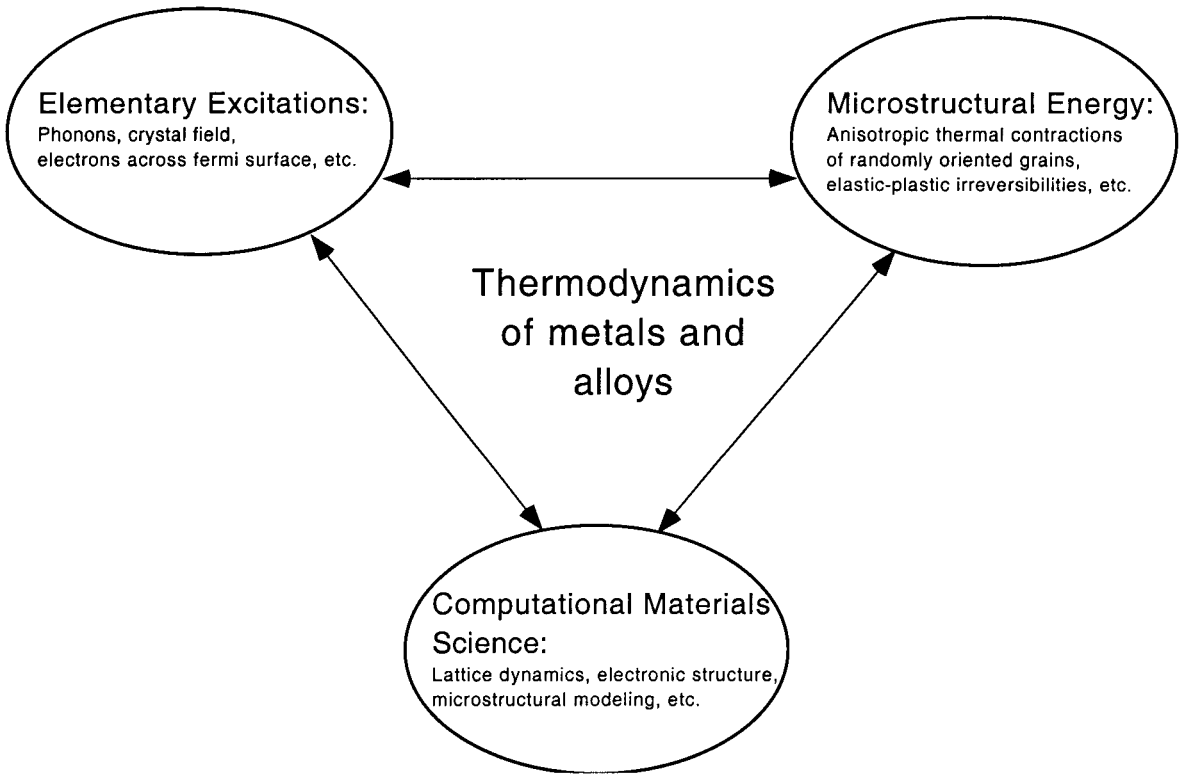

Figure 1.1. This diagram shows how efforts in many different disciplines can be used to improve our understanding of the thermodynamics of metals and alloys. The work of this thesis bridges the top of this diagram.

References

[1] J. Okamoto, C. Ahn, and B. Fultz, in *Proceedings of the XIIth Inernational Congress for Electron Microscopy*, edited by L. D. Peachey and D. B. Williams (San Francisco Press, San Francisco, 1990), p. 50.

[2] L. Anthony, J. K. Okamoto, and B. Fultz, Phys. Rev. Lett. **70**, 1128 (1993).

[3] L. Anthony, L. J. Nagel, J. K. Okamoto, and B. Fultz, Phys. Rev. Lett. **73**, 3034 (1994).

[4] F. Ducastelle, *Ordering and Phase Stability in Alloys* (North Holland, 1991) p. 471.

[5] G. Ceder, Mol. Simul. 12, 141 (1994).

[6] G. Ceder, M.K. Aydinol, and A.F. Kohan, Comp. Mater. Sci. **8** 161 (1997).

[7] B. Fultz, L. Anthony, L. J. Nagel, R. M. Nicklow, and S. Spooner, Phys. Rev. B **52**, 3315 (1995).

[8] L. J. Nagel, B. Fultz, and J. L. Robertson, Phil. Mag. B **50**, 7291 (1997).

[9] J. L. Robertson, H. N. Frase, P. D. Bogdanoff, M. E. Manley, B. Fultz and R. J. McQueeney, Phil. Mag. Lett. **79**, 297 (1999).

[10] M. E. Manley, B. Fultz, L. J. Nagel, Phil. Mag. B **80**, 1167 (2000).

[11] M. E. Manley, R. J. McQueeney, J. L. Robertson, B. Fultz, and D. A. Neumann, Phil. Mag. Lett. **80**, 591 (2000).

[12] A. F. Guillermet and G. Grimvall, J. Phys. Chem. Solids **53**, 105 (1992).

[13] S. J. Clark and G. J. Ackland, Phys. Rev. B **48**, 10899 (1993).

[14] G. D. Garbulsky and G. Ceder, Phys. Rev. B **53**, 8993 (1996).

[15] A. Van de Walle, G. Ceder, and U. V. Waghmare, Phys. Rev. Lett. **80**, 4911 (1998).

[16] C. Wolverton, V. Ozolins, and A. Zunger, Phys. Rev. B **57**, 4332 (1998).

Chapter Two The nature of vibrational softening in uranium

In this chapter the study of vibrational softening in uranium reveals a surprising connection between electronic excitations and atomic vibrations. Thus, we begin with a study connecting electronic to atomic scale contributions to the thermodynamics of uranium.

2.1 Introduction

Although first known for its unusual nuclear properties, uranium exhibits several unusual solid-state properties that may originate with electronic instabilities. The thermally induced softening of the phonon density-of-states (DOS) for most elements originates with anharmonicity [1, 2]. For the actinides, however, a distinction between the normal anharmonic softening and harmonic softening arising from a temperature-dependent harmonic potential has been suggested [3]. In a detailed assessment of the thermodynamic data on the six crystalline phases of Pu, it was concluded that the anharmonic and electronic contributions to the equation of state could not be separated [4]. The origin of this phonon softening is a fundamental issue for the equation of state. In this Chapter we use the power spectrum of atom motions to show that the thermal softening of the phonon DOS in α-U originates with the weakening of force constants in a harmonic solid, as opposed to the typical softening in an anharmonic potential. Temperature alters the electronic structure sufficiently to change the lattice dynamics. This chapter also addresses the entropy of phonons, and by deduction the entropy of electrons, for the three low-pressure phases of uranium metal.

Previous lattice dynamics studies on uranium have been performed at room temperature and below [5, 6], motivated in part by the discovery of several charge density wave transitions at low temperatures [7, 8]. Independently, there has been a recent interest in the vibrational entropy contribution to the high temperature phase stability of metals and alloys [9-11], motivated by the discovery that vibrational entropy plays a larger role in phase stability than previously expected [12]. Other experimental and theoretical work has shown that electronic contributions to the entropies of high temperature phase transitions can also be significant [13-15].

Diffraction measurements on α-U at ambient pressure have shown that the Debye temperature decreases dramatically with increasing temperature [3, 16]. This softening is consistent with decreases in the elastic constants [17, 18]. Specifically, the Debye temperature was expressed by $\theta \cong (306 - 0.158T)$ K, where T is temperature [3]. The magnitude of this softening suggests that the Debeye temperature decreases by about 40% between 300 and 940 K. This corresponds to a vibrational entropy of $\Delta S = 3k_B \ln(\theta_{300K}/\theta_{940K})$ = 1.5 k_B/atom beyond that of the room temperature phonon DOS.

The usual thermodynamic argument for thermal expansion is that although thermal expansion generates elastic energy, a larger crystal has lower phonon frequencies and hence a larger vibrational entropy. The quasiharmonic approximation assumes these vibrations to be those of a harmonic solid [1]. In this approximation the entropy due to phonon softening equals the entropy from volume expansion, consistent with the thermodynamic prediction

$$S_p - S_V = \int_{300K}^{940K} \frac{C_p - C_V}{T} dT = 9B_T V\alpha^2\,(640K) = 0.16\ k_B/\text{atom}, \quad (1)$$

where the bulk modulus B = 100 GPa, the molar volume V = 12.49 cm^3/mol, and the linear thermal expansion coefficient α = 1.39 x 10^{-5}/K are all values at 300 K [8]. (Their temperature dependencies are not expected to change the results below by more than a few percent.) The entropy change of 1.5 k_B/atom predicted with Debye-Waller factors is thus about an order-of-magnitude larger than what is expected from the volume expansion. This substantial inconsistency suggests that the phonon softening has a different origin.

2.2 Experimental

All experiments used uranium powder of 99.84% purity with particle sizes of 20-100 μm. For safety reasons the particles were passivated with a uranium dioxide surface layer that made up about 20% of the total volume. For the high temperature measurements about 80 g was loaded into a vanadium can of 1.5 cm diameter and 7.6 cm in length. The sample can was mounted in a furnace that was kept under high vacuum throughout all measurements. Neutron energy gain spectra were measured at high temperatures with the FCS time-of-flight spectrometer at the NIST Center for Neutron Research. The spectrometer was operated with an incident neutron energy of 3.55 meV (λ = 4.8 Å). Spectra were obtained on α-U at 300 K, 433 K, 645 K, and 913 K; β-U at 1013 K; and γ-U at 1113 K and 1213 K. For the low temperature measurements, 157 g of powder was loaded into a 6 x 10 cm flat plate aluminum can of depth ~2.5 mm. The low temperature measurements were performed with the LRMECS time-of-flight chopper spectrometer at the Intense Pulsed Neutron Source at the Argonne National Laboratory. The spectrometer was operated with

incident neutron energies of 25 meV and 15 meV, and measurements were made at 50 K, 250 K, and 300 K. The data were corrected for empty can scattering and time-independent backgrounds, and summed over a wide range of scattering angles to obtain the phonon density of states. Some weak inelastic intensity from the uranium dioxide surface layer was observed. However, since most of this intensity was at energies higher than the uranium phonon cut off energy (~15 meV), it was easily fit and subtracted from the elemental uranium scattering using a previously measured uranium dioxide phonon density of states [19]. The scattering from the oxide accounted for about 10% of the total inelastic intensity in the energy range of the metallic uranium phonon DOS.

2.3 Results and analysis

2.3.1 Multiphonon correction and the phonon DOS

After the empty can runs were subtracted from each data set, the resulting spectra contains both 1-phonon and multiphonon contributions. To separate out the 1-phonon density of states the incoherent multiphonon scattering was iteratively determined to all orders in the harmonic approximation (the calculations in this section were performed on Mathcad using the files in Appendix A). The procedure involved using a trial phonon DOS to calculate the mean square atomic displacement $\langle u^2 \rangle$ and time dependent self correlation function defined as

$$G(t) = \int_{-\infty}^{\infty} d\omega \frac{Z(\omega)}{\omega} n(\omega) e^{-i\omega t}, \tag{2.1}$$

where $Z(\omega)$ is the phonon density of states and $n(\omega)$ is the thermal occupancy factor. Then this was used to calculate the total incoherent dynamic structure factor summed over the detector angle (2θ) range

$$\overline{S}^{inc}_{calc}(\omega) = \sum_{\theta} \frac{1}{2\pi\hbar} e^{-Q^2(\theta,\omega)\langle u^2\rangle} \int_{-\infty}^{\infty} dt e^{-i\omega t} e^{\hbar^2 Q^2(\theta,\omega) G(t)/2M} \left[e^{-\frac{t^2}{2}\left(\frac{\Delta E(\omega)}{2\hbar}\right)^2} \right] \quad (2.2)$$

where

$$Q(\theta,\omega) = \sqrt{\frac{2M}{\hbar^2}\left(2E - \hbar\omega - 2E\sqrt{1-\frac{\hbar\omega}{E}}\cos(2\theta)\right)}, \quad (2.3)$$

and M is the neutron mass. The anisotropy in the Debye-Waller factor, $\langle u^2 \rangle$, was neglected because the resulting errors can be shown to be negligible (see Appendix B). The expression in square brackets in Equation 2.2 includes a gaussian instrument energy resolution of variable width, $\Delta E(\omega)$, and minimizes cut off errors in the numerical Fourier transform.

By expanding the exponential in Equation 2.2 containing $G(t)$, the incoherent single phonon and elastic scattering was determined. This was subtracted from the total scattering to give the multiphonon-angle-averaged dynamic structure factor

$$\overline{S}^{inc}_{m,calc} = \overline{S}^{inc}_{calc} - \overline{S}^{inc}_{0,calc} - \overline{S}^{inc}_{1,calc}. \quad (2.4)$$

Although the previous result was calculated for incoherent scattering, the angle-averaged result is also a good approximation for the multiphonon coherent scattering since the interference terms in the coherent cross section cancel each other to a large extent.[18] The coherent elastic scattering is just a delta function convoluted with the instrument energy resolution and thus was easily fit and subtracted.

The measured total dynamical structure factor minus the elastic peak was averaged over the detector angles, 2θ, and scaled to match $\overline{S}^{inc}_{calc}(\omega) - \overline{S}^{inc}_{0,calc}(\omega)$. Then the multiphonon part, Equation 2.4, was subtracted to give an estimate of the one phonon scattering plus a small nearly constant background (~5%) from multiple scattering. After a background subtraction this was then used to determine a new phonon DOS that was in turn used to recalculate the multiphonon contribution. The procedure was repeated until the phonon DOS converged to within statistical errors (three iterations).

Figure 2.1 shows the phonon DOS obtained from the measured spectra. The agreement of the FCS and the LRMECS results at 300 K is encouraging. Both measurements show intensity at ~15 meV above the phonon DOS calculated (DOS_calc) from the force constant model of Crummet, et al. [5]. With this model, the fully coherent one phonon scattering function, $S_1(|\boldsymbol{Q}|, \omega)$, was calculated and summed over the appropriate kinematic $|\boldsymbol{Q}|$ and ω ranges for each instrument. The results for both LRMECS (LRMECS_calc) and FCS (FCS_calc) show that the difference is not a result of insufficient Q-sampling. In the α–phase there is a redistribution of intensity in the main features at ~8 and ~12 meV, with the higher energy peak gaining extra weight with increasing temperature. These features also show an overall decrease of about 1 meV per 200 K.

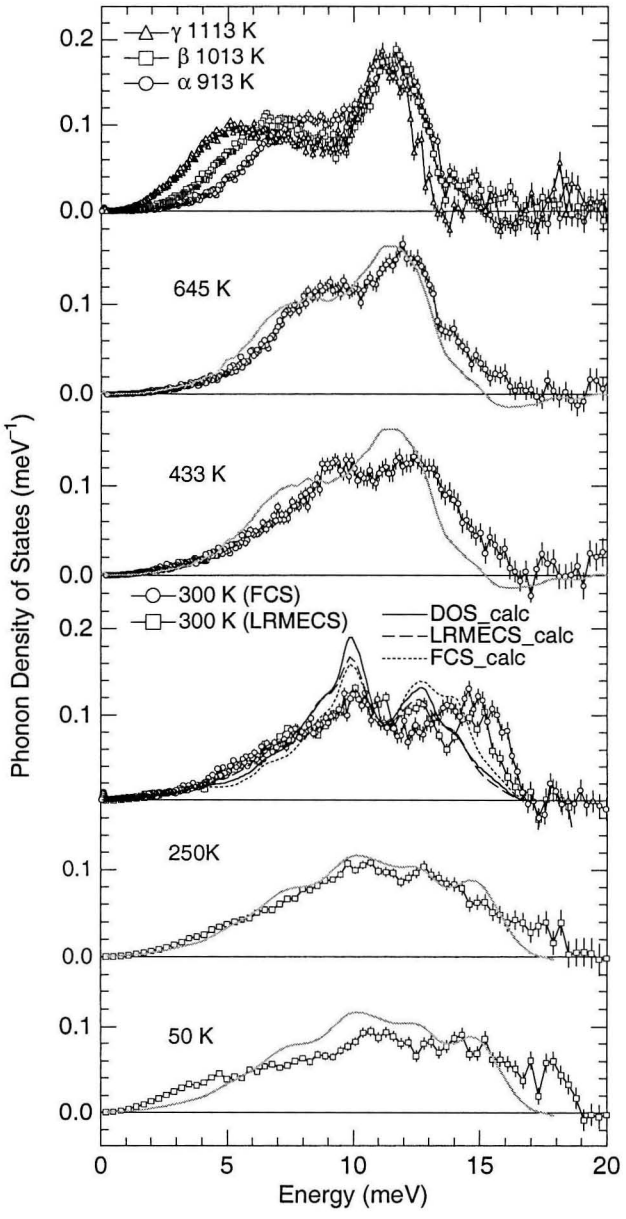

Figure 2.1. The phonon density of states of uranium. Data from 300 K and above were obtained from spectra acquired with the Fermi-Chopper Spectrometer (FCS) at the NIST. Data from 300 K and below were measured on the Low Resolution Medium Energy Chopper Spectrometer (LRMECS) at ANL. The curves labeled DOS_calc, LRMECS_calc and FCS_calc were all calcuated from the force constant model of Crummett et al. [5] as described in the text. The 913 K α-uranium DOS is superimposed on all curves above 300 K and the 300 K data is superimposed on all curves below 300 K. The three solid state phases, orthorhombic (α), tetragonal (β) and body centered cubic (γ) are compared at the top.

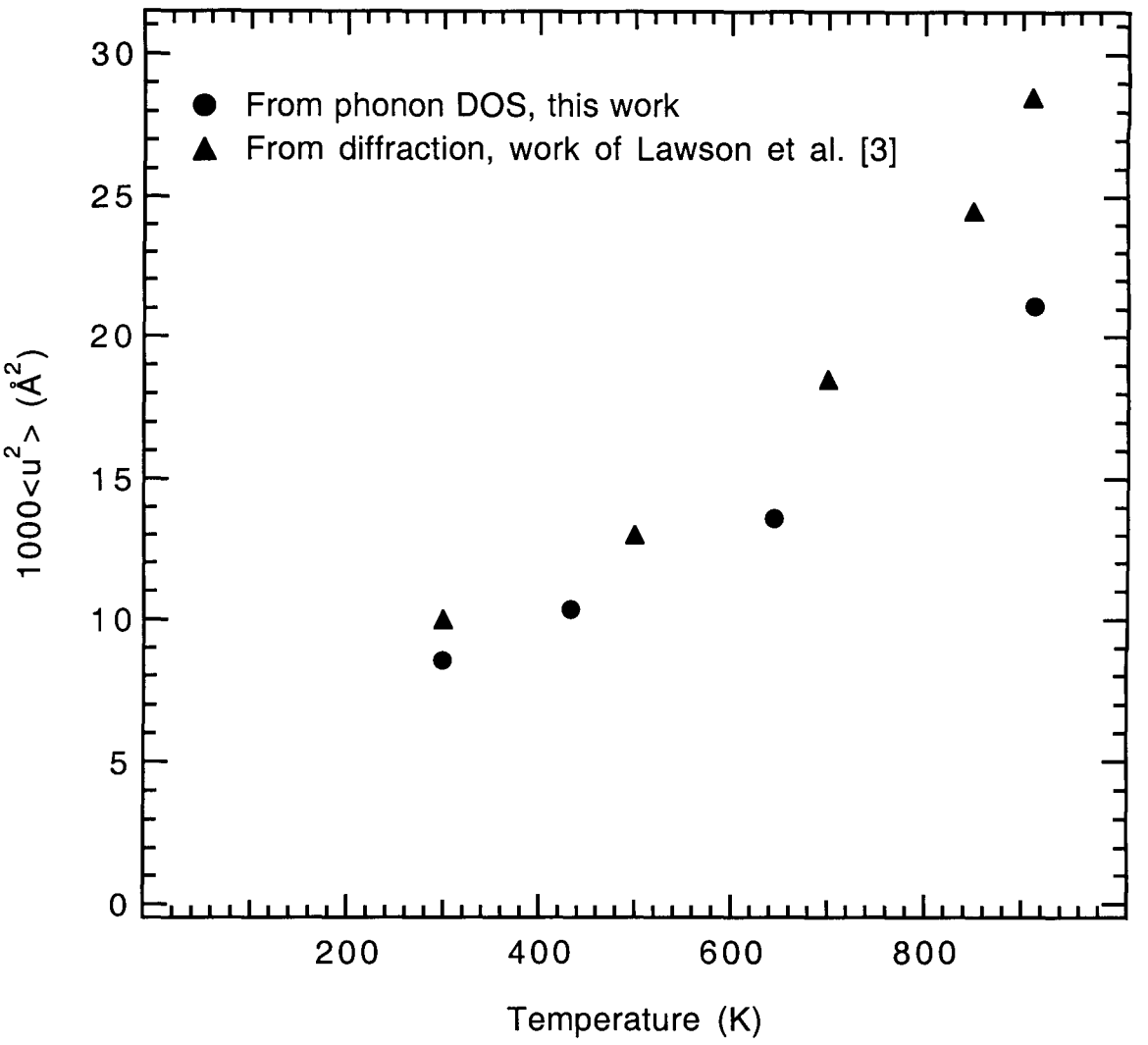

Figure 2.2. Comparison of the mean square displacement calculated from phonon DOS in this work and that determined by diffraction by Lawson et al. [3].

The temperature dependence of the $\langle u^2 \rangle$ calculated from the phonon DOS was compared to those determined from diffraction [3], Figure 2.2. The results from diffraction show a more rapid increase with temperature and hence a larger vibrational softening. The diffraction results predict that the Debye temperature decreases by about 40% from room to the transition temperature where, as our phonon DOS shows, it may only be 30%.

At low temperatures there is a broadening of the features in the phonon DOS that could arise from shortened phonon lifetimes, perhaps related to the charge density wave (CDW) transition at 43 K [8]. At low temperatures a broad peak appears in the phonon DOS at about 4 meV. This could support Yamada's suggestion [20] that a whole sheet of the phonon spectrum starts to soften as the temperature is lowered toward the 43 K CDW transition — a single soft mode would involve a volume in reciprocal space too small to be observed in the phonon DOS.

2.3.2 Testing for harmonic behavior

Most standard methods of measuring vibrations in solids are immediately interpreted in terms of harmonic models. However, it turns out that a more general view can be taken. In the case of inelastic neutron scattering, the dynamical structure factor can be interpreted in terms of the mean-square power spectrum and hence the potential energy can be extracted. For a single component system the incoherent scattering function, $S_i(\boldsymbol{Q}, \omega)$, is given by the Fourier transform of the autocorrelation function [21]

$$S_i(\boldsymbol{Q},\omega) = \frac{1}{2\pi\hbar}\int_{-\infty}^{\infty}\frac{1}{N}\sum_{j=1}^{N}\left\langle e^{-i\boldsymbol{Q}\cdot\boldsymbol{r}_j(0)}e^{i\boldsymbol{Q}\cdot\boldsymbol{r}_j(t)}\right\rangle e^{-i\omega t}dt, \tag{2.5}$$

where $\boldsymbol{r}_j$ represents the instantaneous atomic position of atom j. By taking the classical limit, the scattering from a crystal in an arbitrary orientation with respect to $\boldsymbol{Q}$ can be simplified by expanding the exponentials in powers of the magnitude of $\boldsymbol{Q}$, denoted Q, and integrating over time, t. Taking the classical approximation

$$\left\langle e^{-iQr_{Q,j}(0)}e^{iQr_{Q,j}(t)}\right\rangle = \left\langle e^{iQ(r_{Q,j}(t)-r_{Q,j}(0))}\right\rangle, \tag{2.6}$$

where $r_{Q,j}$ is the projection of $\boldsymbol{r}_j$ along the direction of $\boldsymbol{Q}$. Then expanding in the small Q limit,

$$\left\langle e^{iQ(r_{Q,j}(t)-r_{Q,j}(0))}\right\rangle \cong 1+iQ\left(\left\langle r_{Q,j}(t)\right\rangle-\left\langle r_{Q,j}(0)\right\rangle\right)-\frac{1}{2}Q^2\left(\left\langle {r_{Q,j}}^2(t)\right\rangle+\left\langle {r_{Q,j}}^2(0)\right\rangle\right)$$
$$+Q^2\left\langle r_{Q,j}(0)r_{Q,j}(t)\right\rangle \tag{2.7}$$

Subtituting (2.7) into (2.5) the following results are found per atom (j):

First term:

$$\frac{1}{2\pi\hbar}\int_{-\infty}^{\infty}e^{-i\omega t}dt=\frac{\delta(\omega)}{\hbar}. \tag{2.8}$$

Second term:

$$\begin{aligned}
&\frac{iQ}{2\pi\hbar}\int_{-\infty}^{\infty}\left(\left\langle r_{Q,j}(t)\right\rangle-\left\langle r_{Q,j}(0)\right\rangle\right)e^{-i\omega t}dt\\
&=\frac{iQ}{2\pi\hbar}\left[\int_{-\infty}^{\infty}\int_{-\beta}^{\beta}r_{Q,j}(\tau-t)d\tau e^{-i\omega t}dt-\left\langle r_{Q,j}(0)\right\rangle 2\pi\delta(\omega)\right]\\
&=\frac{iQ}{2\pi\hbar}\left[\left(\int_{-\infty}^{\infty}r_{Q,j}(t')e^{i\omega t'}dt'\right)\int_{-\infty}^{\infty}e^{-i\omega\tau}d\tau-\left\langle r_{Q,j}(0)\right\rangle 2\pi\delta(\omega)\right]\\
&=\frac{iQ}{2\pi\hbar}\left[R_{Q,j}(0)2\pi\delta(\omega)-\left\langle r_{Q,j}(0)\right\rangle 2\pi\delta(\omega)\right]\\
&=0
\end{aligned} \tag{2.9}$$

The change of variables $t' = \tau - t$ was used. $R_{Qj}(0)$ is the Fourier transform of $r_{Qj}(t)$ evaluated at zero frequency. It equals $<r(0)>$ because both $<r(0)>$ and $R_{Qj}(0)$ give the deviation from a zero average (if there is such a deviation). To get the delta function, the limit on the time average, β, was set to infinity.

Third term:

$$
\begin{aligned}
&-\frac{Q^2}{4\pi\hbar}\int_{-\infty}^{\infty}\left(\left\langle {r_{Q,j}}^2(t)\right\rangle+\left\langle {r_{Q,j}}^2(0)\right\rangle\right)e^{-i\omega t}dt \\
&=-\frac{Q^2}{4\pi\hbar}\left[\left(\int_{-\infty}^{\infty}{r_{Q,j}}^2(t')e^{i\omega t'}dt'\right)\int_{-\beta}^{\beta}e^{-i\omega\tau}d\tau+\left\langle {r_{Q,j}}^2(0)\right\rangle 2\pi\delta(\omega)\right] \\
&=-\frac{Q^2}{\hbar}\left\langle {r_{Q,j}}^2(0)\right\rangle\delta(\omega)
\end{aligned}
\tag{2.10}
$$

Last term:

$$
\begin{aligned}
&\frac{Q^2}{2\pi\hbar}\int_{-\infty}^{\infty}\left\langle r_{Q,j}(0)r_{Q,j}(t)\right\rangle e^{-i\omega t}dt=\frac{Q^2}{2\pi\hbar}\int_{-\infty}^{\infty}\int_{-\beta}^{\beta}r_{Q,j}(\tau)r_{Q,j}(\tau-t)d\tau e^{-i\omega t}dt \\
&=\frac{Q^2}{2\pi\hbar}\left(\int_{-\infty}^{\infty}r_{Q,j}(t')e^{i\omega t'}dt'\right)\int_{-\beta}^{\beta}r_{Q,j}(\tau)e^{-i\omega\tau}d\tau=\frac{Q^2}{2\pi\hbar}\left|R_{Q,j}(\omega)\right|^2
\end{aligned}
\tag{2.11}
$$

Combining terms gives the classical incoherent scattering function at low Q:

$$
S_i(\boldsymbol{Q},\omega)\cong\frac{1}{N}\sum_{j=1}^{N}\left(\frac{\delta(\omega)}{\hbar}\left(1-Q^2\left\langle r_{Q,j}^2(0)\right\rangle\right)+\frac{Q^2}{2\hbar}\left|R_{Q,j}(\omega)\right|^2+\ldots\right), \tag{2.12}
$$

For a powder, Equation (2.12) is averaged over all orientations. Hence, the modulus square power spectrum averaged over all atoms (j's) and directions, denoted $|R(\omega)|^2$, can be extracted from the measurement. The average potential energy per degree of freedom can then be determined by integrating the average power spectrum using

$$
\langle U\rangle=\frac{1}{2}M\int\omega^2|R(\omega)|^2d\omega, \tag{2.13}
$$

where M is the mass of the vibrating atom. In the case of harmonic phonons in the high temperature limit, the power spectrum is related to the phonon density of states by

$$
\frac{1}{2}M\omega^2|R(\omega)|^2=\frac{1}{2}k_BTZ(\omega). \tag{2.14}
$$

Integrating both sides with respect to ω gives the expected result that $<U>_h=k_BT/2$. This result holds true even if the harmonic potential is temperature dependent, i.e., if the temperature dependence of the phonon DOS is the result of a continuous change in a harmonic potential. Equipartition of potential and kinetic energy is expected for harmonic, but not anharmonic oscillators. If the potential is constant and the softening originates with anharmonicity, the potential energy can be expressed as

$$\langle U\rangle_{anh} \cong \frac{1}{2}k_BT + A(k_BT)^2 + B(k_BT)^3 + \ldots, \qquad (2.15)$$

where the coefficients A and B can be related to true anharmonic terms in the interatomic potential.

The Q-summed one phonon scattering function, $S_1(|\boldsymbol{Q}|,\omega)$, was used with Eqs. 2.12 and 2.13 to calculate a quantity proportional to $<U>$ for α-U at the four highest temperatures. The result shown in Figure 2.3 was scaled so the points at the lowest temperatures were at the harmonic energy $k_BT/2$. Anharmonicity will appear as a nonlinearity in a plot of $<U>$ vs. T. For comparison, attempts were made to calculate the temperature dependence of the potential energy of a Morse and a Lennard-Jones potential. Because the vibrational softening in α-U is so large in spite of its low thermal expansion and elastic stiffness, no standard potential could match all properties. For the potential energy curves labeled "Lennard-Jones" and "Morse_1" in Figure 2.3, the correct thermal expansion, nearest-neighbor distance and vibrational softening (~30%) were used with an elastic stiffness about two times too large. For the potential labeled "Morse_2" in Figure 2.3, the correct elastic stiffness was used, but the thermal expansion was about two times too large. The nonlinearity in the plot of $<U>$ vs. T is obviously too large in all cases. The phonon

softening in α-U occurs while the potential remains primarily harmonic. Evidently the interatomic force constants are temperature dependent. Since the force constants originate with the sensitivity of the electronic energy to atom displacements, it follows that thermal excitations of the electronic states are altering the force constants. This contradicts the assumption, used in state-of-the-art band structure calculations, that temperature effects can be neglected compared to anharmonic volume effects.

The thermodynamic implications of harmonic versus anharmonic phonon soften can be understood most easily by considering Figure 2.4. The upper graph in Figure 2.4(b) shows a harmonic oscillator with the same energy E and mean-square displacement $<u^2>$ as those of the anharmonic oscillator shown in Figure 2.4(a). However, the anharmonic phase-space trajectory contains a smaller area (lower graph). In the classical limit ($k_B T >>$ the energy spacing of quantum states), a unit of phase-space area of size $\Delta p \Delta u \sim \hbar$ (set by the uncertainty principle) contains one quantum state. A system exploring the smaller area therefore accesses fewer quantum states. Entropy is proportional to the log of the number of accessible quantum states. Thus, the anharmonic oscillator with its smaller phase-space area must have less vibrational entropy. A similar argument can be made for equal temperatures, but in that case the entropies are the same and the energy of the anharmonic oscillator is larger. At equal temperatures, the vibrational free energy ($F = E - TS$) is therefore larger for the anharmonic oscillator. Although this is an oversimplification of a real solid, it does make it clear that distinguishing between anharmonic and harmonic behavior is essential to understanding the vibrational part of the equation of state of uranium (more on the differences between harmonic and anharmonic oscillators can be found in Appendix C).

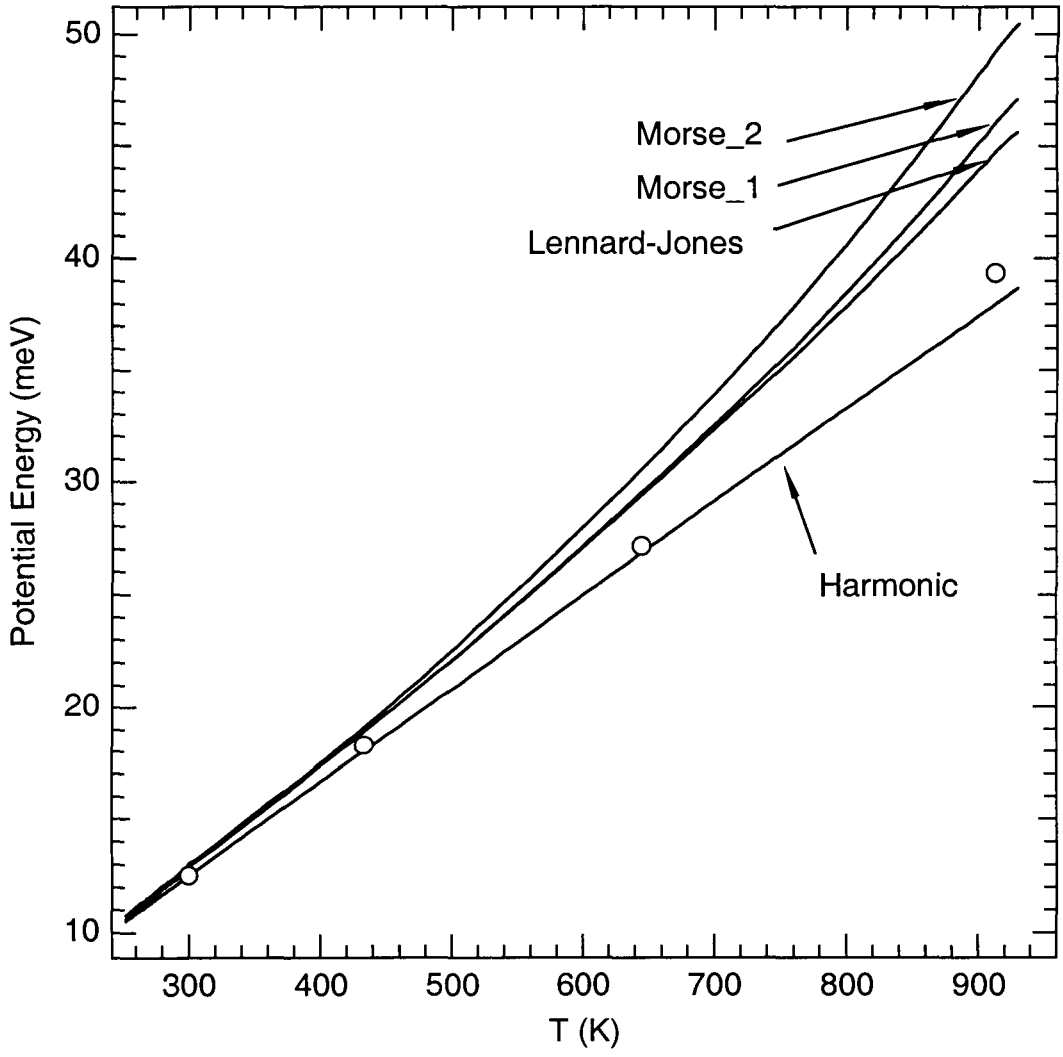

Figure 2.3. Vibrational potential energy of α-uranium (O). The Lennard-Jones, Morse_1 and Morse_2 curves were calculated from potentials described in the text. The Harmonic curve is the result for a harmonic potential in the classical limit.

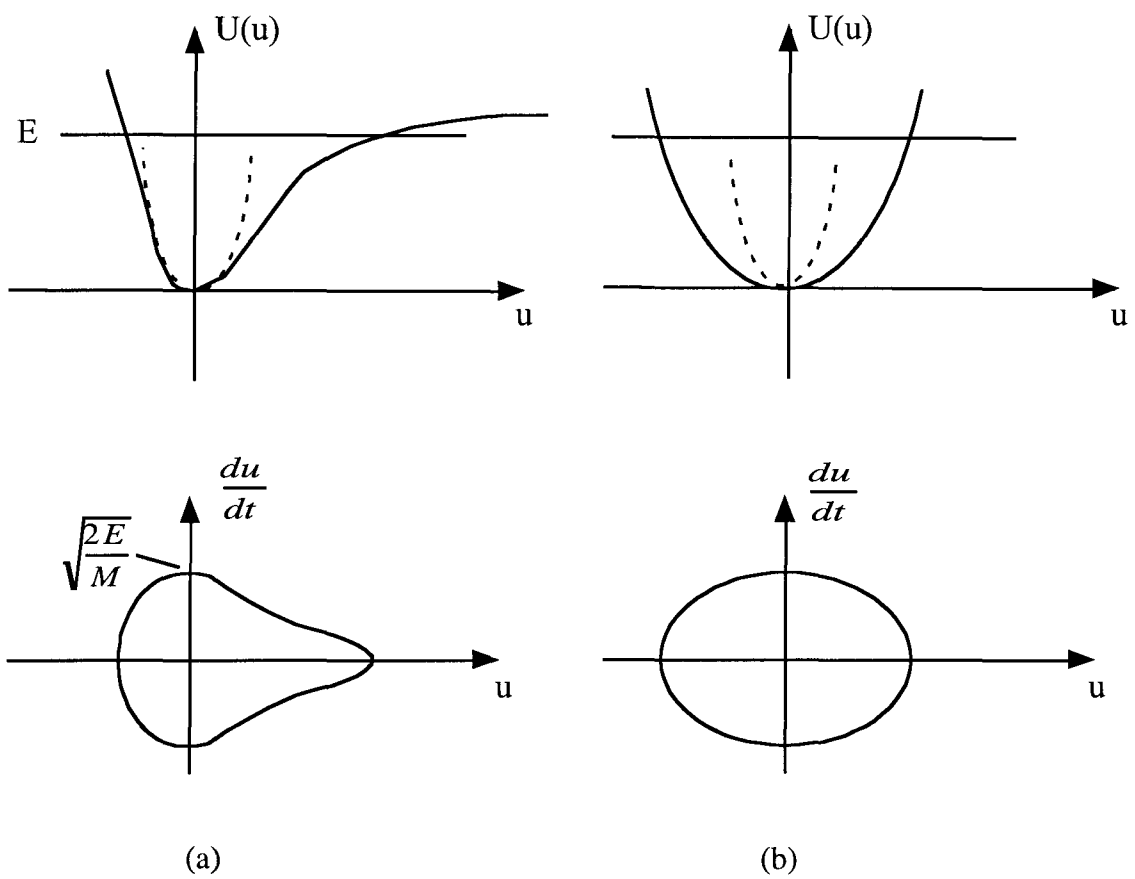

Figure 2.4. Anharmonic versus Harmonic Oscillators. Potentials (top) and phase space (bottom) are shown for (a) anharmonic and (b) harmonic oscillators with the same mean square displacement $<u^2>$ and energy E. The dashed lines represent the potentials seen at low energy (in (a) because the anharmonicity becomes small and in (b) because the potential is temperature dependent). The anharmonic phase space contains a smaller area and hence has a lower vibrational entropy.

The phonon density-of-states of the three solid-state phases of uranium, orthorhombic (α), tetragonal (β) and body-centered cubic (γ) are compared at the top of Figure 2.1. The γ-uranium phonon density of states was statistically the same at 1113 K and 1213 K, showing no evidence of the thermal softening seen in α-phase. The β-phase is not stable over a sufficient temperature range to obtain the temperature dependence of its phonon DOS. The change in phonon DOS at each phase transition accounted for vibrational entropy changes of $(S^{\beta}\text{-}S^{\alpha})_{vib}$ = +(0.15±0.1) k_B/atom and $(S^{\gamma}\text{-}S^{\beta})_{vib}$ = + (0.36±0.1) k_B/atom. The errors arise mainly from the uncertainty in the Q-sampling estimated from the difference between the calculated phonon DOS (DOS_calc) and calcuated Q-summed coherent scattering for the FCS instrument (FCS_calc). Both these values are significantly smaller than the total entropy obtained from latent heat measurements; $(S^{\beta}\text{–}S^{\alpha})_{tot}$ = (0.35–0.37) k_B/atom and $(S^{\gamma}\text{–}S^{\beta})_{tot}$ = (0.54–0.55) k_B/atom [22, 23]. The remaining entropy of the phase transitions must be electronic in origin. Not only does the phonon softening disappear in the high temperature γ-phase, but it does so with a large increase in electronic entropy. Electronic entropy evidently makes a major contribution to the stabilities of the β- and γ-phases.

2.4 Concluding remarks

The results from these experiments were surprising for a number of reasons. Perhaps the greatest significance of these results is that they challenge the way we think about the strength of interatomic bonding. With very few exceptions, changes in the stiffness of a bond between two atoms or a collection of atoms in a crystal are first related to atomic distances

and/or the symmetry of the arrangement in the case of a crystal. It is typical to ignore the effects of electronic thermal excitations that are found to be so important in the present work.

The temperature dependence of the electronic structure in α-U plays a major role in its thermodynamics, being comparable to the phonon entropy and overwhelming the usual anharmonic behavior. Present state-of-the-art electronic band structure calculations used to predict properties such as phonon frequencies are based on the assumption that thermal effects on the electronic structure can be neglected when compared to volume effects. The actinides, however, show the need for more sophisticated treatments of the role of temperature on interatomic interactions. Specifically, the affect of the excited electronic states on the atomic vibrations must be understood.

References

[1] A. A. Maradudin and A. E. Fein, Phys. Rev. **128**, 2589 (1962).

[2] T. H. K. Barron, J. G. Collins, and B. K. White, Adv. Phys. **29**, 609 (1980).

[3] A. C. Lawson, B. Martinez, J. A. Roberts, B. I. Bennett, and J. W. Richardson, Jr., Phil. Mag. B **80**, 53 (2000).

[4] D. C. Wallace, Phys. Rev. B **58**, 15433 (1998).

[5] W. P. Crummett, H. G. Smith, R. M. Nicklow, and N. Wakabayashi, Phys. Rev. B. **19**, 6028 (1979).

[6] H. G. Smith, N. Wakabayshi, W. P. Crummett, R. R. Nicklow, G. H. Lander, and E. S. Fisher, Phys. Rev. Lett. **44**, 1612 (1980).

[7] J. C. Marmeggi and A. Delapalme, Physica **120B**, 309 (1980).

[8] G. H. Lander, E. S. Fisher, and S. D. Bader, Adv. Phys. **43**, 1 (1994).

[9] J. Okamoto, C. Ahn, and B. Fultz, in *Proceedings of the XIIth Inernational Congress for Electron Microscopy*, edited by L. D. Peachey and D. B. Williams (San Francisco Press, San Francisco, 1990), p. 50.

[10] L. Anthony, J. K. Okamoto, and B. Fultz, Phys. Rev. Lett. **70**, 1128 (1993).

[11] L. Anthony, L. J. Nagel, J. K. Okamoto, and B. Fultz, Phys. Rev. Lett. **73**, 3034 (1994).

[12] F. Ducastelle, *Ordering and Phase Stability in Alloys* (North Holland, 1991) p. 471.

[13] J. L. Robertson, H. N. Frase, P. Bogdanoff, M. E. Manley, B. Fultz, and R. J. McQueeney, Phil. Mag. Lett. **79**, 297 (1999).

[14] M. E. Manley, R. J. McQueeney, J. L. Robertson, B. Fultz and D. A. Neumann, Phil. Mag. Lett. **80**, 591 (2000).

[15] E. G. Moroni, G. Grimvall, and T. Jarlborg, Phys. Rev. Lett. 76, 2758 (1996).

[16] A. C. Lawson, J. A. Goldstone, B. Cort, R. I. Sheldon, and E. M. Foltyn, J. of Alloys and Compounds **213/214**, 426 (1994).

[17] E. S. Fisher, Argonne National Lab. Report ANL-6096,TID-4500 (1960).

[18] E. S. Fisher, J. Nucl. Materials **18**, 39 (1966).

[19] G. Dolling, R. A. Cowley, and A. D. B. Woods, Canadian J. of Phys. **43**, 1397 (1965).

[20] Y. Yamada, Phys. Rev. B. **47**, 5614 (1993).

[21] G. L. Squires, *Introduction to the Theory of Thermal Neutron Scattering* (Dover Publications, Mineola, NY, 1978) p. 61.

[22] F. L. Oetting, M. H. Rand, and R. J. Ackermann, *The Chemical Thermodynamics of Actinide Elements and Compounds, Part 1 The Actinide Elements* (International Atomic Energy Agency, Vienna, 1976) p. 16.

[23] *Rare Metals Handbook*, edited by C. A. Hampel (Reinhold Publishing Corporation, London, 1961) p. 609.

Chapter Three Vibrational and electronic entropy of cerium

In this chapter it is shown that, like for uranium, the electronic entropy of cerium is thermodynamically significant. It is also shown that the electronic contribution can be separated into a localized and delocalized electron contribution. The connection between scales in this chapter is the coupling of the localized and delocalized electronic states.

3.1 Introduction

Cerium is endowed with several fascinating structural phase transitions between its six known solid phases shown in Figure 3.1. For example, there is a structural phase transition, driven by increasing pressure or decreasing temperature, where fcc γ-cerium collapses to fcc α-cerium with a 15% volume reduction at room temperature. This difference in volume becomes smaller at higher temperatures, and cerium is the only element to exhibit a critical point in a solid-solid phase transition. Because cerium undergoes a significant change in valence in the γ-α transition (from 3 towards 4), recent studies have focused on the electronic structure of cerium [1-6].

In this chapter the vibrational and electronic entropy of two solid-state cerium transitions are studied. The first (Section 3.1) concerns the high temperature fcc (γ) to bcc (δ) transition. In this transition the electronic contribution is deduced by comparing the measured phonon contribution to the total determined from the latent heat of the transformation. In the second case (Section 3.2) the electronic contribution to the dhcp (β) to fcc (γ) transition is considered in more detail. Specifically, electronic entropy contributions from crystal field

splitting, Kondo spin fluctuations, and the usual excitations at the Fermi energy are treated separately.

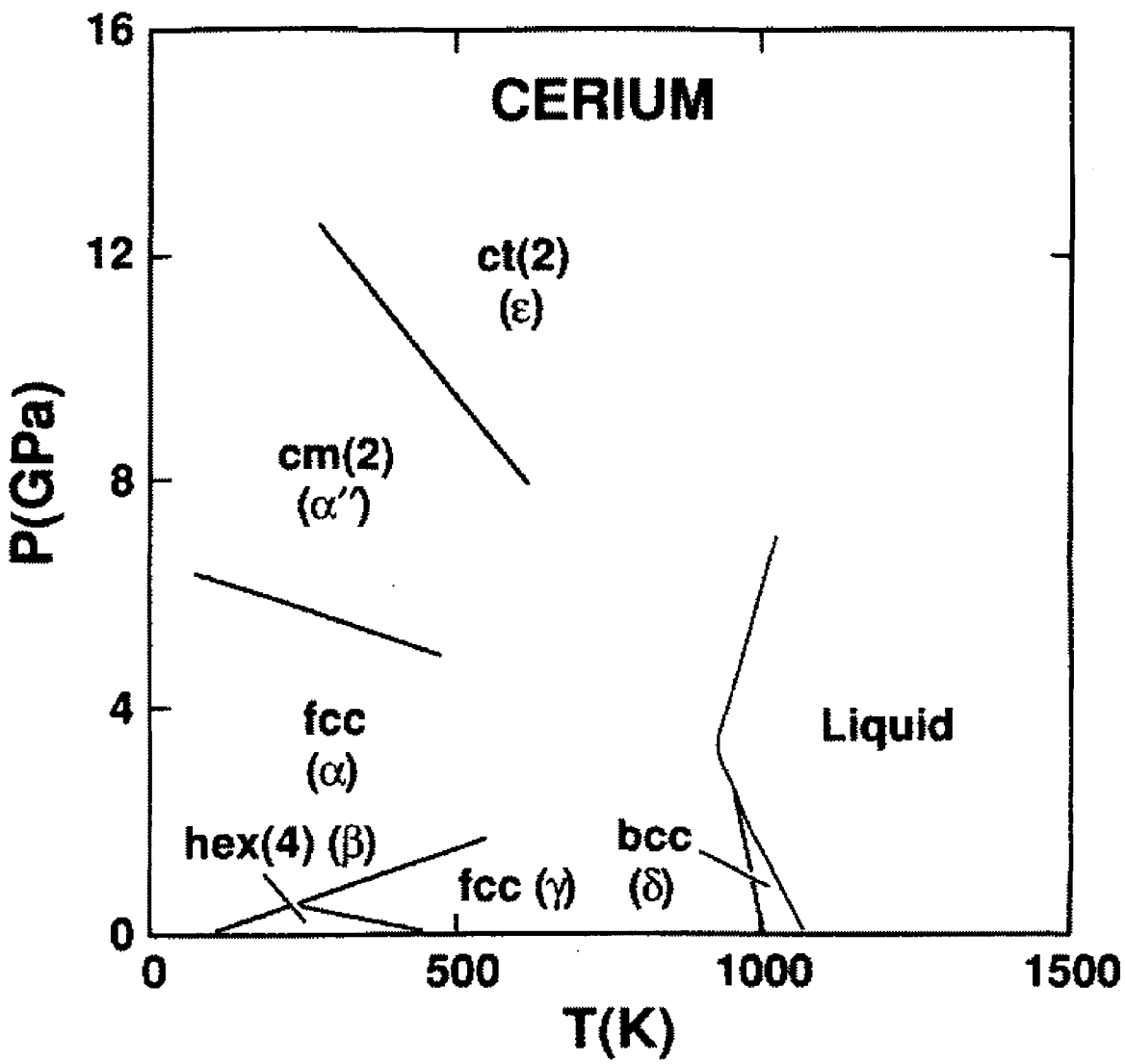

Figure 3.1. Phase diagram of cerium.

3.2 Phonon densities of states of γ-cerium and δ-cerium measured by TOF inelastic neutron scattering

3.2.1 Introduction

Recent inelastic neutron scattering measurements on the HB3 triple axis spectrometer at ORNL were used to estimate the vibrational entropy of the cerium fcc (γ) to bcc (δ) transition [7]. The value found, $\Delta S_{vib}^{\delta-\gamma}$= (0.51 ± 0.05) k_B/atom, was so large that a thermodynamically significant electronic entropy of the opposite sign was required to explain the latent heat. This was an important result because electronic entropy is not normally expected to make a significant contribution to a high temperature structural phase transition. There was, however, some uncertainty in the result. Because cerium scatters neutrons coherently, interference of the neutron wave function modulates the inelastic scattering intensity as a function of momentum transfer (Q). Thus, to determine a phonon DOS it is necessary to sum over all Q in the Brillouin zone. The uncertainty in the triple axis experiments came from the fact that only three or five values of Q were used to estimate the sum. The work of this section on the cerium fcc (γ) to bcc (δ) transition was performed to check the result using a time of flight (TOF) instrument that allows a sum to be taken over a wide range of Q.

3.2.2 Experimental

Cerium metal of 99.9% purity was obtained from Johnson-Matthey. Under an inert atmosphere, the metal ingot was cut up into pieces of typically 1 g mass. About 35 g was

loaded into a vanadium can of 1.5 cm diameter and 7.6 cm in length. The sample can was mounted in a furnace that was kept under high vacuum throughout all measurements.

The high temperature measurements were performed on the Fermi Chopper Time-of-Flight spectrometer at the NCNR (NIST Center for Neutron Research). The spectrometer was operated with an incident neutron energy of E = 3.55 meV (λ = 4.8 Å). Spectra were obtained at 795 K (γ), 984 K (γ), 1006 K (δ), and 1021 K (δ). The phases were verified by observing the first few diffraction peaks in the elastic scattering. Empty can runs were also performed at each temperature.

3.2.3 Data analysis

The empty can runs were subtracted from each data set. Then the incoherent multiphonon scattering was iteratively determined to all orders using the procedure described in Section 2.3.1 of this thesis. On the FCS instrument there were 40 detector angles that went from 35° to 135°. The Q sampling of the Brillouin zone is compared to that of the triple axis measurements of Robertson et al. [7] in Figure 3.2. Clearly, the TOF measurements in the present study give a more complete sum over the Brillouin zone. The out-of-plane Q projections not shown in Figure 3.2 improve the Q-sampling of both the TOF and triple-axis measurements.

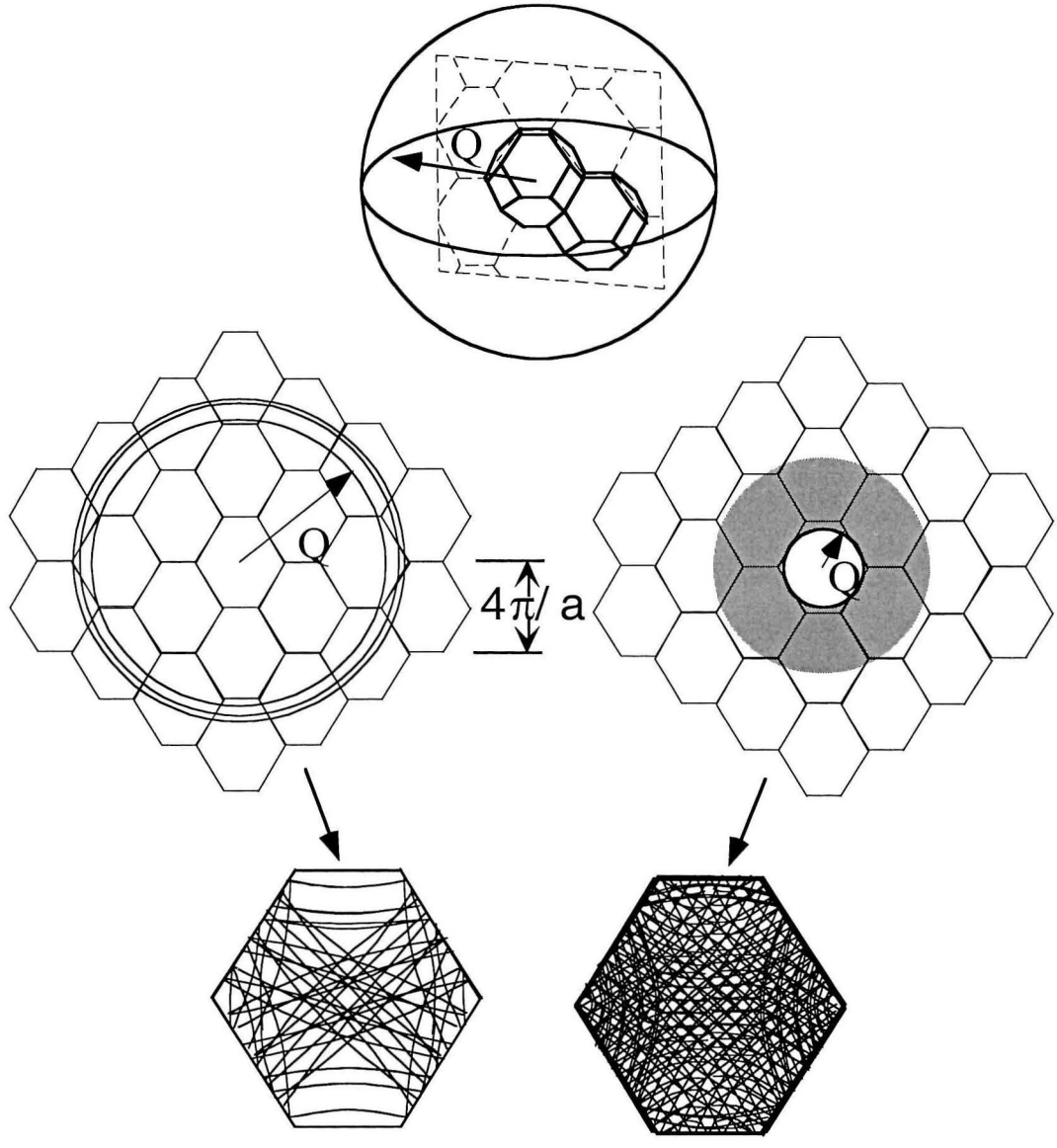

Figure 3.2. Q-space measured. Top picture shows the first Brillouin zone for the fcc structure and a cross section plane for the pictures below. On the left the Q values from the measurements of Roberston, et al. [7] (3.924 $Å^{-1}$, 4.292 $Å^{-1}$, and 4.432 $Å^{-1}$) are shown cutting through a plane and then the in-plane parts are projected into the first zone (bottom left). On the right the equivalent TOF Q-space is shown for an energy transfer of 3.55 meV. For scale, the lattice parameter, a, was taken to be 5.18 Å.

The multiphonon part, Equation 2.4, was subtracted from the data to give an estimate of the one-phonon scattering plus a small nearly constant background (~5%) from magnetic and multiple scattering. After a constant background subtraction this was then used to determine a new phonon DOS that was in turn used to recalculate the multiphonon contribution. The procedure was repeated until the phonon DOS converged to within statistical errors (three iterations). Figure 3.3 is a calculation showing the size of the magnetic scattering relative to the one-phonon scattering. The magnetic scattering was extrapolated from low temperature measurements of the temperature dependence of the magnetic spectra [8]. The one-phonon scattering was calculated with a Born von Karmán model using the force constants of Stasis, et al. [9]. Since the sample was designed for approximately 10% scattering, the multiple scattering should be of order 1%.

There were no statistically significant differences between the γ-cerium at 795 K and 984 K or between the δ-cerium at 1006 K and 1021 K, so to improve statistics each pair of curves was added together. The resulting average phonon DOS for the γ and δ phases are shown in Figure 3.4. Because data were analyzed on the neutron energy gain side of the spectrum, the energy resolution in the phonon DOS decreases with increasing energy from 0.14 meV (at the elastic line) to 1 meV (at 10 meV). The measured result for the fcc phase is in good agreement with the DOS calculated with a Born von Karmán model using the force constants of Stasis et al. [9]. For direct comparison, the calculated $S_1(\omega)$ was convoluted with the instrument resolution function and then multiplied by a thermal factor to obtain the calculated phonon DOS.

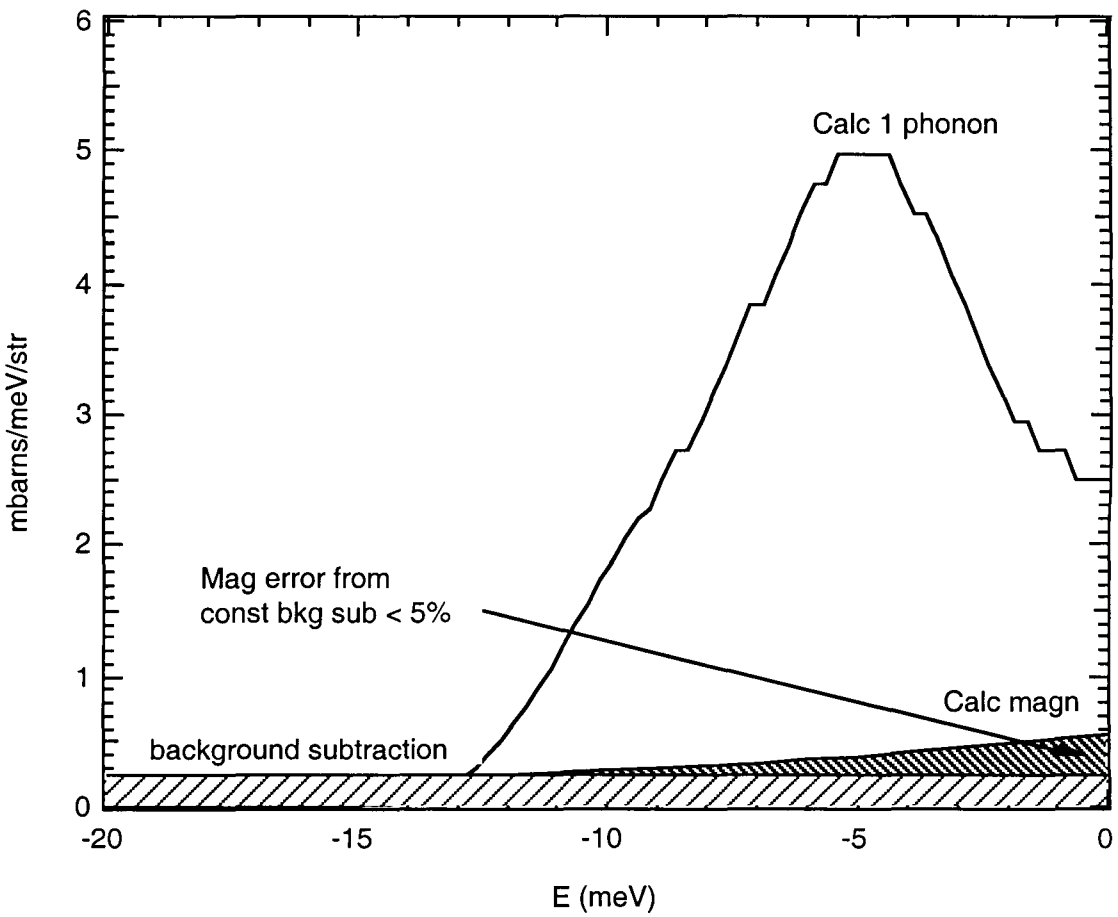

Figure 3.3. Magnetic contribution relative to the one-phonon scattering.

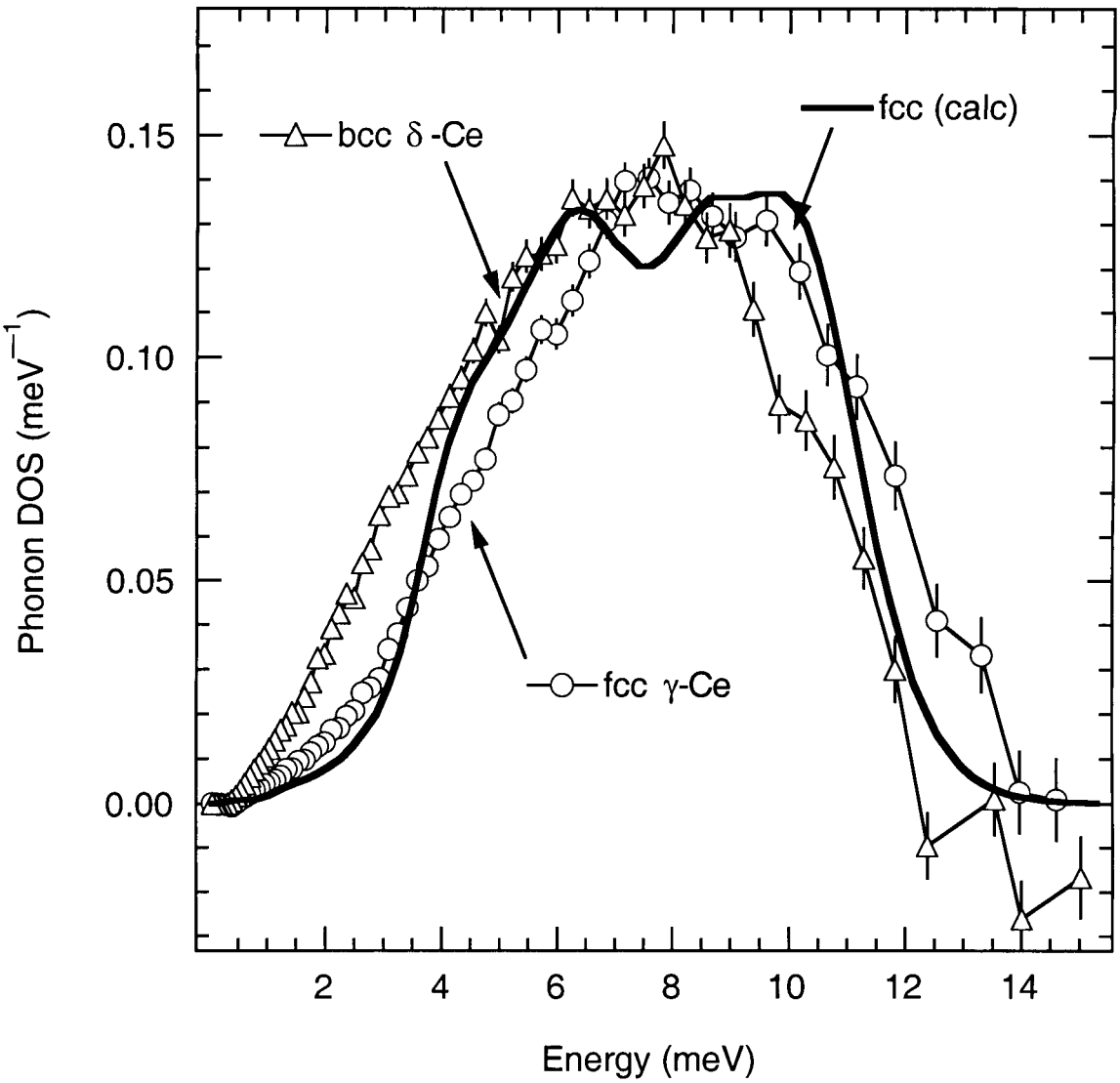

Figure 3.4. Phonon DOS of δ-cerium at 1006 K and 1021 K and γ-cerium at 795 K and 984 K. Solid dark curve: phonon DOS of γ-cerium, calculated using force constants of Stasis, et al. [9], and convoluted with the instrument resolution function.

Integration of the difference in the measured phonon DOS gave $\Delta S_{vib}^{\delta-\gamma} = (0.71 \pm 0.05)$ k_B/atom. The error is based mainly on the uncertainty in the background subtraction (Figure 3.3). Other errors include counting statistics and the energy resolution. The resolution broadening of measured features in $S(\omega)$ tends to cause a slight underestimate of entropy

differences calculated from the phonon DOS. The underestimate comes from both the apparent increases in measured cutoff energies due to broadening, and from a smoothing out of sharp differences in the measured $S(\omega)$. Fortunately, most of the difference in vibrational entropy of the γ and δ cerium originates with the difference in DOS curves below 7 meV where the experimental energy resolution was best.

3.2.4 Discussion

The phonon DOS of cerium shows a large increase in low energy modes (up to 7 meV) when it transforms from fcc (γ) to bcc (δ), Figure 3.4. This was similar to the triple axis results of Robertson et al. [7], although this previous work reported an enhancement of the low energy modes only up to 4 meV rather than 7 meV. The triple axis results are shown in Figure 3.5. The additional enhancement of the low energy modes increases the calculated vibrational entropy difference at the transition temperature from $\Delta S_{vib}^{\delta-\gamma} = (0.51\pm0.05)$ k_B/atom [7] to $\Delta S_{vib}^{\delta-\gamma} = (0.71\pm0.05)$ k_B/atom. The discrepancy suggests that the Q-sum in the triple axis measurements may not have been adequate to average out coherence effects. This higher value is slightly less than what Robertson et al. [7] obtained from diffraction measurements, $\Delta S_{vib}^{\delta-\gamma} = 0.84$ k_B/atom, although these Debye-Waller factor measurements were affected by crystallographic texture in the sample.

The thermodynamic implications of the increase in low energy modes were noted by Robertson, et al. [7]. The most significant result is that the derived vibrational entropy of the transition, $\Delta S_{vib}^{\delta-\gamma} = (0.71\pm0.05)$ k_B/atom, is much larger than that expected from the latent heat 0.35-0.36 k_B/atom [10, 11]. To account for this difference, it was suggested that the

electronic entropy of δ-cerium is lower than γ-cerium. The present results increase the estimate of the electronic entropy from 0.14 k_B/atom to 0.35 k_B/atom. It is surprising that electronic entropy can be significant in a high temperature structural phase transition, but this seems plausible in light of recent calculations of the electronic DOS of fcc and bct cerium by Ravindran et al. [12] and Eriksson et al. [1]. Further evidence that electronic changes are important in high temperature cerium is given by the argument that the contraction of δ-cerium upon melting is caused by an electronic transition [13].

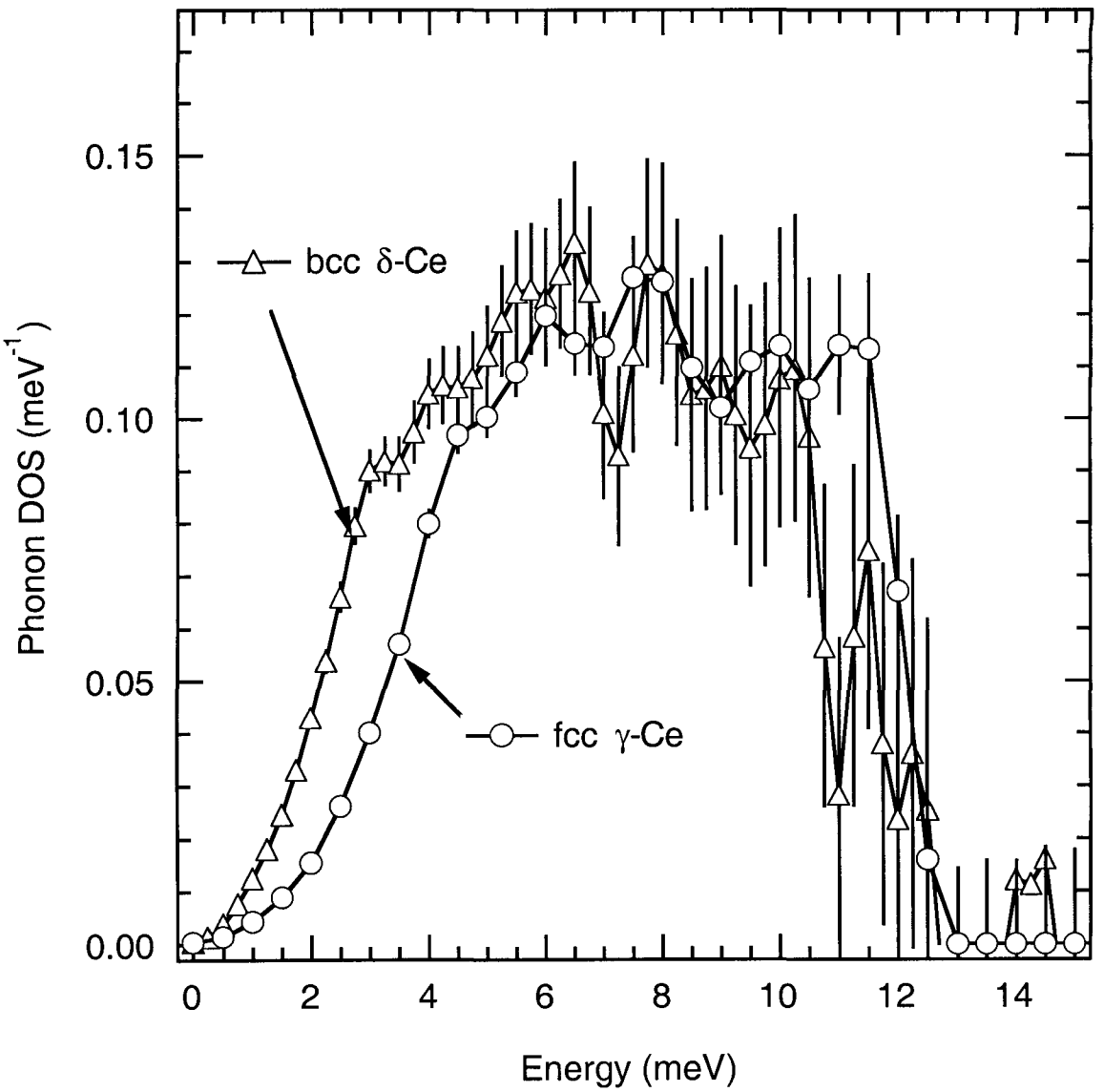

Figure 3.5. Phonon DOS of δ-cerium and γ-cerium determined from triple axis measurements by Robertson et al. [7].

3.3 Detailed study of the vibrational and electronic entropy of β-cerium and γ-cerium

3.3.1 Introduction

Electronic states of an atom, which are degenerate for isolated atoms, are split into various crystal field levels when the atom is in a crystal. If this crystal field splitting of electronic levels is of order k_BT, there is a contribution to the specific heat associated with the partial occupancy of the electronic states. This is seen as the "Schottky anomaly" in the specific heat. These levels can also be determined from measurements of crystal field excitations in the neutron magnetic scattering. Magnetic scattering can be effectively isolated from phonon scattering because it dominates at low angles, whereas phonon scattering dominates at high angles. A phase transition can change the local symmetry and the strength of the crystal field splitting and hence change the entropy. In the present chapter we compare the 4f-electron level splitting of β–cerium and γ–cerium to determine the change in crystal field entropy. We also consider the contribution from spin fluctuations of the 4f-electrons seen as a broadening of the measured crystal field energy levels. To identify any remaining entropy contribution, we compare the vibrational and crystal field splitting entropy with the latent heat measured at the β–γ transition temperature. We deduce that there is a third contribution to the β–γ transition, probably electronic in origin.

3.3.2 Experimental

Two different cold-rolled and annealed plates (approximately 100 grams each) of 99.9+% pure cerium in the γ-phase were prepared for inelastic neutron scattering

measurements at 300 K. For β-cerium measurements at 150 K and 300 K, one of the γ-cerium plates was transformed to more than 95% β-cerium using a thermal cycling technique similar to that described by Koskimaki, et al. [14]. The procedure involved cycling from room temperature to 77 K 20 times, annealing at 345 K for 6 days, and cycling another 20 times.

Neutron scattering measurements were performed on the LRMECS spectrometer at the Intense Pulsed Neutron Source of the Argonne National Laboratory. The samples were mounted in a closed-cycle helium displex refrigerator. Inelastic measurements were made with incident neutron energies of E_i = 45 and 25 meV. The raw data were corrected for self-shielding, sample environment background, detector efficiency, and k_f/k_f phase space factor. The data were normalized in absolute units of millibarns/(steradian · Ce atom) by comparison to a vanadium standard measured under identical spectrometer conditions, giving the scattering function $S(\theta,\omega)$, where θ is the scattering angle and $\hbar\omega$ the energy transfer.

3.3.3. Data analysis

The analysis of the magnetic scattering is described in detail elsewhere [8]. The procedure involves summing experimental data from detector banks in the low angle range from 1.95°-51.6° to increase statistics and minimize the contribution from phonon scattering, which increases with θ. Figure 1a shows the magnetic and phonon contribution for the low angle sum at 300 K and E_i = 45 meV. The higher resolution data obtained with E_i = 25 meV did not reveal any additional information on the magnetic scattering at 300 K because the lifetime broadening was much greater than the instrument resolution. The magnetic peak positions were fit using the peak positions inferred from low temperature measurements and

accounting for thermal broadening [8]. The phonon contribution was approximated using a measured La spectra and accounting for the relative cross sections.

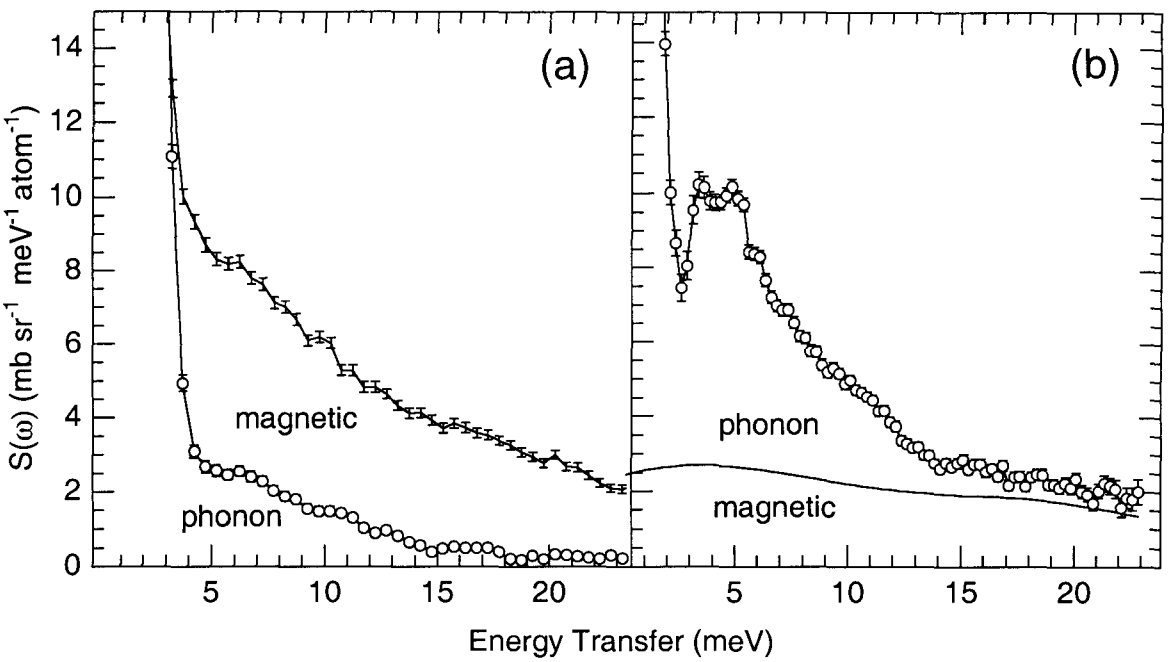

Figure 3.6. Phonon and magnetic contributions to $S(\omega)$ for β-Ce at 300 K; (a) E_i = 45 meV and summed over the low angle range 1.95°-51.6°, (b) E_i = 25 meV and summed over the high angular range 55.3° -118.5°. The relatively constant phonon contribution above the phonon cut off (about 14 meV) is from multiphonon scattering.

The phonon scattering was studied by summing over the high angle range 55.3° - 118.5° where the phonon scattering was largest. The 300 K data were appropriate for phonon scattering determinations because the magnetic excitations were broadened and comparatively weak. Using the magnetic form factor, the magnetic scattering was extrapolated from the low angle data to the high angle range and subtracted from the phonon scattering. The size of this magnetic correction is shown in Figure 3.6b. The good separation of phonon and magnetic scattering is evident by comparing their relative 3.6a and 3.6b.

The incoherent multiphonon scattering was iteratively determined to all orders using the procedure described in Section 2.3.1 of this thesis. The final phonon DOS are shown in Figure 3.7. The γ-cerium (fcc) and β-cerium (dhcp) phonon DOS were essentially identical to the corresponding fcc and dhcp phonon DOS measured for lanthanum [15].

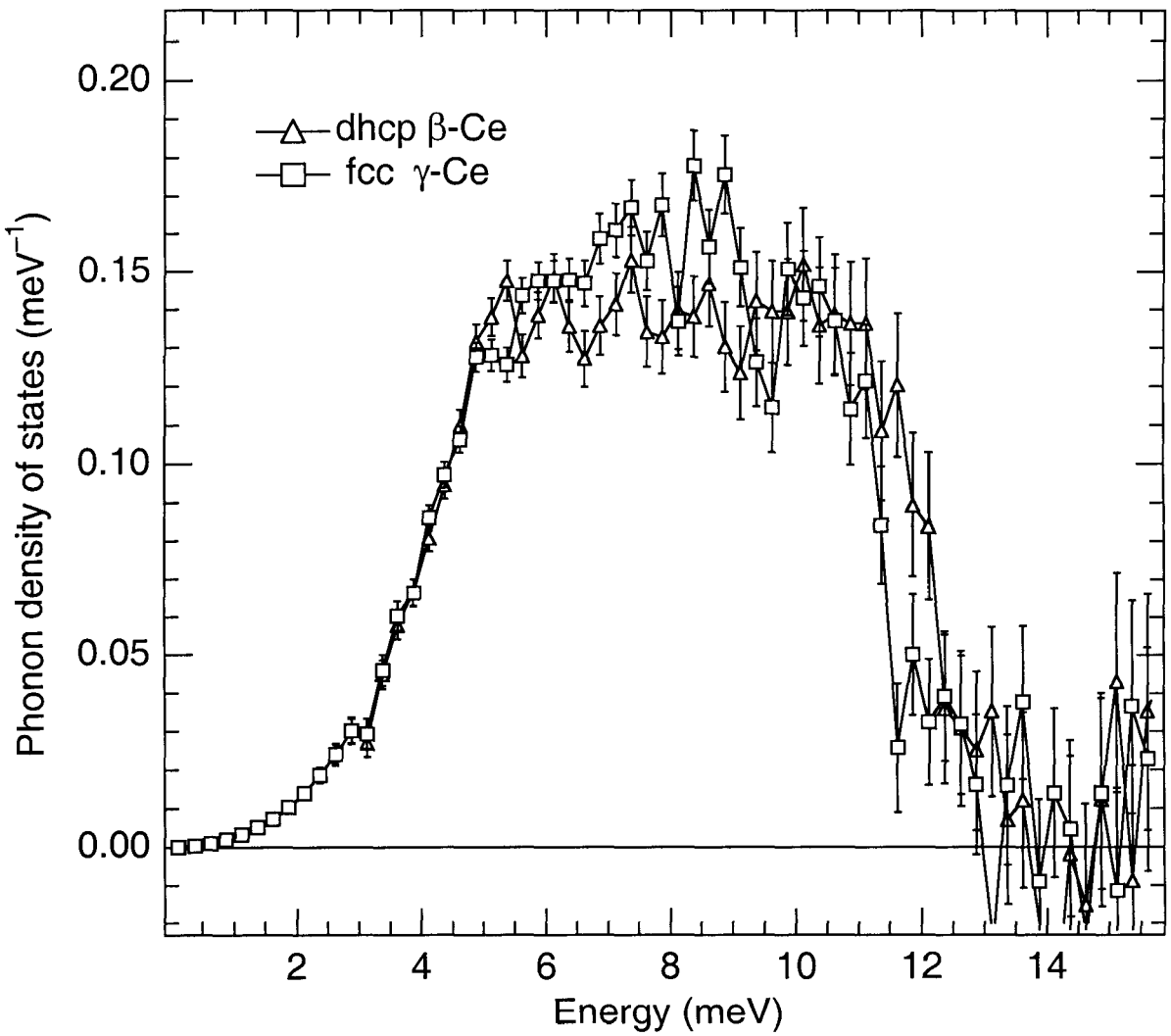

Figure 3.7. Phonon DOS curves for β-cerium and γ-cerium at 300K.

3.3.4 Discussion

The measured phonon DOS (Figure 3.7) was used to calculate the phonon part of the specific heat. The constant volume (harmonic) part of the phonon specific heat was calculated using:

$$C_{V,vib}(T) = 3k_B \int_0^\infty g(\omega) \left(\frac{\hbar\omega}{k_B T} \right)^2 \frac{\exp\left[\frac{\hbar\omega}{k_B T}\right]}{(\exp\left[\frac{\hbar\omega}{k_B T}\right] - 1)^2} d\omega. \qquad (3.1)$$

The size of the anharmonic contribution from volume expansion, $C_p - C_V = 9Bv\alpha^2T$, was estimated using the specific volume, v, bulk modulus, B (0.20 Mbar) [16], and thermal expansion coefficient, α (8.1×10^{-6} K^{-1}) [7] , of γ-cerium. This contribution was less than the error on the specific heat (~0.1 J/mol-K) over the temperature range used in this analysis, Figure 3.8, and was thus neglected. It is assumed that anharmonic contribution to β-cerium and γ-cerium are similar in magnitude since they have similar densities and are both close-packed structures differing only in stacking sequence.

The γ-cerium (fcc) has a well-defined crystal field excitation at 17 meV [8]. For a 4f electron with fcc symmetry this corresponds to a transition from a doublet (Γ_7) to quartet (Γ_8) [17]. The β-cerium (dhcp) data did not show all of crystal field peaks because some were too weak and broadened to separate from the quasielastic scattering. The details of this problem are discussed in a separate report on the magnetic scattering in this data set [8]. The basic problem seems to be a fairly strong hybridization of the f-states with the conduction band. This makes accurate predictions of thermodynamic quantities from simple crystal field models difficult without supporting measurements. Fortunately, calorimetry measurements were made on β-cerium at low temperatures by Koskimaki, et al. [18], Tsang, et al. [19], and

Gschneidner and Pecharsky [20]. After subtracting the phonon part using Equation 5 we fit the remaining heat capacity by assuming three contributions from the electronic degrees of freedom; (1) crystal field, (2) spin fluctuations, and (3) the usual electronic excitations at the Fermi energy. The phonon-subtracted specific heat is shown in Figure 3.8.

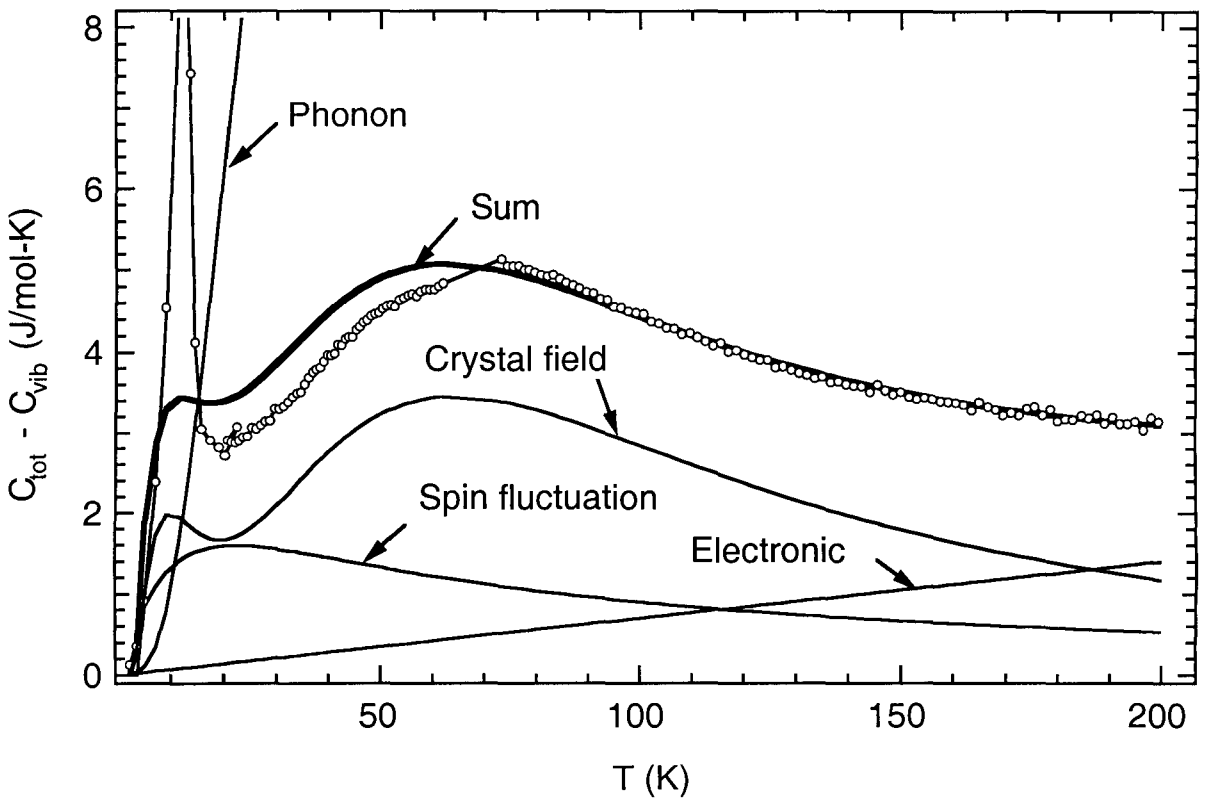

Figure 3.8. Phonon-subtracted heat capacity of β-cerium (O). Phonon contribution was calculated from the β-cerium phonon DOS shown in Fig. 2. The crystal field (Schottky) contribution was calculated from the level scheme determined using the inelastic neutron scattering spectra [8]. The spin fluctuation (Kondo) contribution was calculated with the Coqblin-Schrieffer model [21]. The thick curve shows the sum of the crystal field, spin fluctuation, and electronic contributions. The linear electronic contribution was adjusted such that the sum matched the specific heat at high temperatures. Peak at around 10 K is due to an antiferromagnetic transition. The heat capacity data are those from measurements of Koskimaki et al. [18], Tsang et al. [19], and Gschneidner and Pecharsky [20].

The β-cerium dhcp structure has an equal number of sites with cubic local symmetry and hexagonal local symmetry. The cubic site has the same doublet (Γ_7) to quartet (Γ_8) 17 meV crystal field excitation as the fcc structure [8]. As discussed by McQueeney et al. [8], it is possible to predict the hexagonal level scheme from the measured cubic levels by following the assumptions of the Superposition Model [22]. Briefly, the relevant crystal field scaling parameters depend only on the polar coordinates of the ligands. Because the only difference between the local environments of the cubic and hexagonal sites is a $\pi/3$ rotation of the closed-packed plane above the site, the relevant scaling parameters are identical on both sites. Based on the cubic splitting, the crystal field level scheme on the hexagonal sites was $|\pm 1/2\rangle$ at 0 meV, $|\pm 5/2\rangle$ at 1.9 meV and $|\pm 3/2\rangle$ at 9 meV [8]. Thus, if we neglect the effects of lifetime broadening, the mean crystal field energy can be determined using

$$U_{CF} = \frac{1}{Z(T)} \sum_n E_n \exp\left(\frac{-E_n}{k_B T}\right), \tag{3.2}$$

where

$$Z(T) = \sum_n \exp\left(\frac{-E_n}{k_B T}\right), \tag{3.3}$$

and n is summed over all levels (half on cubic sites and half on hexagonal sites). The crystal field specific heat is then given by

$$C_{CF}(T) \equiv \left(\frac{\partial U_{CF}}{\partial T}\right)_V = \sum_n \left[\frac{E_n^2}{Z(T) k_B T^2} - \frac{\partial Z(T)}{\partial T} \frac{E_n}{Z(T)^2}\right] \exp\left(\frac{-E_n}{k_B T}\right). \tag{3.4}$$

The crystal field specific heat calculated from this level scheme is shown in Figure 3.8. It should be noted that the lifetime broadening of the crystal field levels is significant [8]. A justification for using the simple model of the sharp levels is that the specific heat is an

integral quantity, so the details of the broadening are smoothed out to a large extent. We do, however, include the broadening in the ground state separately below.

The interaction of the localized 4f-electrons with the conduction electrons provides an energy spread for the ground state doublet ($|\pm 1/2\rangle$ on the hexagonal sites and Γ_7 on the cubic sites). This can be seen as quasielastic spin fluctuations in the neutron inelastic magnetic spectra [8]. The spread of these states contributes an additional term to the electronic specific heat. The simplest way to treat this problem is with the Kondo impurity model as is often done with heavy fermion systems [23]. The problem is in fact very similar, but with a much higher Kondo temperature ($T_K \sim$ 40 K [22]) and a much weaker enhancement of the electronic specific heat at low temperatures. Further support for this approach is that a resistivity anomally in β-cerium at around 50 K has been interpreted successfully in terms of a quenched Kondo scattering mechanism [24]. Rajan calculated an exact expression for the specific heat using the Coqblin-Schrieffer Model [23]. For the doublet ground states the specific heat from Kondo spin fluctuations is given by [23]

$$C_{SF}(T) = k_B \int_{-\infty}^{\infty} \frac{g_{SF}(\varepsilon)(\varepsilon/2k_BT)^2}{\cosh^2(\varepsilon/2k_BT)} d\varepsilon, \tag{3.5}$$

where $g_{SF}(\varepsilon)$ is the spin fluctuation density of states that modifies a standard result for a 2-level system. We approximate the spin fluctuation density of states as a lorentzian with a half-width determined from the neutron quasielastic width extrapolated to zero temperature, ~ 4 meV [8]. The calculated specific heat for this contribution is labeled "spin fluctuation" in Figure 3.8. We did not attempt to fit the specific heat at the lowest temperatures because of the antiferromagnetic transition at ~ 10 K.

If we assume temperatures well below the Fermi temperature, T_f, and that the energy derivatives of the electronic DOS can be neglected, the electronic specific heat in the free electron model can be expressed in terms of the electronic DOS at the Fermi level, $C_{el}(T) = g(\varepsilon_f)(\pi^2/3)k_B^2T$. Therefore, with these approximations just one adjustable parameter, the electronic specific heat constant, $\gamma = g(\varepsilon_f)(\pi^2/3)k_B^2$, was required to fit the remaining electronic contribution to the specific heat data. The fit, shown in Figure 3.8, gives γ = (7.0±0.1) mJ/mol-K^2. With this it is confirmed that temperatures are well below the Fermi temperature since $T_f = (\pi^2/2)(k_B/\gamma)$ = 6060 K. Since the narrow 4f-bands result in the largest derivative, our second assumption depends mainly on the location of the 4f-bands with respect to the Fermi level. According to Baer and Busch [25] the 4f-bands lie ~ 900 meV below the Fermi energy in γ-cerium and thus should not affect the derivatives. More recent results suggest it may be in the 1 to 2 eV range [26]. In any case, if the next term in the Sommerfeld expansion were large, an additional T^3 term would need to be added to the electronic specific heat. The data do not warrant such a correction.

Despite the simplicity of the models used, the sum of the various electronic components fit the data surprisingly well above the antiferromagnetic transition as shown in Figure 3.8. However, it should be pointed out that many assumptions were not quite correct. In fact, it seems unlikely that crystal field picture is even correct in a strict sense since the hybridization with conduction electrons is so strong [8]. A more accurate model would include the hybridization of each crystal field state with the conduction electrons. On the other hand, since the specific heat is adequately reproduced, the entropy associated with an effective crystal field can be calculated accurately.

The calculated contributions to the specific heat were used to calculate the entropy difference between γ-cerium and β-cerium as a function of temperature using

$$\Delta S_i^{\gamma-\beta}(T) = \int_0^T \frac{\Delta C_i^{\gamma-\beta}}{T} dT, \tag{3.6}$$

where *i* indicates the entropy contribution (*i* = *el, vib*, and *CF*). Although the spin fluctuation part was significant, it made no measurable contribution to the entropy difference since the quasielastic scattering of γ-cerium was nearly identical to β-cerium [8]. The crystal field and vibrational entropy differences are compared in Figure 3.9. At the experimental transition temperature (420 K), the crystal field contribution is negligible compared to the vibrational contribution. The latent heat measured at ~420 K implies an entropy change of only 0.05 k_B/atom [27], which is smaller than the vibrational entropy. Thus, by setting the sum of the entropy differences equal to the latent heat, Figure 3.9 implies an electronic entropy difference of $\Delta S_{el}^{\gamma-\beta}$ = – (0.04 ± 0.05) k_B/atom. This difference is similar to predictions at 420 K using the electronic specific heat constants of Koskimaki et al. [18] for low temperature calorimetry measurements on γ-cerium and β-cerium (-0.096 k_B/atom). However, Koskimaki et al. [18] noted significant uncertainty in the electronic specific heat constant for β-cerium and attributed it to the low temperature antiferromagnetic transition (near 11 K in Figure 3.8). Perhaps more significant was the fact that Koskimaki et al. neglected the spin fluctuation. (This is not surprising, since at the time of this publication (1974) heavy fermions were unknown and the calculations of Rajan [23] did not exist.) This latter point probably explains why they found such an unusually large value for the electronic specific heat constant, γ, at low temperatures (~46 mJ/mol-K^2) but could not reconcile it with the high temperature trend.

Based on the Kondo impurity model with a $T_K \sim 40$ K, the low temperature limit of the specific heat is of order $C\ (T \rightarrow 0)/T = \gamma = 1.29\pi k_B/6T_K \sim 100$ mJ/mol-K^2 [23]. Thus, it is not surprising that Koskimaki, et al. found a significantly enhanced electronic specific heat constant at low temperatures.

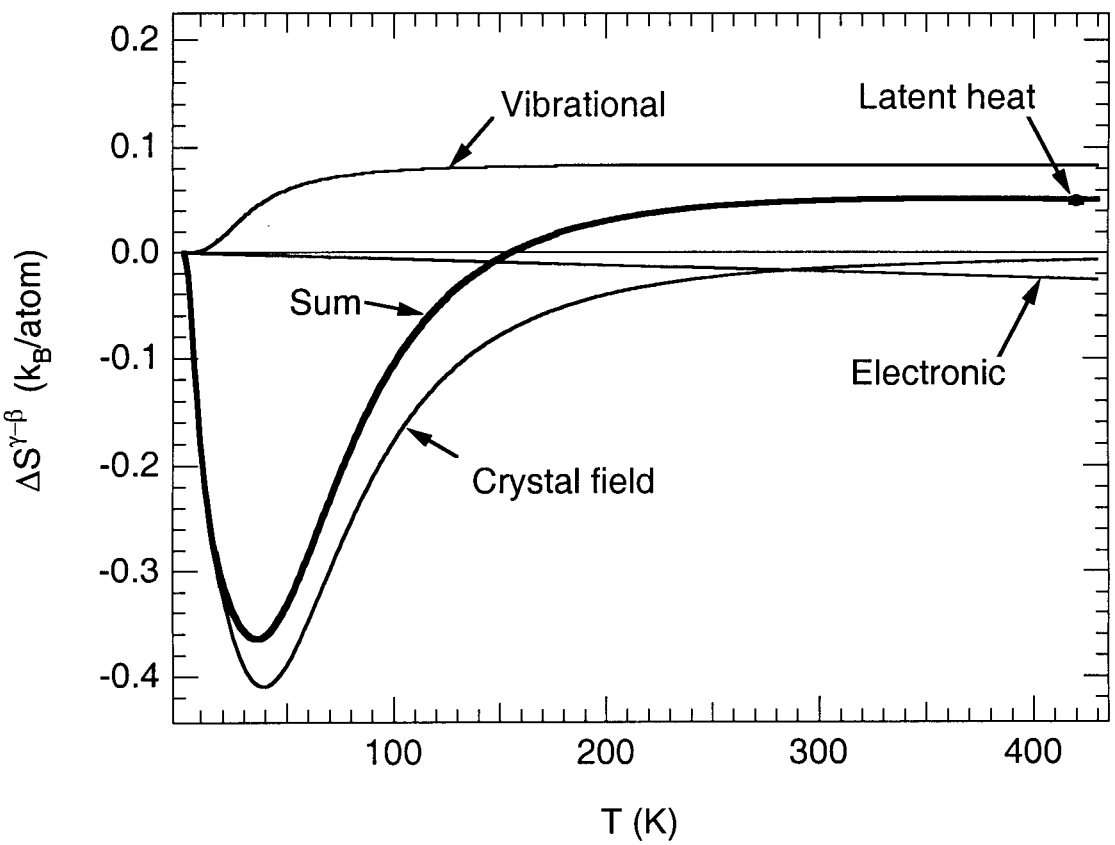

Figure 3.9. Crystal field, vibrational and electronic contributions to the entropy difference between γ-cerium and β-cerium. Thick curve shows the sum of the three components. The electronic component was adjusted so that the sum equaled the value obtained from the latent heat measurement of Gschneidner *et al.*, [27].

Because of this uncertainty in the electronic specific, the electronic specific heat constant of β-cerium (dhcp) was assumed to be equal to that of dhcp-lanthanum [18]. The present results make no such assumption, and thus imply independent estimates of the

electronic specific heat constants; (7.0±0.1) mJ/mol-K^2 for β-cerium from the fit in Figure 3.8 and (6.2±0.8) mJ/mol-K^2 for γ-cerium accounting for the latent heat and other entropy terms. Compared with the values used by Koskimaki et al. [18], 9.4 mJ/mol-K^2 for β-cerium (which is actually just the lanthanum value) and 7.5 mJ/mol-K^2 for γ-cerium, our values are both slightly smaller but their difference is similar.

The crystal field and electronic entropy tend to stabilize the γ-phase with respect to the β-phase at low temperatures. Although the crystal field entropy difference is negligible at the measured transition temperature (420 K), it becomes important at the lower (true) transformation temperature, 283 K, determined in a 20 year study by Gschneidner, et al. [27]. Of course in a 20 year study it is not possible to measure the latent heat and, thus, determine the total entropy change. However, inspection of Figure 3.9 shows that the entropy difference is essentially the same in magnitude as at 420 K but that the crystal field entropy assumes a more significant role with respect to the electronic entropy (from continuous excitation of electrons across the fermi energy.)

3.3.5 Summary

The relative contributions of the vibrational and electronic degrees of freedom to the entropy of the β– and γ–phases of cerium were determined. Many competing sources of vibrational and electronic entropy need to be included in the equation of state of cerium. Their different temperature dependencies change their relative importance. However, at the experimentally observed transition temperature (~420 K) a vibrational entropy difference of $\Delta S_{vib}^{\gamma-\beta} = (0.09 \pm 0.05)\ k_B$/atom is dominant followed by the electronic contribution $\Delta S_{el}^{\gamma-\beta} = -$

(0.04 ± 0.05) k_B/atom and a negligible crystal field contribution. The crystal field entropy difference dominates at low temperatures and is comparable to the electronic contribution at the true transition temperature, 283 K. A contribution from quasielastic fluctuations from Kondo scattering was significant, but showed no difference between the two phases.

References

[1] O. Eriksson, J. M. Wills, and A. J. Boring, Phys. Rev. B **46**, 12981 (1992).

[2] P. Soderlind, O. Eriksson, and B. Johansson, Phys. Rev. B **50**, 7291 (1994).

[3] P. Soderlind, O. Eriksson, B. Johansson and J. M. Wills, Phys. Rev. B **52**, 13169 (1995).

[4] A. Svane, Phys. Rev. Lett. **72**, 1248 (1994).

[5] A. Svane, Phys. Rev. B **53**, 4275 (1996).

[6] T. Charpentier, G. Zerah, and N. Vast, Phys. Rev. B **54**, 1427 (1996).

[7] J. L. Robertson, H. N. Frase, P. D. Bogdanoff, M. E. Manley, B. Fultz, and R. J. McQueeney, Phil. Mag. Lett. **79**, 297 (1999).

[8] R. J., McQueeney, M. E. Manley, B. Fultz, G. Kwei, R. Osborn, and P. Bogdanoff, Dynamic magnetic susceptibility in γ-cerium, β-cerium, and low-density cerium alloys, Phil. Mag. B., in press (2000).

[9] C. Stassis, T. Gould, O.D. McMasters, K. A. Gschneidner, Jr., and R. M. Nicklow, Phys. Rev. *B* **19**, 5746 (1979).

[10] G. Beggerow, In Landolt-Bornstein, New Series, *Numerical Data and Functional Relationships in Science and Technology*, K. H. Hellwege (editor), Group 4, Vol. 4 (Berlin: Springer-Verlag) p. 9 (1980).

[11] I. Barhin and B. Patzki, *Thermochemical Data of Pure Substances*, Vol. 1 (Weinheim: VCH), p. 507 (1995).

[12] P. Ravindran, L. Nordstrom, R. Ahuja, J. M. Wills, B. Johansson, and O. Eriksson, Phys. Rev. B **57**, 2091 (1998).

[13] A.K. Singh and T.G. Ramesh, *The Metallic and Nonmetallic States of Matter,* edited by Edwards, P. P. and Rao, C. N. R. (Taylor and Francis: London and Philadelphia), Ch. 13, p. 359 (1985).

[14] D. C. Koskimaki, K. A. Gschneidner, and N. T. Jrand Panousis, J. of Crystal Growth **22**, 225 (1974).

[15] N. Nücker, *Proc. Int. Conf. On Lattice Dynamics,* Paris, Flammarion Sci, p. 244 (1977).

[16] F. F. Voronov, L. F. Vereshchagin, and V. A. Goncharorva, Sov. Phys. Dokl. **135**, 1280 (1960).

[17] K. R. Lea, M. J. M. Leask, and W. P. Wolf, J. Phys. Chem. Solids **23**, 1381 (1962).

[18] D. C. Koskimaki and K. A. Gschneidner, Jr., Phys. Rev. B **10**, 2055 (1974).

[19] T. W. E. Tsang, K. A. Gschneidner, Jr., D. C. Koskimaki, and J. O. Moorman, Phys. Rev. B **14**, 4447 (1976).

[20] K. A. Gschneidner, Jr., and V. K. Pecharsky, J. of Phase Equilibria **20**, 612 (1999).

[21] V. T. Rajan, Phys. Rev. Lett. **51**, 308 (1983).

[22] D. J. Newman and B. Ng, Rep. Prog. Phys. **52**, 699 (1989).

[23] A. Yatskar, W. P. Beyermann, R. Movsovich, and P. C. Canfield, Phys. Rev. Lett. **77**, 3637 (1996).

[24] S. J. Liu, P. Burgardt, K. A. Gschneidner, and S. Legvold, J. Phys. F: Metal Phys. **6**, L55 (1976).

[25] Y. Baer and G. Busch, J. Electron Spectrosc. Related Phenom. **5**, 611 (1974).

[26] J. Rohler, *Handbook on the Physics and Chemistry of Rare Earths*, Vol. 1, edited by K. A. Gschneidner, Jr., L. Eyring, and S. Hufner (Elsevier Science, New York, 1987), Vol. 10, p. 453.

[27] K. A. Gschneidner, Jr., V. K. Pecharsky, Jaephil Cho, and S. W. Martin, Scripta Materialia **34**, 1717 (1996).

Chapter Four Heat capacity and microstructure of ordered and disordered Pd_3V

In this Chapter a connection is made between anharmonic atomic scale vibrations and a microstructural scale contribution to the specific heat. It is also found that the microstructural contribution to the specific heat is restricted by plasticity.

4.1 Introduction

It is now accepted that crystallographic differences between phases cause differences in vibrational entropy. It is less clear, however, if microstructure can affect the heat capacity of a phase, and hence its stability. Nanocrystalline Fe and Ni_3Fe exhibit changes in their phonon DOS that alter somewhat their stability with respect to large grained material [1-3]. A recent experimental study of anharmonic effects in Ni_3V [4] suggested that some of the heat capacity of Ni_3V could originate with internal stresses that develop during anisotropic thermal expansion, but such effects were not shown conclusively. The present study was designed to test if such microstructural stresses could affect the heat capacity of Pd_3V, which has the same DO_{22} ordering phase transition as Ni_3V.

The difference in entropy of two states or phases of a material, α and β, is found by measuring differences in heat capacities at constant pressure, $\Delta C_p^{\beta-\alpha} = C_p^{\beta} - C_p^{\alpha}$, as a function of temperature and integrating

$$\Delta S^{\beta-\alpha} = \int_0^T \frac{\Delta C_p^{\beta-\alpha}}{T'} dT' \quad . \tag{4.1}$$

For measurements of vibrational entropy, the atomic arrangements in the two states, α and β, must remain unchanged throughout the differential calorimetry measurements. This is usually not a problem because most of the harmonic vibrational entropy difference comes from the low temperature range of the integrand where there is no significant atomic diffusion.

The standard relationship between the thermal expansion coefficient, α, and the heat capacity at constant pressure, C_p, is with the Grüneisen relation [5]

$$\alpha = \frac{\gamma}{3B_S V} C_p \quad , \tag{4.2}$$

where B_S is the adiabatic bulk modulus, V is the volume and γ is the Grüniesen constant. This relationship can be derived from the anharmonic contribution to the vibrational specific heat by assuming a quasiharmonic model (cf. Chapter 2.1 and Chapter 6.1). In this case the Grüniesen constant is given by the volume sensitivity of the phonon frequencies $\gamma_i = -\frac{V}{\omega_i}\frac{\partial \omega_i}{\partial V}$, appropriately averaged over all phonons (typically, $\gamma \cong 2$). For small changes between states, the differential thermal expansion coefficient is given by

$$\Delta\alpha^{\beta-\alpha}(T) = \frac{\gamma}{3B_S V}\Delta C_p^{\beta-\alpha}(T) + C_p(T)\Delta\left(\frac{\gamma}{3B_S V}\right)^{\beta-\alpha} \quad , \tag{4.3}$$

where the notation, $\Delta(x)^{\beta-\alpha}$, means the difference in the quantity, x, between the two phases, α and β. At low temperatures, where α and C_p vary more strongly than the other parameters, it seems reasonable to assume that α and C_p are proportional. It is often easier to measure differential thermal expansion, $\Delta\alpha$, than differential heat capacity, ΔC_p, and we use both methods in the present investigation. Thermal expansion measurements were used previously

to obtain differences in vibrational entropy [7], but a comparison was not made with the more direct differential calorimetry measurements. In the present work we find excellent agreement between the temperature dependence of $\Delta\alpha$ and ΔC_p. This agreement extends to higher temperatures where significant anharmonicity is observed. We attribute the anharmonicity to both the conventional thermodynamic source of Equation 4.2 and 4.3, but also to strain in the microstructure.

4.2 Experimental

Ingots of Pd_3V were prepared from elemental Pd (99.9%) and V (99.9%) by induction melting in an argon atmosphere. For calorimetry, a pair of disks (188.7 mg) were cut from ingots with a slow speed saw. The edges were ground so that the masses were matched to within 0.1 mg. Samples for differential thermal expansion measurements were made by cold-rolling ingots to about 0.1 mm thickness and cutting out two strips (40 mm by 4 mm). A solid cylinder (8.63 mm diameter and 8 mm long) was also machined for ultrasonic sound velocity measurements and for absolute thermal expansion measurements. All five of these pieces were annealed in evacuated quartz ampoules at 1100 ^{0}C for 2 h, and quenched by breaking the ampoules in iced brine. One of the strips and one disk were used directly in this state, which was confirmed to be disordered fcc by X-ray diffractometry. The remaining strip and disk were transformed to the ordered DO_{22} state by annealing in evacuated quartz ampoules at 780 ^{0}C for 10 days. The annealing of the cold-rolled strip also induced recrystallization and reduced the rolling texture. X-ray diffractometry was performed with an Inel CPS-120 diffractometer using Co Kα radiation with an Al filter to suppress the V Kα fluorescence.

Differential heat capacity was measured with a Perkin-Elmer DSC-4 differential scanning calorimeter (DSC) that had been modified by installing its sample head in a liquid-helium dewar [8]. The sample disks, one disordered and one ordered, were placed in the two sample pans of the DSC. Heat capacity measurements comprised pairs of runs, with the two samples interchanged in the sample pans between runs. The difference in heat capacity was found from the difference of these two sets of runs. Ten matched runs were performed to ensure reproducibility. To counteract instrumental drift, runs comprised two pairs of scans over temperature intervals of 30 K, which overlapped by 10 K.

Two strips, one disordered and one ordered, were spot-welded to make a bi-layer sample for differential thermal expansion measurements. The spot welds were estimated to have melted < 5% of the total sample volume. The difference in thermal expansion was determined by cantilevering the bi-layer and measuring the deflection of its free end with an optical lever. Assuming the elastic constants are similar, the deflection of the laser beam is

$$\delta \cong \left(\frac{D}{h}\right) L \, \Delta\alpha^{dis-ord} \Delta T \quad , \tag{4.4}$$

where D is the distance from the sample to the optical sensor, $2h$ is the thickness of the bi-layer, and L is the length of the sample as shown in Figure 4.1 (see Appendix D for a detailed derivation of Equation 4.4). The difference in thermal expansion coefficients of the disordered and ordered strips, $\Delta\alpha^{dis-ord}$, causes a difference in their lengths over a temperature range of ΔT that is $L\Delta\alpha^{dis-ord}\Delta T$. The measured deflection, δ, is D/h times the expansion difference of isolated strips. Since $D/h \cong 5000$ for our experiment, thermal expansion differences as small as 2.5×10^{-8} could be measured. No attempt was made to

measure the precise sample geometry, so absolute thermal expansion coefficient differences were not measured. We sought to measure the functional form of $\Delta\alpha^{dis\text{-}ord}(T)$, and compare it to results from calorimetry or $\Delta C_p^{dis\text{-}ord}$.

Temperature was controlled by clamping the bi-layer to a cold copper finger in a vacuum chamber. As shown in Figure 4.1, the copper finger was cooled by flowing cryogenic fluid (liquid N_2 or He), and the finger was heated resistively. A steady-state temperature was maintained for 1 to 2 minutes before recording the deflection. Five runs were made with the laser reflection from the ordered side and one run was made with the bi-layer turned over.

Absolute thermal expansion measurements were performed from 300 K to 770 K with a Perkin Elmer TMA-7 thermomechanical analyzer. To ensure reproducibility, two heating and three cooling cycles were measured. Ultrasonic measurements of longitudinal and transverse wave velocities were performed using 10 MHz transducers of 0.6 cm diameter. A disordered cylindrical sample (8.63 mm diameter and 8 mm long) was measured first. The same sample was annealed to develop DO_{22} chemical order and measured again.

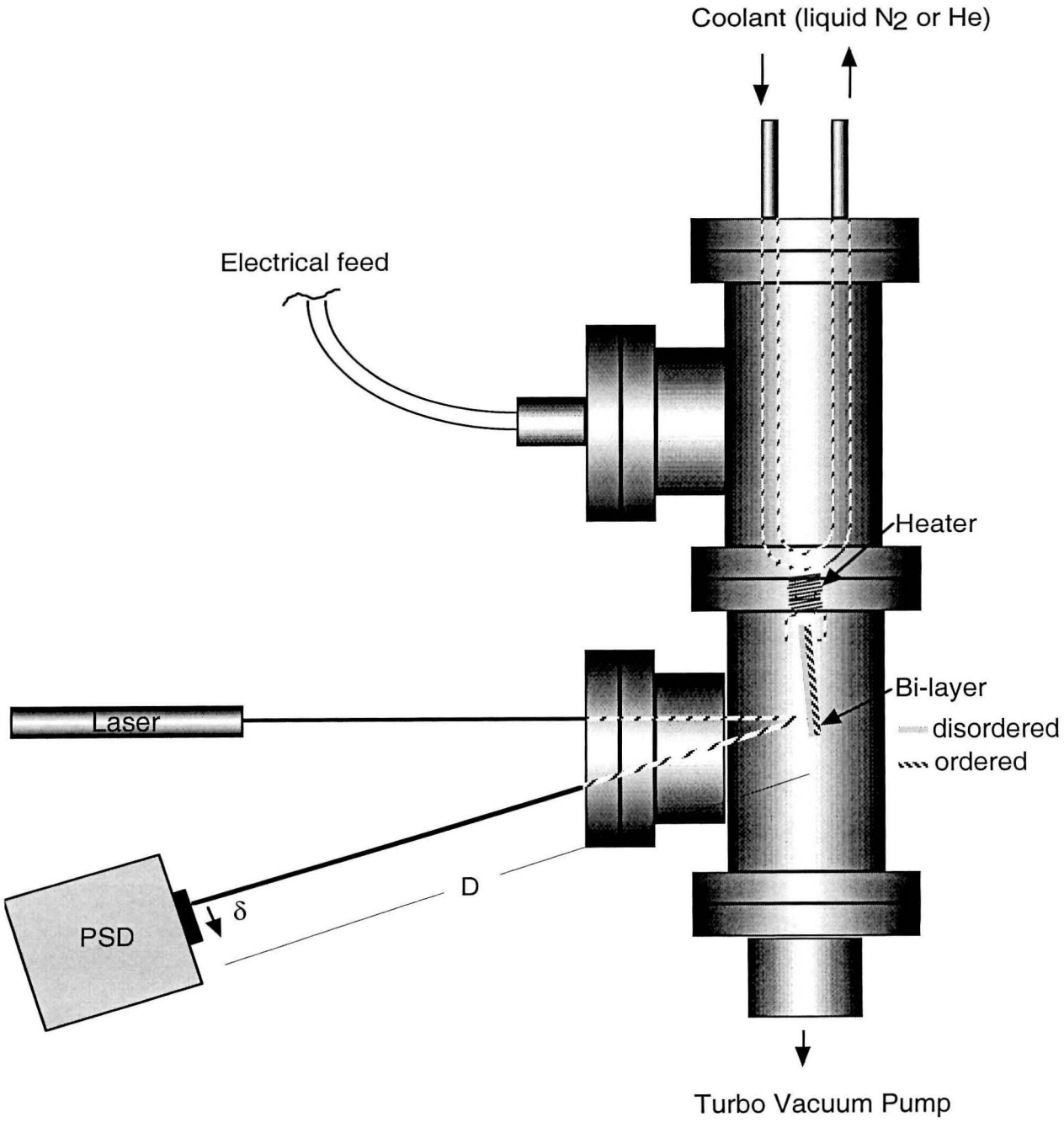

Figure 4.1. Schematic of differential dilatometer.

Metallography was performed on the ordered calorimetry sample through a procedure of thermal cycling. The sample was annealed at 780 (C for ten days, after which the surface was polished and etched with a 3:1 hydrochloric to nitric acid solution. A digital image of the microstructure was then taken. The sample was subsequently immersed in liquid nitrogen for about a minute, warmed to room temperature, and a second image was taken. The sample was cycled ten more times in liquid nitrogen, and an image was taken after each cycle. To ensure reproducibility, the same experiment was performed again after a second anneal.

4.3 Results

X-ray diffractometry was performed on all samples. Figure 4.2 presents X-ray diffraction patterns for both the quenched (fcc-disordered) sample and the annealed (DO22-ordered) sample. The presence of DO22 order was shown by the formation of superlattice diffraction peaks and a slight splitting of the "fcc" peaks owing to the development of some tetragonality of the unit cell. The tetragonality, c/a = 2.01, was the same as that observed by Maldonado and Schubert [9] but slightly smaller than that observed by Dwight, Downey, and Conner [10] (c/a = 2.015). The diffraction data were used to calculate molar volumes of 8.63_10–6 m3/mol for the DO22-ordered state and 8.69_10–6 m3/mol for the fcc disordered state.

Results from an average of ten pairs of differential scanning calorimetry (DSC) runs are shown in Figure 4.3. Error bars are the standard deviations of the data from the different runs. The positive sign of the data shows that the disordered state has a larger heat capacity

than the ordered state. The magnitude of the difference was less than 1% of the typical heat capacity of a solid (25 J mol–1K–1) and was a challenge for calorimetric measurement. The data are qualitatively similar to those observed for Ni3V [4].

Figure 4.2. X-ray powder diffraction pattern of the disordered and ordered Pd3V. Inset shows peak splitting of the (220) "fcc" fundamental peak. Small unlabled peaks were from a surface oxide.

Results from an average of six differential thermal expansion (DTE) runs were scaled to match the calorimetry results and are presented in Figure 4.3. Error bars are the standard deviations of the data from different runs. The scaled errors were 10 to 30 times smaller than the DSC results. Note that near 150 K, (_dis-ord (0 and (Cp_dis-ord__(0. Since Cp must be greater than zero, Equation 4.3 implies that (((/3BSV)dis-ord is zero. Assuming (((/3BSV)dis-ord remains zero at all temperatures, the DTE and DSC results should be proportional to each other. This assumption is supported by the experimental data, since the DSC results and scaled DTE results have no discernable differences over the full range of temperature. The consistency of the thermal expansion data and calorimetry data gives more credibility to both, including the unexpected dip at 150 K.

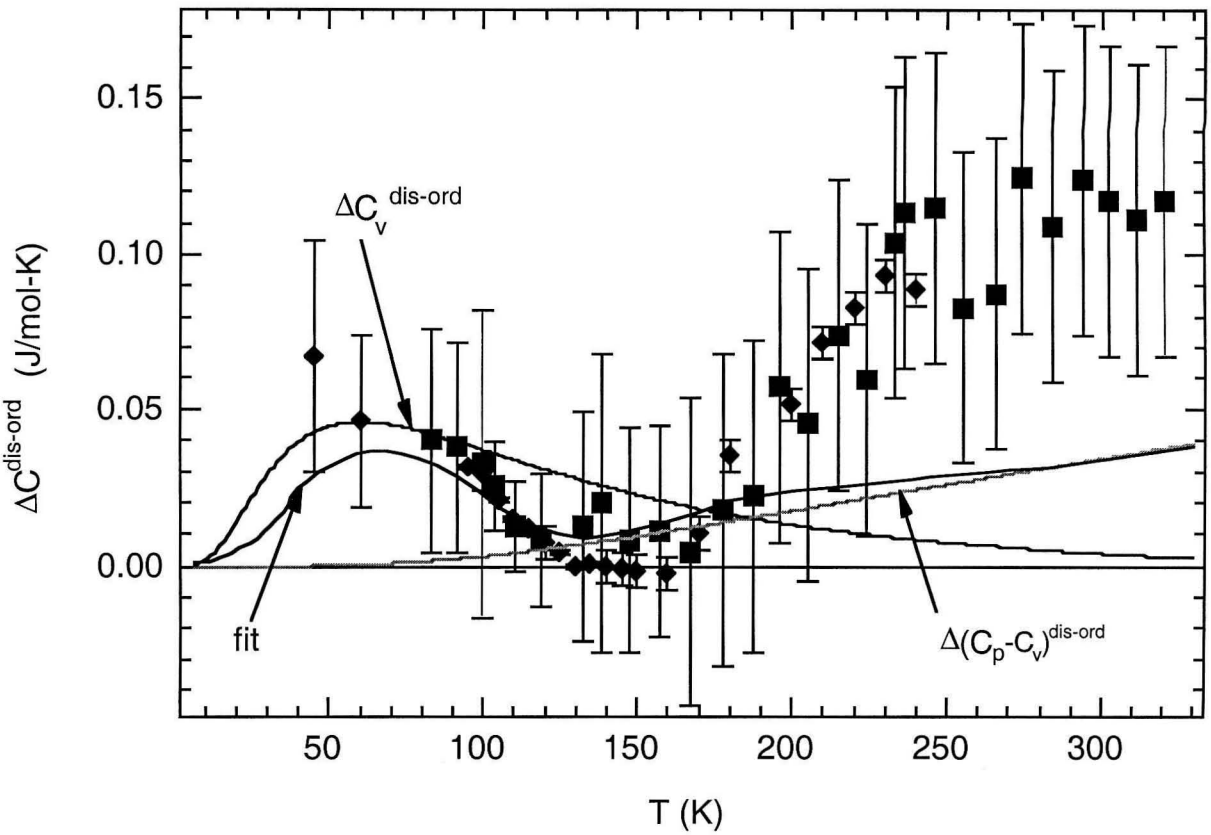

Figure 4.3. Differential heat capacity (■, DSC) and differential thermal expansion coefficient scaled by 500,000 J $mol^{-1}K^{-1}$ (◆, DTE). Curve $\Delta C_V^{dis\text{-}ord}$ was fit to data using the difference in two Debye curves. Curve $\Delta(C_p\text{-}C_V)^{dis\text{-}ord}$ is the anharmonic volume expansion contribution calculated from measured properties. The curve labeled "fit" is the sum of ΔC_V, $\Delta(C_p\text{-}C_V)^{dis\text{-}ord}$ and the microstructural contribution including plasticity (as described in the text).

The high temperature thermal expansion coefficient was obtained by differentiating the measured displacements in the TMA scans. These results, shown in Figure 4.4, indicate that the thermal expansion coefficient increases gradually with temperature. The contraction on cooling was slightly larger than the expansion on heating. This irreversibility is discussed below.

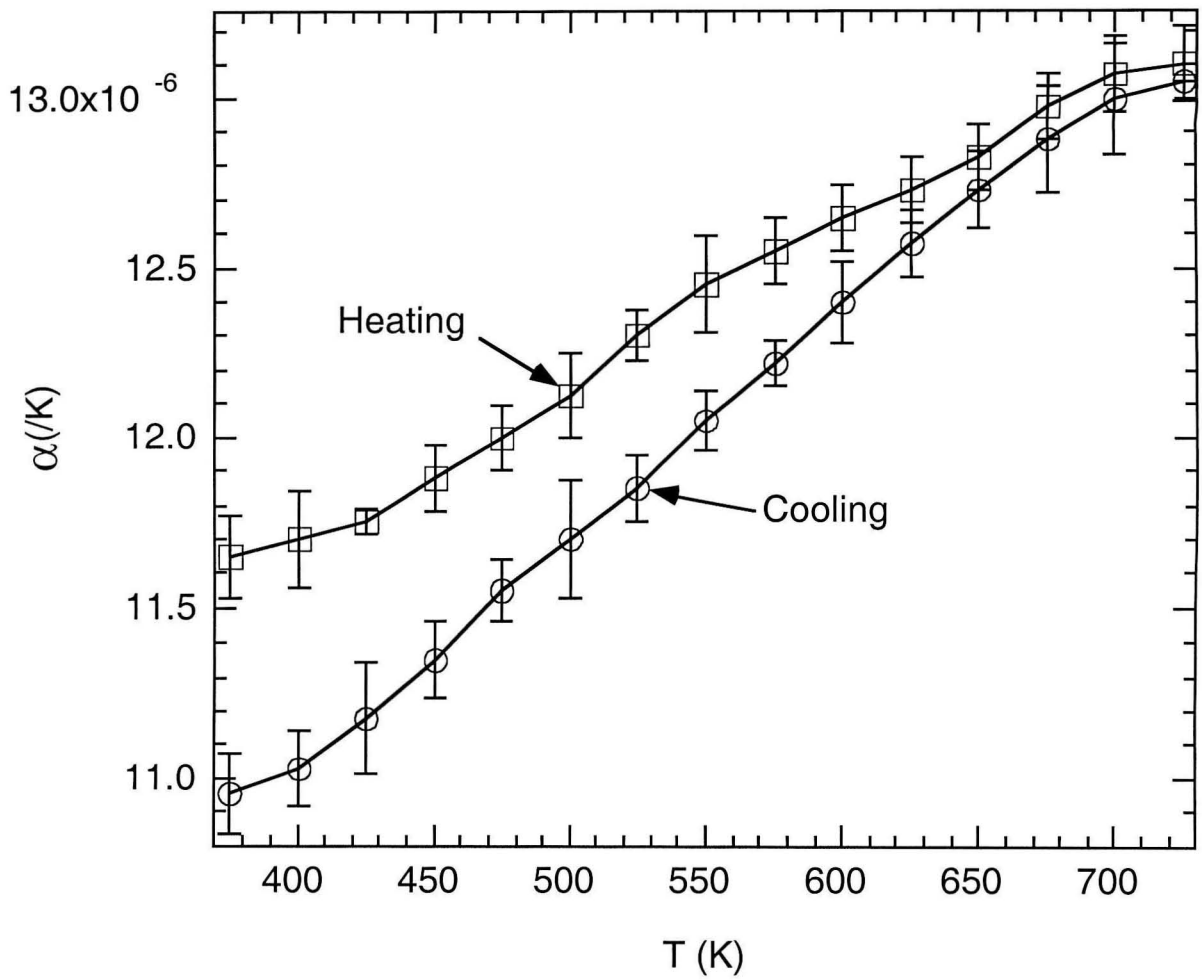

Figure 4.4. Thermal expansion coefficient of ordered Pd_3V.

The longitudinal sound velocity increased from 5064±5 m/sec in the disordered state to 5137±5 m/sec in the ordered state. The transverse sound velocity was more sensitive to ordering; the transverse velocity was 2547±5 m/sec in the disordered and 2664±5 m/sec in the ordered state. Since the sample length (8 mm) was several times the wavelength, the adiabatic elastic constants were calculated using the long bar approximation with densities obtained from diffraction data, and assuming an isotropic polycrystalline average. The results, presented in Table 4.1, indicate that although elastic constants change by a significant amount, the bulk modulus is essentially unchanged.

Table 4.1. Measured adiabatic elastic constants.

Material	c_{11} (10^{11} N/m^2)	c_{44} (10^{11} N/m^2)	$B = (c_{11} - \frac{4}{3}c_{44})$ (10^{11} N/m^2)
fcc-disordered Pd_3V	2.71±0.01	0.685±0.003	1.797±0.006
DO_{22}-ordered Pd_3V	2.81±0.01	0.755±0.003	1.803±0.006

Images of the microstructure showed an unrecovered microstrain of about 3% after the first liquid nitrogen thermal cycle (see Figure 4.5). The strain was determined by first removing any rotations by aligning a small part of the microstructure (*e.g.*, grain boundaries on the left in Figure 4.5b). The remaining bend in the microstructure gave the net unrecovered microstrain. To test the consistency of the image alignment, additional cycles were performed and the images were aligned with the uncycled sample. Ten additional cycles showed no new unrecovered microstrain when aligned with the sample that received one cycle. These results were repeated for another sample with a full set of images. Further evidence for plastic strains during thermal excursions was found in X-ray lineshapes, which broadened slightly from their room temperature widths when the material was heated to temperatures of less than 400 K. The additional line broadening was difficult to assess quantitatively, however, since the individual crystallites were too large to provide a good polycrystalline average in the diffraction pattern.

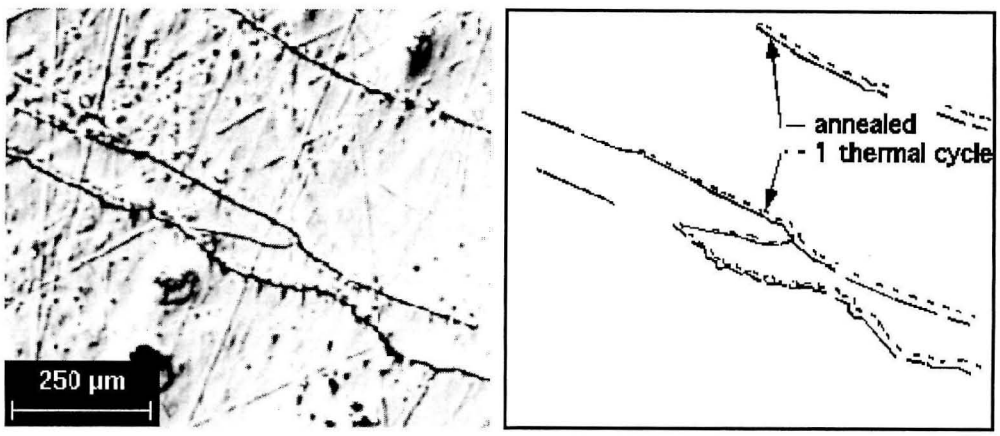

Figure 4.5. Metallography of ordered Pd_3V. (a) Image taken after annealing. (b) Trace of grain boundaries in images taken before and after the first liquid nitrogen cooling cycle. The images were overlain so that the grain boundaries on the left-hand side were aligned.

4.4 Discussion

Following the work of Nagel, Fultz, Robertson and Spooner [4], we explain the measured shape of the differential heat capacity in Figure 4.3 by assuming three contributions; (1) harmonic vibrations, (2) the anharmonic $C_p - C_V$ term, and (3) a microstructural strain energy contribution from anisotropic contractions of the DO_{22} structure. When the harmonic contribution was approximated as the difference between two Debye curves with θ_{dis} = 290 K and θ_{ord} = 291 K, harmonic vibrations account adequately for the low temperature, constant volume contribution to the heat capacity difference in Figure 4.3 and give the peak at 60 K. The anharmonic $C_p - C_V$ term accounts for the energy expended when thermal expansion works against the bulk modulus of the material. The

specific volumes calculated from diffraction data, v, measured thermal expansion coefficients, α, and the bulk moduli from ultrasonic measurements, B, were used to calculate this anharmonic contribution to the heat capacity:

$$\Delta(C_p - C_V)^{dis\text{-}ord} = \Delta(9Bv\alpha^2T)^{dis\text{-}ord} \cong (1\pm 0.3)\times 10^{-4}T \quad (\mathrm{J/mol^{-1}K^{-1}}). \quad (4.5)$$

Figure 4.3 shows that this anharmonic term accounts for only a small part of the anharmonic contribution to the heat capacity at 300 K.

The microstructural contribution, first suggested by Nagel, Fultz, Robertson and Spooner [4], is a consequence of the anisotropy of the thermal expansion of the DO_{22}-ordered phase in a polycrystalline sample. As the material is cooled, anisotropies in its contraction cause a buildup of elastic strain energy. An irregular microstructure of tetragonal grains can be free of strain at one temperature, T_0, but changes in temperature cause a buildup of microstructural strain. We expect no such effect in the disordered phase because the structure is cubic. When thermal expansion is anisotropic, however, this can be represented as an extra term in the difference in the Gibbs free energies of the two phases, $\Delta E_{\mu str}^{dis-ord}$,

$$\Delta G^{dis-ord} = \Delta H^{dis-ord} - T\Delta S_{vib}^{dis-ord} - \Delta E_{\mu str}^{dis-ord}. \quad (4.6)$$

The difference in vibrational and "microstructural" entropies is then

$$\Delta S_{vib.\mu str}^{dis-ord} = \int_0^T \frac{\Delta C_V^{dis-ord} + \Delta(C_p - C_V)^{dis-ord} - \Delta C_{\mu str}}{T'} dT', \quad (4.7)$$

where

$$\Delta C_{\mu str} = \frac{\partial E_{\mu str}^{ord}}{\partial T}. \quad (4.8)$$

A detailed calculation of the microstructural contribution is not practical. However, assuming linear elasticity (with fixed elastic properties), and assuming that the ordered microstructure formed in a state of minimum strain energy at temperature T_0, the microstuctural strain energy will have the form

$$E_{\mu str} \propto \left[\int_{T}^{T_0} \overline{\alpha}(T')dT' \right]^2, \tag{4.9}$$

where T_0 is a reference temperature where the internal stress is zero, such as the temperature of the ordering treatment (780 °C). Here $\overline{\alpha}$ is an averaged thermal expansion coefficient. The temperature derivative of Equation 4.9 gives

$$C_{\mu str} \propto -\overline{\alpha}(T) \int_{T}^{T_0} \overline{\alpha}(T')dT' \cdot \tag{4.10}$$

The negative sign accounts for the fact that the strain energy increases when the temperature decreases below the temperature T_0. Thus, $C_{\mu str}$ makes a positive contribution in Figure 4.3. Assuming that the average thermal expansion coefficient has the same shape as a Debye heat capacity curve (Grüniesen's law), $C_{\mu str}$ was calculated from Equation 4.10, with the results shown as "Elastic" in Figure 4.6. This microstructural contribution combined with the anharmonic and Debye contribution can partially account for the heat capacity data. However, it cannot account adequately for the dip in the differential heat capacity near 150 K.

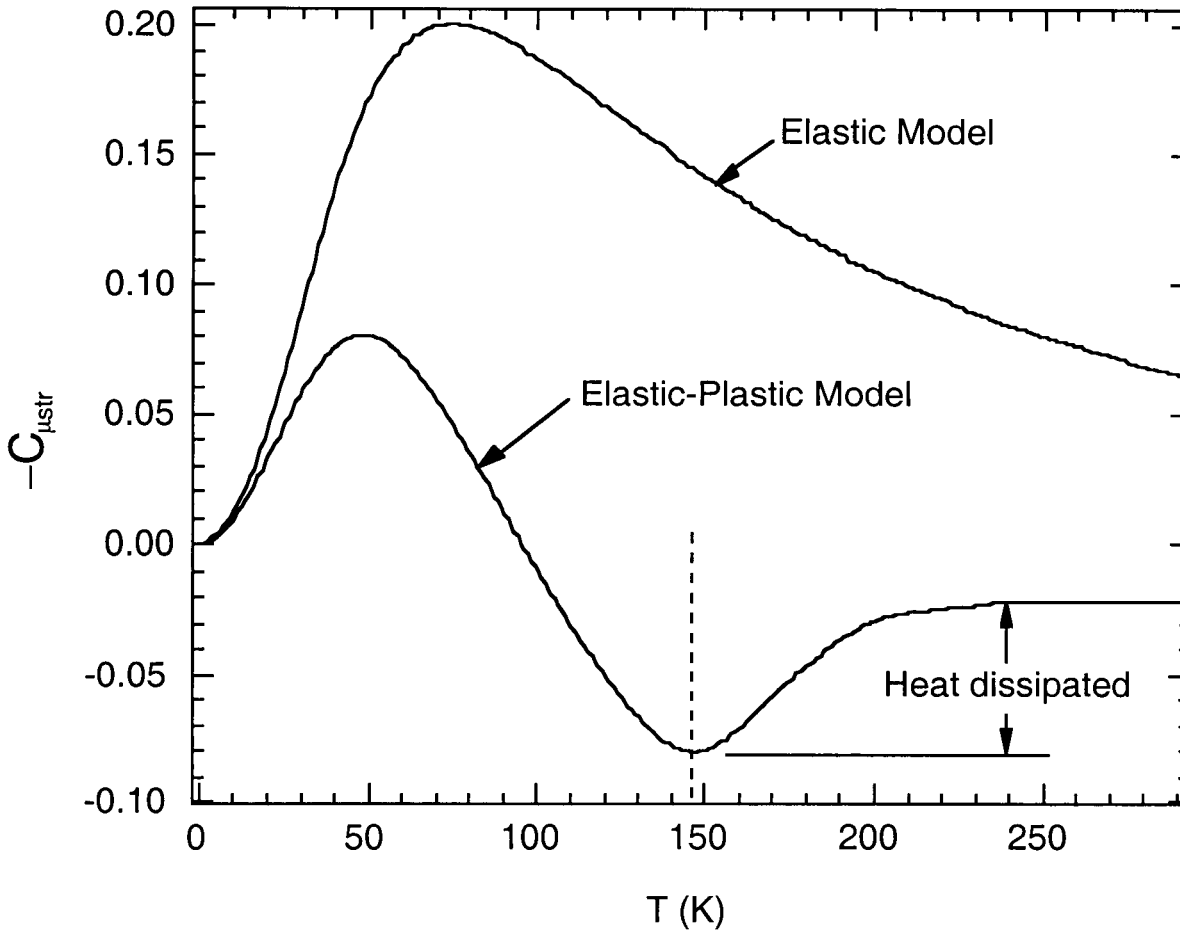

Figure 4.6. Microstructural contribution to heat capacity with and without the effects of plastic flow. Plastic flow begins to the right of the dashed line in the elastic-plastic model (as described in text).

The above analysis assumed elastic strains. The microstructural images, Figure 4.5, showed that plastic strain was imparted to the sample during thermal cycling. The simplest way to include plastic behavior into the heat capacity is to assume that as the material is cooled, internal stresses build up to a yield stress and then remain constant (*i.e.*, no work hardening or softening). The microstructural stress-temperature curve for this process (Figure 4.7) shows how plastic deformation leads to a decrease in the reference temperature, $T_0 \rightarrow T_1$, upon cooling, and an increase in the reference temperature on heating, $T_1 \rightarrow T_2$. The reference

temperature lags T by a characteristic temperature ΔT_y. The ΔT_y is the temperature difference that provides sufficient thermal expansion to induce local yielding. More realistically, inhomogeneities in the microstructural stress would lead to a distribution for ΔT_y, but determining the actual distribution is impractical. As a first approximation we assumed a single average ΔT_y .

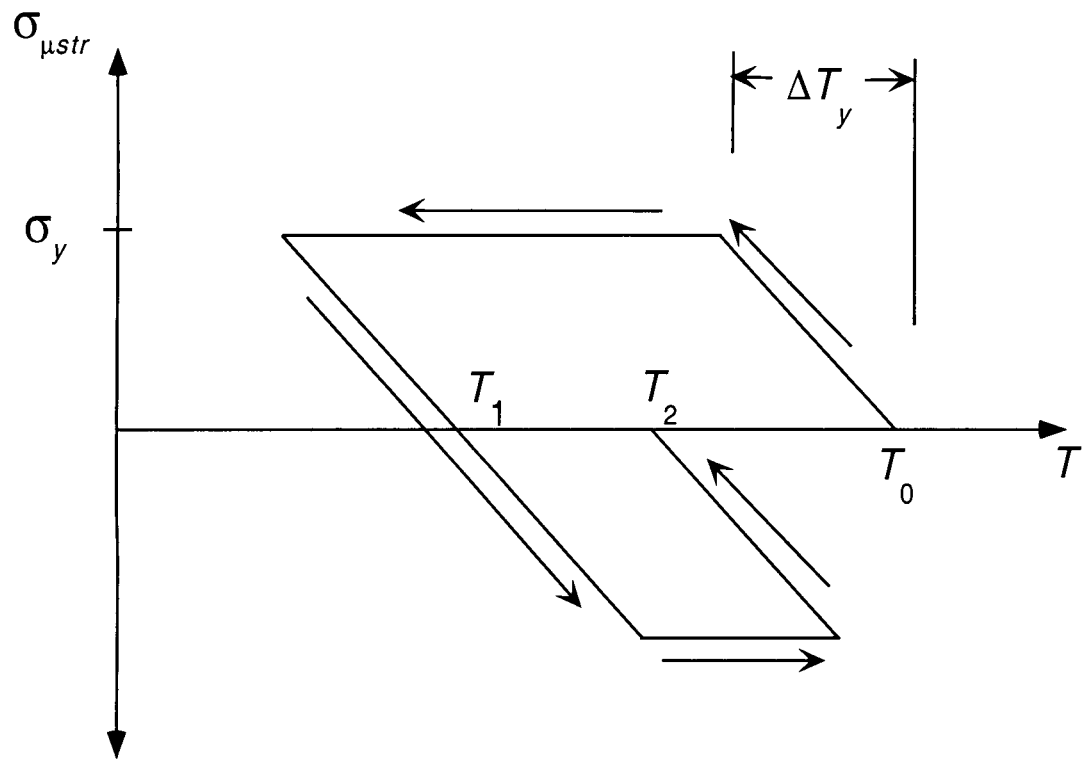

Figure 4.7. Simplified temperature (T) versus microstructural stress ($\sigma_{\mu str}$) diagram. The parameter σ_y is the microstructural yield stress. The parameter ΔT_y is the change in temperature from the minimum stress state to the yield stress.

We tested a microstructural heat capacity model that included the elastic and plastic response of the material induced by thermal expansion. The elastic part was calculated using Equations 4.9 and 4.10. For the plastic part, we assume that once steady state-plastic flow is

achieved, there is no net generation of defects and dislocations to alter the internal energy of the material. With this assumption, the work required for plastic flow will equal the heat evolved by the plastic flow. A microstructural heat capacity was then determined for heating from 90 K, Figure 4.6. By adjusting ΔT_y, it was found that $\Delta T_y = 30$ gives a dip at 150 K similar to that observed in the measurements, Figure 4.3. The dip at 150 K corresponds to a microstructural yielding that is expected outside the range $2\Delta T_y$. At temperatures around 150 K, the plastic response dominates over the elastic response. The transition from initial yielding at 150 K to steady-state plastic flow at about 250 K was adjusted to match the data. In this model the "Elastic-Plastic" heat capacity (Figure 4.6) above 150 K is from a net formation of defects. For temperature changes of more than 160 K, the defect density is assumed steady-state so our model of a fixed ΔT_y therefore predicts zero microstructural contribution to the heat capacity of the material.

To check if ΔT_y =30 K is reasonable, a simple comparison was made with the observed microstrains in the thermal cycle experiments. For a given temperature change, the average microstrain, ε_μ, is given approximately by a constant, A, times the relevant temperature change ΔT, as $\varepsilon_\mu = A\Delta T$. The proportionality constant, A, is a material property and should be similar for the thermal cycle, the thermal expansion, and the calorimetry measurements. The yielding microstrain in the ordered phase is then estimated from

$$\varepsilon_y \cong \left(\Delta T_y / \Delta T_{cycle} \right) \varepsilon_{cycle} = 0.004, \qquad (4.11)$$

where ΔT_{cycle} is the temperature range of the thermal cycle (223 K), and the observed unrecovered microstrain (0.03) from Figure 4.5 was used for ε_{cycle}. We expect the cycle microstrain to be greater than the unrecovered microstrain used in the calculation. The

temperature dependence of A was neglected. Using the unrecovered strain tends to cause an underestimate of ε_y, while neglecting the temperature dependence causes an overestimate of about a factor of two. Thus, the predicted yield strain at $\Delta T_y = 30$ K is at least 0.002, which is reasonable for a metal.

It is expected that the microstructural contribution to the heat capacity should be observed in the high temperature thermal expansion measurements, Figure 4.4. The low temperature range does show a difference in the heating and cooling curves, indicative of a microstructural elastic response, but the response is not seen at high temperatures. The lack of response at the high temperatures suggests that the effective yield strength has decreased. This could be caused by creep. As the temperature is decreased, the increase in yield strength gives a gradual microstructural elastic response. For this reason it is not possible to determine an accurate value for ΔT_y from these data. However, from the observed difference between the thermal expansion coefficient on heating and cooling, 0.5×10^{-6}/K, the magnitude of the response is found. When this value is scaled by the same factor relating the differential thermal expansion to the differential calorimetry (500,000 J/mol), $C_{\mu str} = 0.1$ J $mol^{-1}K^{-1}$, which is similar to the differential calorimetry measurements.

Figure 4.3 shows the final calculated curve labeled "fit," which combines all terms for the differential heat capacity — the elastic-plastic $C_{\mu str}$ (from the ordered alloy only), the harmonic Debye curves (for both phases), and the anharmonic $C_p - C_V$ terms (for both phases). The agreement with experimental data is reasonable, but the high temperature anharmonic effects are underestimated. This extra heat capacity difference could not

originate with the ordering of the disordered phase because this would provide a contribution of the wrong sign. The deviation at high temperatures is likely caused by our oversimplification of the microstructural plastic flow. Deformation processes with $\Delta T_y > 30$ K probably contribute to the heat capacity at higher temperatures. The important point is that it was necessary to include plastic flow to account for the dip in the data at 150 K in Figure 4.3.

The microstructural contribution appears in the scaled thermal expansion data without the use of any new scale factor at high temperatures, Figure 4.3. The standard expression relating thermal expansion and specific heat, Equation 4.2, is derived without considering the effects of microstructure [5]. From classical thermodynamics the linear thermal expansion that results from energy stored in the microstructure can be expressed by

$$\alpha_{\mu str} = \frac{1}{3V}\left(\frac{\partial}{\partial T}\left(\frac{\partial E_{\mu str}}{\partial p}\right)_T\right)_p . \tag{4.12}$$

For clarity we assume a simple expression for the energy stored in the microstructure:

$$E_{\mu str} = \frac{1}{2}\bar{c}\left\langle \bar{\delta}^2 \right\rangle, \tag{4.13}$$

where $\bar{c}$ is the average compliance coefficient and $\left\langle \bar{\delta}^2 \right\rangle$ is the mean square strain stored in the microstructure (this energy is considered in more detail in Chapter 5). Substituting Equation 4.13 into Equation 4.12, a relationship is found between the thermal expansion coefficient and the specific heat due to strain energy stored in the microstructure:

$$\alpha_{\mu str} = \frac{1}{3V\bar{c}}\left(\frac{\partial \bar{c}}{\partial p}\right)_T \frac{1}{2}\bar{c}\left(\frac{\partial \left\langle \bar{\delta}^2 \right\rangle}{\partial T}\right)_p = \frac{1}{3V\bar{c}}\left(\frac{\partial \bar{c}}{\partial p}\right)_T C_{\mu str} \tag{4.14}$$

The pressure derivative in Equation 5.3 can be written in terms of a volume derivative using the bulk modulus, B, resulting in a familiar form,

$$\alpha_{\mu str} = \frac{\gamma_{\mu str}}{3BV} C_{\mu str}. \tag{4.15}$$

This is exactly the same form as the standard Grüniesen relation (Equation 4.2) only with a Grüniesen constant given by

$$\gamma_{\mu str} = -\frac{V}{\bar{c}} \frac{\partial \bar{c}}{\partial V}. \tag{4.16}$$

This gives the volume sensitivity of the elastic constants rather than the usual volume sensitivity of the phonon frequencies. Of course, these quantities are directly related and thus it is expected that $\gamma_{\mu str} \approx \gamma$. Therefore, it is not surprising that only one scale factor was needed to relate the thermal expansion and heat capacity over the entire temperature range.

Evaluating the three terms in the integrand of Equation 4.7, we obtain three contributions to the entropy difference between ordered and disordered Pd_3V. The harmonic and anharmonic vibrational entropy differences are $\Delta S^{dis-ord}_{harmonic} = 0.01 k_B$/atom and $\Delta S^{dis-ord}_{anharmonic} = 0.025$ k_B/atom at 300 K. It is expected that at the ordering temperature (1088 K) the anharmonic effects will be larger. The third part of the heat capacity comes from defect formation, which provides an effective entropy of $\Delta S^{dis-ord}_{defect} = -0.01 k_B$/atom at 300 K. This plastic microstructural contribution to the heat capacity is highly temperature-dependent, and becomes zero at high temperature. These three contributions to the entropy are all expected to be smaller than the configurational entropy of the order-disorder transformation, which could be as large as 0.56 k_B/atom if there is no short-range order in the fcc phase.

Since a significant portion of the entropy comes from the microstructure, it is expected that the stability of the DO_{22} ordered phase will be different in a single crystal. Both theoretical [11] and experimental [12] studies have suggested that coherency stresses can have a significant effect on the phase diagram. In the present study a temperature-dependent strain energy within the microstructure of the ordered phase was observed over a range of temperature. The type of strain energies observed here are expected to be at least as large as the coherency strain energies since the elastic limit is exceeded. A consequence of including plasticity, as was done here, is that the effects on phase stability are expected to be dependent on thermal history.

4.5 Conclusion

A polycrystalline alloy of Pd_3V was prepared in states of DO_{22} chemical order and as a disordered fcc solid solution. Differences in the heat capacity and thermal expansion of these two materials were measured, as were the density, bulk moduli, and thermal expansion coefficients that are needed to assess anharmonic contributions to the heat capacity. When scaled by a positive constant factor, the differential thermal expansion coefficient and the differential heat capacity were the same over the temperature range from 80 - 300 K. The heat capacity was larger for the chemically disordered Pd_3V at both the lowest and highest temperatures in this range. The differential heat capacity curve and ancillary measurements were used to assess the harmonic and the anharmonic contributions to the vibrational entropy, which at 300 K was $S^{dis} - S^{ord}$ = (+0.035± 0.001) k_B/atom, with 70% of this coming from the anharmonic contribution.

The conventional anharmonic contribution, $\Delta(C_p\text{-}C_V)^{dis\text{-}ord}$, was too small to account for the measured differential heat capacity. This anharmonic contribution was also unable to account for a peculiar behavior in the differential heat capacity and differential thermal expansion at 150 K, where both differential curves were nearly zero. We argue that this dip originates with the elastic/plastic response of the polycrystalline microstructure of the ordered alloy during thermal expansion. We propose a model where elastic energy is stored in the polycrystalline microstructure owing to anisotropies in thermal expansion, but this energy is limited by plastic flow of the material.

References

[1] B. Fultz, J. L. Robertson, T. A. Stephens, L. J. Nagel, and S. Spooner, J. Appl. Phys. **79**, 8318 (1996).

[2] B. Fultz, C. C. Ahn, E. E. Alp, W. Sturhahn, and T. S Toellner, Phys. Rev. Lett. **79**, 937 (1997).

[3] H. Frase, B. Fultz, and J. L. Robertson, Phys. Rev. B **57**, 898 (1998).

[4] L. J. Nagel, B. Fultz, J. L. Robertson, and S. Spooner, Phys. Rev. B **55**, 2903 (1997).

[5] T. H. K. Barron, J. G. Collins and G. K. White, Adv. Phys. **29**, 609 (1980).

[7] G. D. Mukherjee, C. Bansal, and A. Chatterjee, Phys. Rev. Lett. **76**, 1876 (1996).

[8] L. Anthony, J. K. Okamoto, and B. Fultz, Phys. Rev. Lett. **70,** 1128 (1993).

[9] A. Maldonado and K. Schubert, Z. Metallkde **55**, 619 in German (1964).

[10] A. E. Dwight, J. W. Downey, and R. A. Conner, Jr., Acta Crystallogr., **14**, 75 (1961).

[11] M. J. Pfeifer and P. W. Voorhees, Metall. Trans. A **22**, 1991 (1991).

[12] M. J. Pfeifer, P. W. Voorhees, and F. S. Biancaniello, Scripta Metall. Mater **30**, 743 (1994).

Chapter Five Microstructural strain energy of α-uranium determined by calorimetry and neutron diffractometry

In this Chapter we take what was learned about the microstructural contribution to the specific heat in Pd_3V and design better experiments to isolate the contribution in uranium. This Chapter focuses on the largest length scale in this thesis.

5.1 Introduction

We report the first direct measurement of the microstructural effects on the heat capacity of α-uranium. Results from prior work imply that microstructure can affect the charge density wave (CDW) transitions in α-uranium. Distinct CDW transitions at 23 K and 37 K can clearly be seen in calorimetry measurements on single crystal uranium, but these transitions are broadened severely in measurements on polycrystalline samples [1]. Work by Hall [2] shows that the constraints on anisotropic thermal expansion in uranium polycrystals either partially inhibit or prevent the CDW transformations, as evidenced by the diminished effects on thermal expansion, specific heat, and electron transport properties.

Recently it has been proposed that an anomaly in the specific heat of Ni_3V and Pd_3V alloys was the result of a microstructural contribution [3, 4]. However, in these experiments, the microstructural contribution was mixed with contributions from both harmonic phonons and anharmonic volume expansion. In this chapter the microstructural contribution in uranium is isolated by subtracting a single crystal specific heat directly from a mass matched polycrystal. In addition, neutron powder diffraction experiments are used to measure the

distribution of elastic strains in the polycrystalline material along various crystallographic directions. The strain distribution data were used to calculate the microstructural strain energy. We find good agreement between the elastic strains that develop in polycrystalline α-uranium during thermal expansion and the reduction in the measured heat capacity as this energy is released. The temperature and energy scales of these phenomena are consistent with measured distortions of the CDW transitions in polycrystalline α-uranium.

5.2 Experimental

Uranium crystals were grown by electro-transport through a molten salt bath of LiCl-KCl eutectic containing on the order of 3 wt. % UCl_3 [5]. The uranium was deposited onto a stainless steel cathode as dendrites in the form of parallelogram-edged platelets. The individual platelets are high purity single crystals of α-uranium. The residual resistivity ratio (RRR) of 115 was about three times higher than any RRR reported previously [1]. Because the uranium was deposited below the α–β transformation temperature, single crystals are strain-free. Strips were cut by spark-erosion cutting, and were cleaned in concentrated HNO_3 and electropolished in H_3PO_4.

Uranium polycrystals were prepared by induction melting the dendritic electro-refined product described above in a BeO crucible under an inert atmosphere. The ingot was melted only once to minimize the risk of contamination from the crucible or the atmosphere. The samples were sectioned directly from the cast ingot with a diamond saw.

Differential heat capacity measurements were performed with a Perkin-Elmer DSC-4 differential scanning calorimeter (DSC) that had been modified by installing its sample head in a liquid-helium dewar [5]. Mass matched ~200 mg samples, one single crystalline and one polycrystalline, were placed in the two sample pans of the DSC. Heat capacity measurements comprised pairs of runs, with the two samples interchanged in the sample pans between runs. The difference in heat capacity was found from the difference of these two sets of runs. Four matched runs were performed to ensure reproducibility. To counteract instrumental drift, runs comprised two pairs of scans over temperature intervals of 30 K, which overlapped by 10 K.

Neutron diffraction patterns were obtained on the Neutron Powder Diffractometer (NPD) at the Lujan Center, Los Alamos National Laboratory. To reproduce the thermal history of the calorimetry measurements, the ~150 g sample was first cooled to 77 K. Diffraction patterns were then obtained at 77 K, 90 K and in steps of 10 K up to 290 K. The sample was equilibrated at each temperature for 10 minutes before acquiring each diffraction pattern. Each diffraction pattern was acquired for 20 minutes. The sample was re-cooled to check for irreversibilities, and measurements were then performed at lower temperatures (40 K, 30 K, and 20 K).

5.3 Results and analysis

The shape of the microstructural contribution showed the basic form expected from the "Elastic-Plastic Model" described by Manley, et al. [4], Figure 5.1. The material showed the release of microstructural strain energy upon heating from liquid nitrogen temperature.

The minimum in strain energy appears to be at about T_0 = 280 K. The temperature change associated with yielding, as defined by Manley, et al. [4], is about ΔT_y = 150 K (see Figure 4.7). Both of these values are much larger than for Pd_3V [4], reflecting the higher yield strain of uranium metal. The low temperature range, however, showed a significant difference from the "Elastic-Plastic Model." With constant thermal and elastic properties, the model predicts linear behavior until about half the Debye temperature (~150 K for uranium), where the thermal expansion coefficients decrease owing to a depopulation of phonons. The data, however, show nonlinear behavior at much higher temperatures. This is probably a result of the strong temperature dependence of the elastic properties of uranium. A more detailed analysis, including the temperature dependence of the thermal and elastic properties, is discussed below.

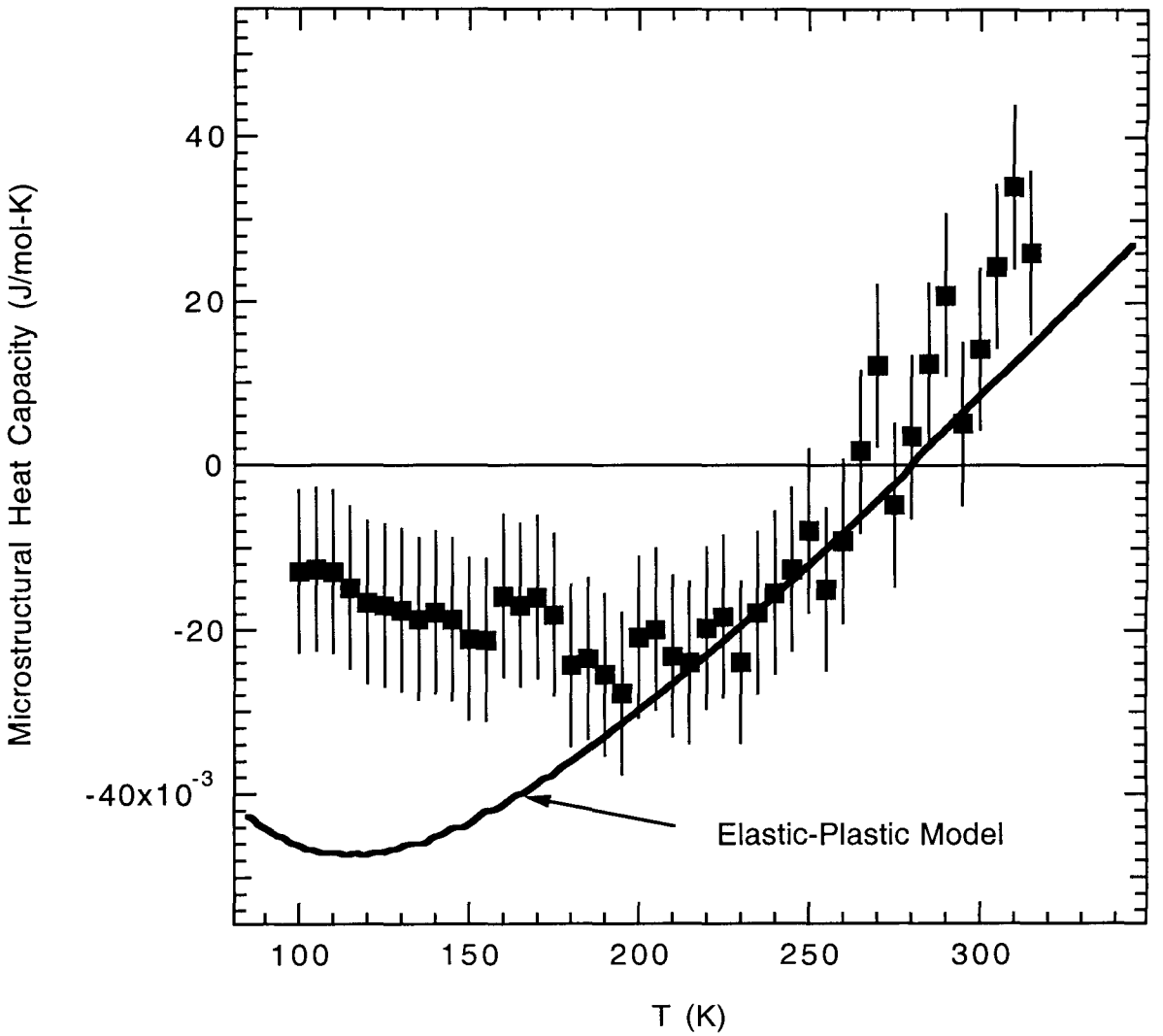

Figure 5.1. Microstructural contribution to the specific heat of uranium. The "Elastic-Plastic Model," described by Manley et al. [3], was scaled arbitrarily and a Debye temperature of 250 K was used. The error bars come from the standard deviation between an average of 4 pairs of runs.

The strain energy per unit volume in an arbitrary stress state is given in matrix notation by [7]

$$u = \frac{1}{2} c_{ij} \varepsilon_i \varepsilon_j \quad (i, j = 1 \ldots 6), \tag{5.1}$$

where c_{ij} is the compliance matrix and ε_i is the strain matrix. The total energy per unit volume in a polycrystal is obtained by averaging over the entire volume. Neutron diffraction provides a sampling of the strain distribution in crystallites in specific orientations determined by Bragg's law. We assume that ε_l in the set of all crystallites in selected by Bragg's law, have a gaussian distribution characterized by

$$\delta_{ij}^2 = \langle \varepsilon_i \varepsilon_j \rangle - \langle \varepsilon_i \rangle \langle \varepsilon_j \rangle, \tag{5.2}$$

where $\delta_{ii}^2 = \sigma^2(\varepsilon_i)$, the variance of ε_i. By multiplying Equation 5.2 by $\frac{c_{ij}}{2}$, considering the appropriate sums, and rearranging terms, a general expression for the average strain energy (Equation 5.1) of this set of crystallites is given by

$$\langle u \rangle \equiv \left\langle \frac{1}{2} c_{ij} \varepsilon_i \varepsilon_j \right\rangle = \frac{1}{2} \left[\langle \sigma_j \rangle \langle \varepsilon_j \rangle + c_{ij} \delta_{ij}^2 \right], \tag{5.3}$$

where the relation between the stress and strain matrix, $\sigma_j = c_{ij} \varepsilon_i$, has been used. The first term in Equation 5.3 originates with the average distortion, and the second term originates with deviations from the average. For a polycrystal with random crystallite orientations the average of this set of crystallites is equivalent to any other orientation and hence it is equivalent to a volume average. Experimentally, each component of Equation 5.3 is determined by an average over a different set of crystallites.

We now show that for an unconstrained polycrystal, the first term in Equation 5.3 vanishes. Consider a plane normal to the x_1 axis cut through an arbitrary polycrystal as shown in Figure 5.2. The force normal to the plane on an area $dx_2 dx_3$ cut by the plane at position x_1 is given by $dF_1(x_1) = \sigma_1(x_1, x_2, x_3)\, dx_2 dx_3$. With no forces applied to the polycrystal along x_1 equilibrium requires

$$F_1(x_1) = \int\int \sigma_1(x_1, x_2, x_3) dx_2 dx_3 = 0. \tag{5.4}$$

Since this condition must hold true for all x_1 in the polycrystal, it follows that

$$\langle \sigma_1 \rangle = \frac{1}{V} \int\int\int \sigma_1(x_1, x_2, x_3) dx_1 dx_2 dx_3 = 0, \tag{5.5}$$

where V is the total volume of the polycrystal. Similar arguments can be made for all of the stress matrix elements, so in general $<\sigma_j> = 0$. Thus, the first term in Equation 5.3 is zero in the case of an unconstrained polycrystal. The microstructural strain energy can then be reduced to

$$\langle u \rangle_{\mu str} = \frac{1}{2} c_{ij} \delta_{ij}^2. \tag{5.6}$$

Like the compliance tensor, the strain-broadening tensor is fourth rank because it connects two second-rank tensors.

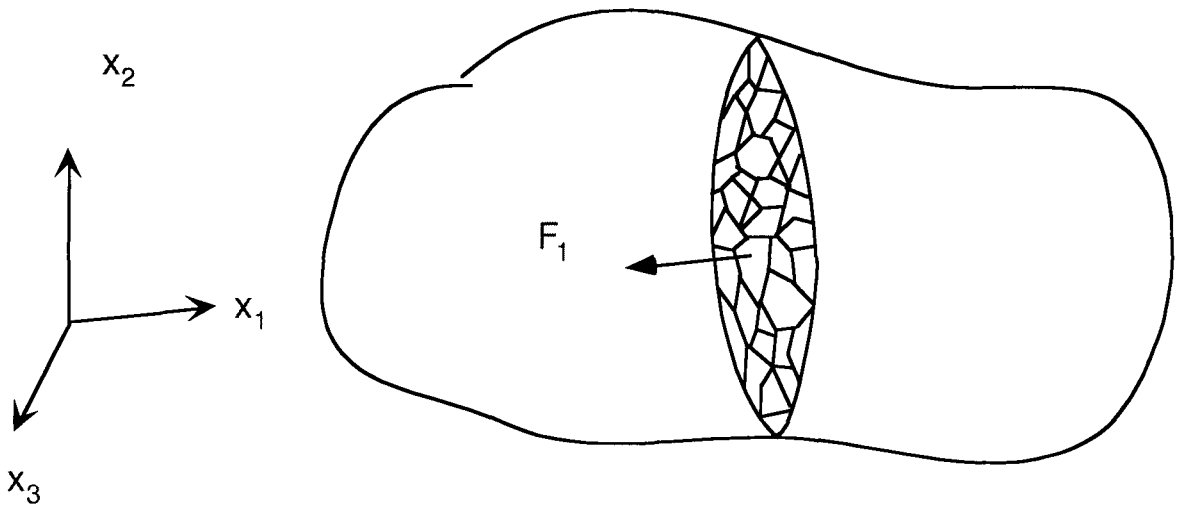

Figure 5.2. Planar cut through an arbitrary unconstrained polycrystal.

Since we need to know only the deviations from the average strain to determine the microstructural strain energy, we have to consider only the strain broadening in the neutron

diffraction data. This is an important simplification because the average strains can be determined accurately only with precise knowledge of the free crystal lattice parameters, which are often sensitive to impurities, defect concentrations, etc.

A measure of the strain-broadening matrix can be extracted from neutron diffraction data using a formalism developed by P. W. Stephens [8]. In this formalism the variance of the diffraction peak widths are fit using [8]

$$\sigma^2(hkl) = \sum_{HKL} S_{HKL} h^H k^K l^L, \tag{5.7}$$

where the coefficients S_{HKL} are restricted by symmetry (6 for orthorhombic) and h, k, and l are the Miller indices. In the following discussion we convert this into strain using

$$S(hkl) = \frac{\sqrt{\sigma^2(hkl)}}{d(hkl)C_{diffraction}}, \tag{5.8}$$

where $d(hkl)$ is the spacing of (hkl) planes and $C_{diffraction}$ is the diffraction constant (converts time-of-flight to Å). The Stephens formalism has been incorporated into the well-known GSAS (General Structure and Analysis Software) Rietveld refinement package [9]. Refinements were fit to all neutron diffraction data in the Le Bail mode [10]. In this mode the diffraction peak intensities are treated as free parameters. Only the peak positions and profiles are fit. A typical fit is shown in Figure 5.3. Using profile function 4 in the GSAS software, the appropriate Stephens strain broadening parameters (6 unique S_{HKL}) were extracted at each temperature. From these parameters the microstrain broadening was calculated as a function of direction using the Mathcad file in Appendix E. The function, $S(hkl)$, fits the strain broadening in all of the peaks simultaneously. To check for consistency, the peak broadening from this function was compared to single peak fits for some easily-

separated peaks, Figure 5.4. The fair agreement was reassuring, although it fell short of what Stevens obtained using much higher resolution synchrotron radiation [8]. The temperature trend of a single peak, shown in the inset of Figure 5.4, was much better.

Three-dimensional representations of the strain broadening function at several temperatures are shown in Figure 5.5. The strain broadening is strongly anisotropic as is expected from the anisotropic elastic and thermal expansion properties of α-uranium [1]. The largest strain broadening is in the [010] direction. This is expected since the Young's modulus is lowest in this direction. Strain broadening increases in the [100] direction at low temperatures, consistent with the softening of c_{11} below about 250 K [11]. The magnitude of the strain broadening decreases with increasing temperature. This agrees with the microstructural specific heat. The microstructural specific heat is negative at low temperatures, implying a decrease in strain energy with increasing temperature.

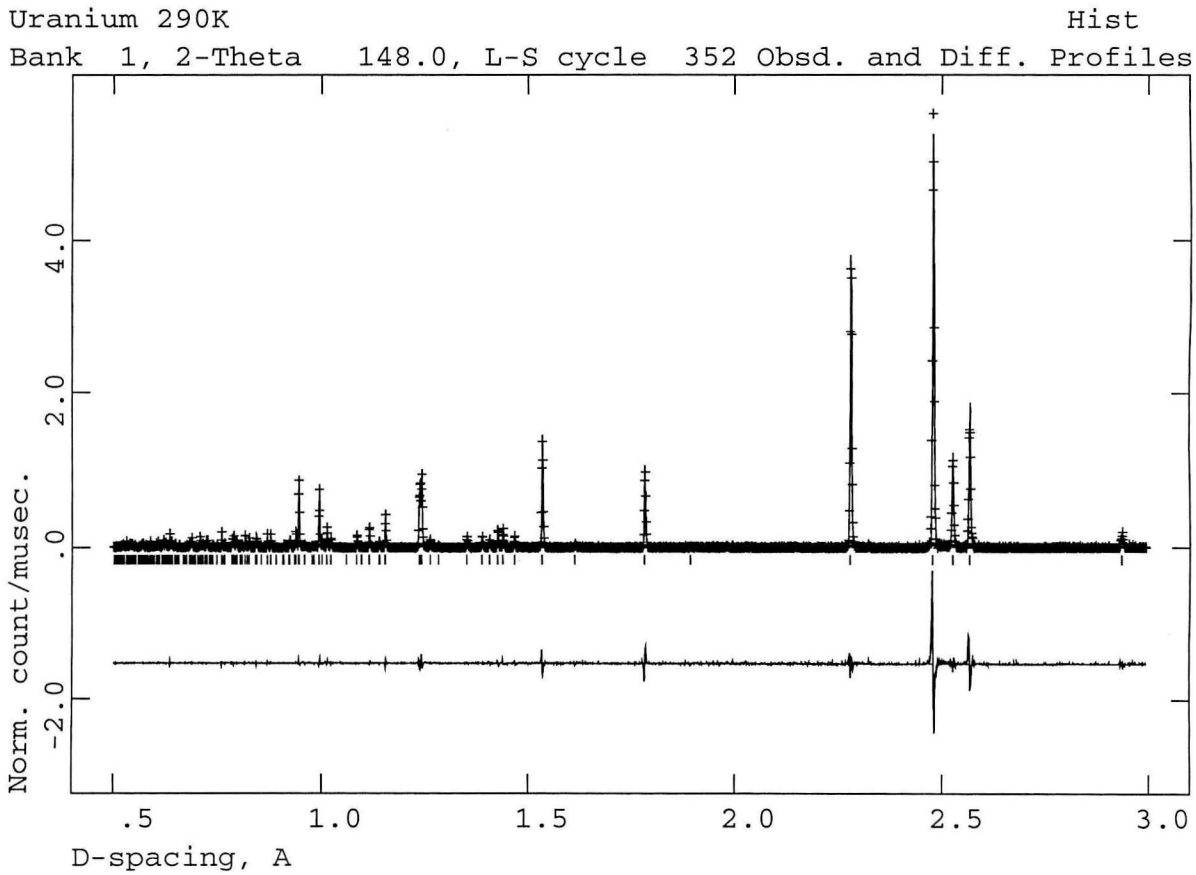

Figure 5.3. GSAS refinement of a uranium diffraction pattern at 290 K.

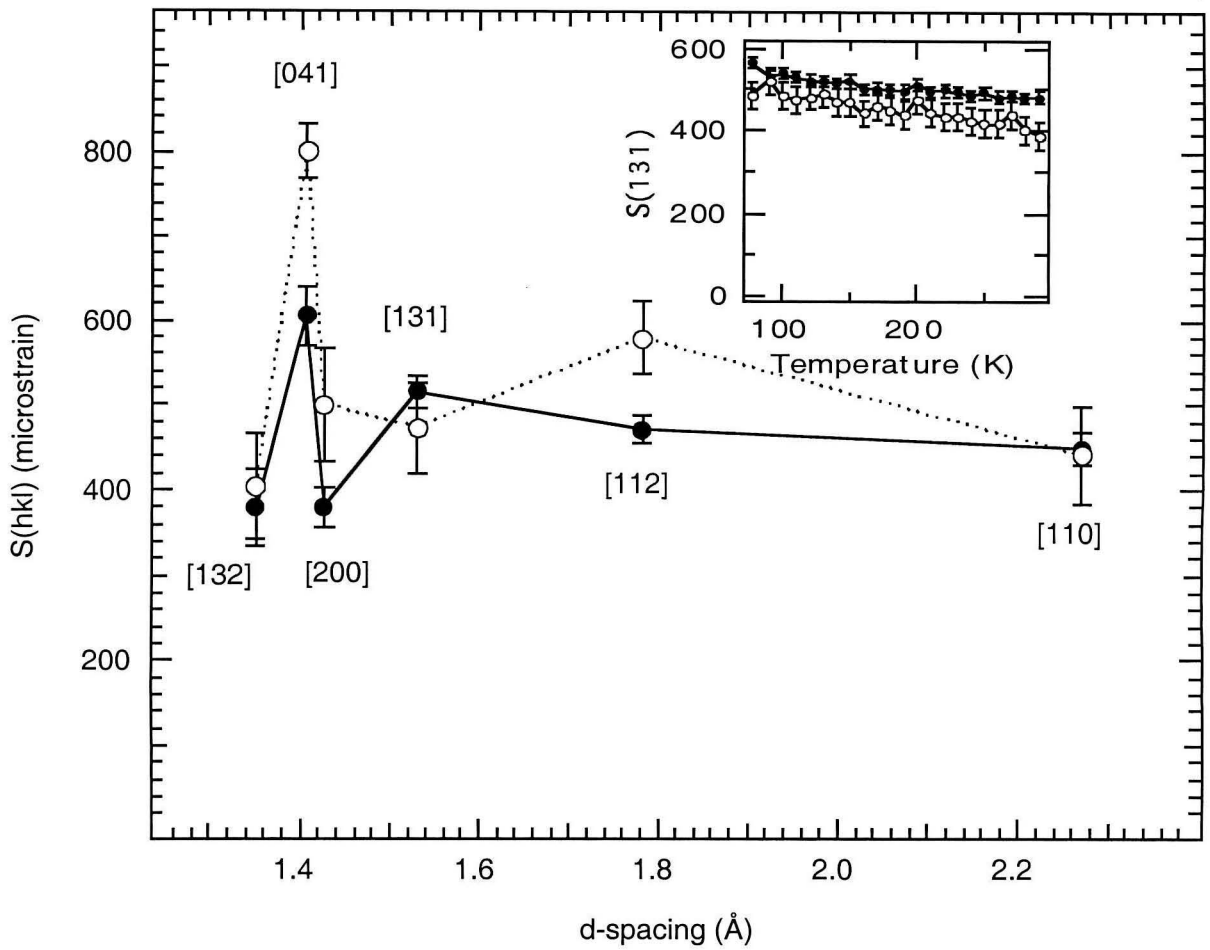

Figure 5.4. Comparison of strain broadening at 190 K calculated from refinement of the entire diffraction pattern, open symbols (○), and from single peak fits, filled symbols (●). Inset shows the temperature dependence of one peak. Units are in microstrain (1000 = 0.1% strain).

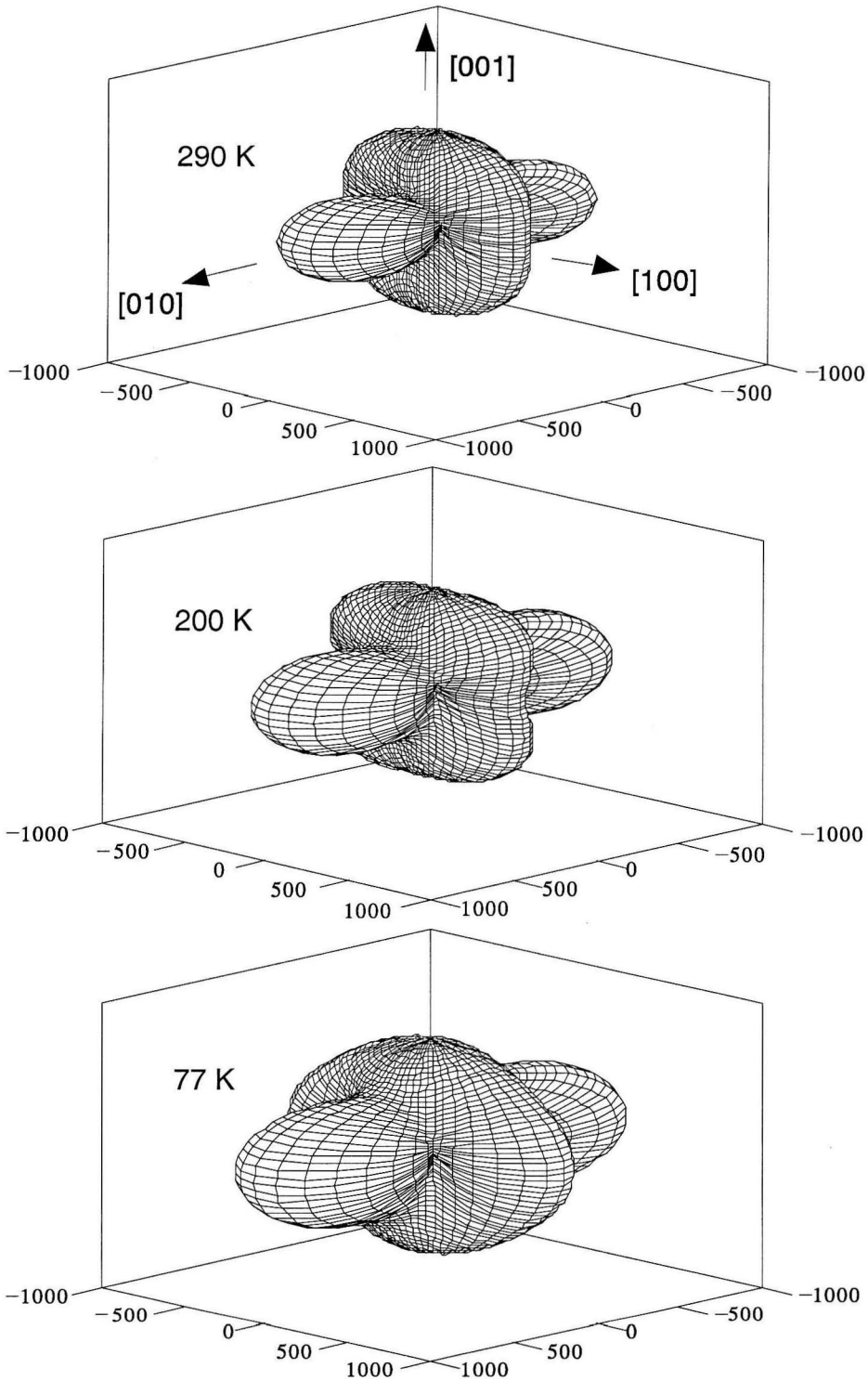

Figure 5.5. The shapes represent the anisotropic microstrain broadening in uranium at several temperatures. Units are in microstrain (1000 = 0.1% strain) and all axes are on the same scale.

5.4 Microstructural strain energy

To determine the strain energy stored in the microstructure we need to determine the strain broadening matrix elements, δ_{ij}^2, corresponding to the nine compliance constants, c_{ij}, allowed by orthorhombic symmetry. The first six components correspond to the variance of the three pure normal strains and the three pure shear strains. They can be written down directly as

$$\begin{aligned} \delta_{11}^2 &= S^2(100) \\ \delta_{22}^2 &= S^2(010) \\ \delta_{33}^2 &= S^2(001) \\ \delta_{44}^2 &= S^2(011) \\ \delta_{55}^2 &= S^2(101) \\ \delta_{66}^2 &= S^2(110) \end{aligned} \tag{5.9}$$

where the numbers in parentheses correspond to the crystallographic *hkl* indices. The remaining non-zero components (corresponding to c_{12}, c_{13}, c_{23}) contain subscripts with $i \neq j$ and thus represent connected variances between strain components (Equation 5.2). The six coefficients obtained in the Stephens formalism cannot be used to determine these strain components. However, these strain components can be estimated using some additional information.

The connected variance terms have the individual strain components subtracted away leaving only the strains in different directions that occur together. Thus, it is a measure of the correlation between strain components in different directions averaged over the volume of the sample. For random intergranular stresses, the strain in direction 1 due to the stress in direction 1 is uncorrelated with the strain in direction 2 due to the stress in direction 2.

However, the strain in direction 1 due to the stress in direction 2 (determined by the Poisson ratio ν_{12}) is correlated with the strain in direction 2 due to the stress in direction 2 and thus contributes to δ_{12}^2. Therefore, assuming the only correlations between strains in different directions comes from the Poisson effect, the remaining components can be written

$$\delta_{ij}^2 = \langle \varepsilon_i \varepsilon_j \rangle - \langle \varepsilon_i \rangle \langle \varepsilon_j \rangle = -\nu_{ij} \left[\langle \varepsilon_j^2 \rangle - \langle \varepsilon_j \rangle \langle \varepsilon_j \rangle \right] = -\nu_{ij} \delta_{jj}^2 \quad (i \neq j). \tag{5.10}$$

Fisher and McSkimin [12] measured all the single crystal elastic constants at room temperature. Some of the resulting properties are most unusual. For example, there is an extraordinarily strong coupling between strains in the [010] direction and the [001] direction with ν_{32}= 0.548. On the other hand, the strains along the [100] direction and the [001] direction are almost uncoupled with ν_{31}= -0.017. This results in the unusual property that [010] is most compressible in uniaxial compression, while [100] is most compressible under hydrostatic compression. Thus, it is important that the coupling terms, Equation 5.8, be included in the strain energy calculation. Fisher [11] measured the temperature dependence of the shear and normal compliance coefficients. The temperature dependence of the off-diagonal components (c_{12}, c_{13}, and c_{23}) is unknown and was thus neglected. Substituting Equation 5.9 and 5.10 into Equation 5.6 with the temperature dependent elastic constants, the strain energy stored in the microstructure was calculated as a function of temperature, Figure 5.6.

For comparison, the microstructural specific heat shown in Figure 5.1 was integrated to give a measure of the strain energy using

$$E_{\mu str} = \int C_{\mu str}(T) dT + E_0, \tag{5.9}$$

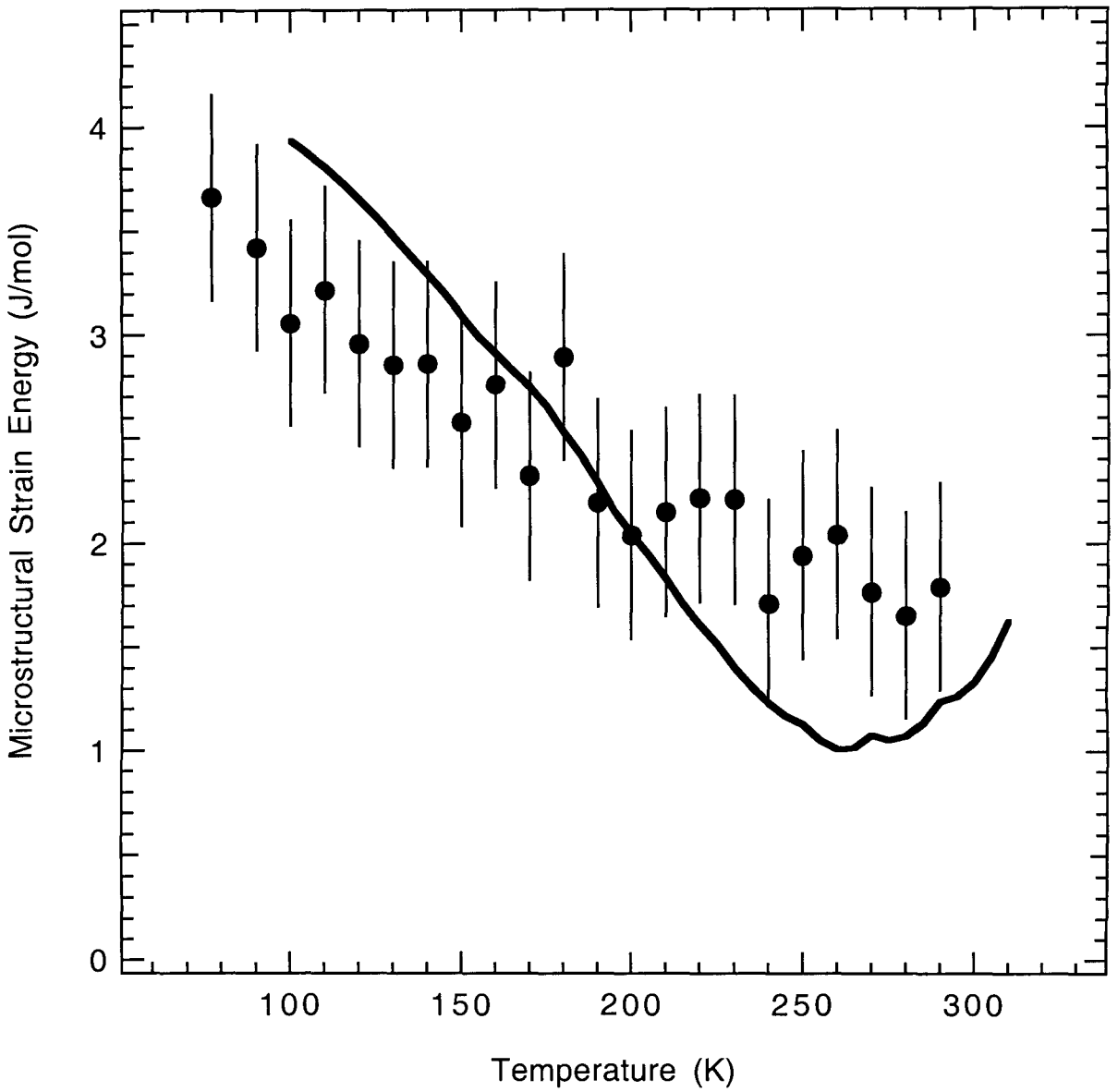

Figure 5.6. Strain energy stored in the microstructure: The points (●) were calculated from strain broadening in neutron diffraction patterns and the solid line comes from integrating the microstructural specific shown in Figure 5.1 and adding an arbitrary constant.

where E_0 is an arbitrary constant set to match the strain energy determined from the strain broadening in the diffraction pattern, Figure 5.6. The origin of E_0 is probably from residual strain fields. The agreement between the neutron diffraction and calorimetry results gives more credibility to both measurements. Errors in the total energy integral are not shown in Figure 5.6 because they depend on the uncertainty in E_0 and the systematic accumulation of errors through integration. For example, if E_0 is known exactly at some temperature, say T_0, then the error in energy by integrating away from T_0 is given by $\Delta E_{\mu str} = \Delta C_{\mu str} (T - T_0)$ where $\Delta C_{\mu str}$ = 0.01 J/mol-K the error in the specific heat measurement. Thus, assuming E_0 = 1 J/mol at 280 K, then the energy at 77 K would be (4±2) J/mol-K. The strain energy calculated from the diffraction measurements give a more precise measure at 77 K of (3.7±0.5) J/mol-K.

Attempts were made to measure how the strain energy stored in the microstructure changed below the CDW transitions by measuring the diffraction pattern at 40 K, 30 K and 20 K. However, there was no clear indication that the CDW transition had occurred. Specifically, Barrett et al. [13] observed a sudden increase in the a (0.2%) and b (0.05%) lattice parameters and a decrease in c (-0.09%) in single crystals. Our measurements, on the other hand, showed no significant changes (other than the usual continuous thermal contractions). Our results, therefore, agree with earlier measurements suggesting that the CDW transformations are either suppressed or completely smeared out in temperature in the presence of the microstructural constraints on the anisotropic thermal expansions/contractions [1, 2].

5.5 Elastic strains and the charge density wave transitions

The magnitude of the strain energy stored in the microstructure, (3.7±0.5) J/mol-K at 77 K, is comparable to the latent heats of the CDW transitions. The latent heats of these 37 K and 22 K transitions are 2.08 and 1.38 J/mol, respectively [14]. Since these transitions are accompanied by lattice strains, it is therefore not surprising that the transitions are either smeared out in temperature or suppressed by constraints imposed by the microstructure.

The expansion of the a-axis and b-axis during the CDW transformations [13] would tend to undo some of the strains that built up on cooling because the strains that build up on cooling originate with contractions along these directions. Specifically, in single crystals the CDW transformation strains cause the lattice parameters to recover to their values at about 180 K for the a-axis and about 300 K for the b-axis [13]. Therefore, one would expect that in regions dominated by thermal strains along [100] and [010], the strain energy would favor the transformations. Therefore, these regions may in fact transform at a higher temperature than in the single crystal. On the other hand, the contraction of the c lattice parameter during the transformation would tend to further increase the strain energy. Therefore, the opposite affect would be expected in grains dominated by strains along [001]. Of course, the actual strain energy depends on all of the strain components in a given region. In a polycrystal with randomly oriented grains we would expect a distribution of strain energies either gained or lost in the transitions and therefore a distribution of transition temperatures. This has the effect of smearing out the effective CDW transition temperature seen in the polycrystal.

The spread of the transition temperatures depends on the strain energy gained or lost in the transition and the free energy change in the free crystal. To predict the range of this spread, we would need to add the strain energy gained or lost in a region to the free energy difference between the phases in the single crystal and then recalculate a new local equilibrium temperature (if there is one). Presently, we do not have enough information to do this because we do not know how the free energy difference of the single crystal scales with temperature. For example, if the entropy difference was primarily electronic, then the difference would scale linearly with temperature. If it where vibrational, the entropy difference would scale roughly as T^3 in the lower temperature range.

The elastic energy in the polycrystalline microstructure depends on the thermal history of the material. We have made the above arguments based on the strains induced by our particular thermal path. It is conceivable that different results could be found with different heat treatments. In particular, it would make sense to try and find a way to minimize the strain energy stored in the microstructure near the phase transition. This may allow these transitions to be studied in more detail in polycrystalline samples.

5.6 Concluding remarks

The results presented in this Chapter not only confirm the mechanism for microstructural specific heat described in Chapter 4, but also show that it is possible to deduce the same results from neutron diffraction. Estimated strain energies stored in the microstructure showed good agreement between calculations from the diffractometry and

calorimetry. It is now clear that the strain energies stored in the microstructure of uranium have a significant affect on the temperatures of the low temperature charge density wave transitions.

References

[1] G. H. Lander, E. S. Fisher, and S. D. Bader, Adv. Phys. **43**, 1-111 (1994).

[2] R. O. A. Hall, Inst. Phys. Conf. Series (Lond.) **27**, 60 (1978).

[3] L. J. Nagel, B. Fultz, J. L. Robertson, and S. Spooner, Phys. Rev. B **55**, 2903 (1997).

[4] M. E. Manley, B. Fultz, and L. J. Nagel, Phil. Mag. B. **80**, 1167 (2000).

[5] C. C. McPheeters, E. C. Gay, P. J. Karell, and J. P. Ackerman, J. Met. **49**, p. N7 (1997).

[6] L. Anthony, J. K. Okamoto, and B. Fultz, Phys. Rev. Lett. **70,** 1128 (1993).

[7] J. F. Nye, *Physical Properties of Crystals: Their Representation by Tensors and Matrices* (Oxford Science Publications, 1989) p. 137.

[8] P. W. Stephens, J. Appl. Cryst. **32**, 281-289 (1999).

[9] A. C. Larson and R. B. Von Dreele, GSAS – General Structure Analysis System. Los Alamos National Laboratory Report LAUR 86-748.

[10] A. Le Bail, H. Duroy, and J. L. Fourquet, Mater. Res. Bull. **23**, 447-452 (1988).

[11] E. S. Fisher, J. Nucl. Mater. **18**, 39 (1966).

[12] E. S. Fisher and H. J. McSkimin, J. Appl. Phys. **29**, 1473 (1958); Phys. Rev. **124**, 67 (1961).

[13] C. S. Barrett, M. H. Mueller, and R. L. Hittermann, Phys. Rev. **129**, 625.

[14] J. Crangle and J. Temporal, J. Phys. F **3**, 1097 (1973).

Chapter Six Future work

At this point it is clear that the thermodynamics of metals and alloys depend on phenomena across a wide range of length scales. We have found many interesting contributions to phase stability from electronic excitations to strain energy produced at the microstructural scale (from the forces that grains exert on one another). There is still considerable work remaining. In this Chapter some future work is outlined.

6.1 Phonon softening in the absence of anharmonicity

In Chapter 2 the search for the nature of the vibrational softening in uranium was motivated in part by the failure of the quasiharmonic approximation to explain the phonon softening from thermal expansion. Specifically, there was about an order of magnitude more entropy from phonon softening than needed to account for the elastic energy generated from volume expansion. This argument can be reformulated in terms of the specific heat. First, express the entropy as

$$S = \sum_j S_j \cong \sum_j -3k_B \ln\left(\frac{\hbar\omega_j(V)}{kT}\right). \tag{6.1}$$

Then take the temperature derivative at constant pressure,

$$C_p^{quasi} = T\left(\frac{\partial S^{quasi}}{\partial T}\right)_p = \sum_j T\frac{\partial}{\partial T}\left(-3k_B \ln\left(\frac{\hbar\omega_j}{k_B T}\right)\right)_p \tag{6.2}$$

$$= 3k_B\left(1+\delta_p T\right)$$

where

$$\delta_p = \sum_j -\frac{1}{\omega_j}\left(\frac{\partial \omega_j}{\partial T}\right)_p \tag{6.3}$$

Considering only the vibrational contribution, the constant pressure specific heat can be written,

$$C_p^{anh} = 3k_B + 9Bv\alpha^2 T. \tag{6.4}$$

Comparing Equation 6.4 and Equation 6.2 it is clear that under the assumptions of the quasiharmonic approximation $9Bv\alpha^2 = 3k_B\delta_p$. These terms were calculated for several different materials and are shown in Table 6.1. The first three elements (Pd, Ni, and Cu) were calculated using the temperature dependence of the phonon DOS published in the Landolt-Bornstein series [1]. The remaining Pu phases and α-U were calculated using the temperature dependence of the Debye temperature extracted from neutron diffraction data [2]. For both Pu and U the discrepancy is quite large, suggesting further study of the phonon contribution to the equation of state of both materials.

Table 6.1. Excess specific heat above $3k_B$ from volume expansion (column 1) and from phonon softening (column 2).

Material	$9Bv\alpha^2$ ($10^{-4}$$k_B$/atom-K)	$3k_B\delta_p$ ($10^{-4}$$k_B$/atom-K)
Pd	2.4	3.2
Ni	2.3	2.7
Cu	2.8	3.2
α-Pu	6.2	11.8
δ-$Pu_{0.95}Al_{0.05}$	2	10.6
α-U	2.5	23.4

In the case of U, the effects of pressure on the vibrational spectrum could be explored. At ambient pressure the vibrational and electronic entropy have been shown to be significant. However, the origin of the electronic entropy is not understood. The origin of

the electronic contribution could be explored by measuring the partial electronic density of states using photoelectron spectroscopy (PES). For Pu the temperature dependence of the vibrational spectra in all of its phases should be measured. Measured vibrational spectra measurements could be used to determine the vibrational entropy, and this could be compared with calorimetry measurements in the literature. The electronic contribution to the entropy will be the difference between the vibrational entropy and the total entropy determined by calorimetry. It is expected that a significant electronic contribution will also be found in Pu and could be explored using the same techniques as with U and Ce.

This work will help lay the groundwork for more accurate first principles calculations of the behavior of these metals. For example, PES may give the information needed to take into account the temperature-dependence of the force constants. The understanding of such complex materials will also lead to a more general understanding of other materials.

6.2 Crystal-field splitting and Kondo spin-fluctuations

We have shown that both the crystal-field splitting and Kondo spin-fluctuations make a significant contribution to both β-cerium and γ-cerium at low temperatures. However, both were small at the transition temperature so the difference made only a minor contribution to the transition. In the case of α-cerium, however, the transition is at a much lower temperature (100 K). Also, α-cerium has no localized f-electron and thus both the spin fluctuation and the crystal field contribution should be zero in this phase. Therefore, it

seems likely that a detailed study of the entropy change of these transitions (α– to β-cerium or α- to γ-cerium) will reveal a significant contribution from these degrees of freedom.

6.3 Strain energy stored in microstructures

The strain energy stored in the microstructure of uranium was large enough to affect the low temperature CDW transitions. However, the range of transition temperatures could not be worked out without prior knowledge of the components of the free energy differences between the low temperature phases. Unfortunately, it is the spread in the transition temperatures seen in polycrystals that makes it so difficult to study these transitions. We could not, for example, perform the kind of detailed analysis that was performed for cerium in Chapter 3.2 because in polycrystalline uranium we are likely to have some mixture of transformed and untransformed uranium well below the transition temperature. In cerium the strain problem was overcome by thermal cycling the sample (although it is not entirely clear why this works). A more detailed study including microstructural modeling and modeling of the electronic and phonon contributions is likely to contribute to an understanding of, and possibly allow the control of, the CDW transitions in uranium.

References

[1] P. H. Dederichs, H. Schober, and D. J. Sellmyer, in *Numerical Data and Functional Relationships in Science and Technology*, edited by K. –H. Hellwege and J. L. Olsen, Landolt-Bornstein, New Series, Group III, Vol. III/13a (Springer-Verlag, Berlin, 1981).

[2] A. C. Lawson, B. Martinez, J. A. Roberts, and B. I. Bennett, Phil. Mag. B **80**, 53 (2000).

Appendix A Mathcad files used to determine multiphonon scattering

1 Phonon Scattering Calculation

$Z := READPRN(UDOS)$ input DOS

$Se := READPRN(U300KS)$ data to be compared with

$r := 0, 1 .. rows(Z) - 1$

$$Z_{r,1} := \left[\sum_{m=0}^{rows(Z)-2} Z_{m,1} \cdot \left(Z_{m+1,0} - Z_{m,0}\right) \right]^{-1} \cdot Z_{r,1}$$ normalizes the DOS

$h := 1$ $M := 238$ atomic mass

$E := 3.55$ meV incident energy

$\Delta E(\omega) := \left[(1 - 0 \cdot 0.0753 \cdot h \cdot \omega) + 0 \cdot 0.00195 \cdot (h \cdot \omega)^2 \right]$ meV insturment resolution function

$kT := 25$ meV temperature

$\theta 1 := 0.61$ to $\theta 2 := 2.32$ detector angle range (radians)

$$msd := \sum_{m=0}^{rows(Z)-2} \frac{Z_{m,1}}{Z_{m,0}} \cdot \coth\left[h \cdot \frac{Z_{m,0}}{2 \cdot kT} \right] \cdot \left(Z_{m+1,0} - Z_{m,0}\right)$$ (mean square displacement) *2M/h^2

time-dependent correlation function

$$b := \frac{\pi}{\left(Z_{1,0} - Z_{0,0}\right) \cdot 606.5}$$

$$G(t) := \sum_{m=0}^{rows(Z)-2} \frac{Z_{m,1}}{Z_{m,0}} \cdot \left[i \cdot \sin\left(Z_{m,0} \cdot t\right) + \cos\left(Z_{m,0} \cdot t\right) \cdot \coth\left[h \cdot \frac{Z_{m,0}}{2 \cdot kT} \right] \right] \cdot \left(Z_{m+1,0} - Z_{m,0}\right)$$

$n := 0, 1 .. 1214$

$t_n := b \cdot (n - 606.5)$

$G_n := G(t_n)$

single phonon dynamic structure factor convoluted with resolution function

$$D(\theta, \omega) := \frac{1}{2 \cdot \pi \cdot h} \cdot \exp\left[\frac{-1.008}{M} \cdot E \cdot \left[2 - h \cdot \frac{\omega}{E} - 2 \cdot \sqrt{1 - h \cdot \frac{\omega}{E}} \cdot \cos(2 \cdot \theta) \right] \cdot msd \right]$$

$$S(\theta, \omega) := D(\theta, \omega) \cdot \sum_{k=0}^{1213} \exp\left[-(t_k)^2 \cdot \frac{\Delta E(\omega)^2}{h^2} \right] \cdot \exp\left[-i \cdot \frac{\omega}{h} \cdot t_k \right] \cdot G_k \cdot \frac{1.008}{M} \cdot E \cdot \left[2 - h \cdot \frac{\omega}{E} - 2 \cdot \sqrt{1 - h \cdot \frac{\omega}{E}} \cdot \cos(2 \cdot \theta) \right] \cdot \left(t_{k+1} - t_k\right)$$

$m := 10$

$$S1(\omega) := \frac{1}{\theta 2 - \theta 1} \cdot \sum_{n=0}^{m} S\left[\theta 1 + n \cdot \frac{(\theta 2 - \theta 1)}{m}, \omega \right] \cdot \frac{(\theta 2 - \theta 1)}{m}$$

Output data

$r := 0, 1 .. rows(Se) - 1$

$E_r := Se_{r,0}$

$S1_r := S1(E_r)$

Total Scattering Calculation

$Z := READPRN(UDOS)$ input DOS

$Se := READPRN(U300KS)$ data to be compared with

$r := 0, 1 .. rows(Z) - 1$

$$Z_{r,1} := \left[\sum_{m=0}^{rows(Z)-2} Z_{m,1} \cdot \left(Z_{m+1,0} - Z_{m,0} \right) \right]^{-1} \cdot Z_{r,1}$$ normalizes the DOS

$h := 1$ $M := 238$ atomic mass

$E := 3.55$ meV incident energy

$\Delta E(\omega) := \left[(1 - 0 \cdot 0.0753 \cdot h \cdot \omega) + 0 \cdot 0.00195 \cdot (h \cdot \omega)^2 \right]$ meV insturment resolution function

$kT := 25$ meV temperature

$\theta 1 := 0.61$ to $\theta 2 := 2.32$ detector angle range (radians)

$$msd := \sum_{m=0}^{rows(Z)-2} \frac{Z_{m,1}}{Z_{m,0}} \cdot \coth\left[h \cdot \frac{Z_{m,0}}{2 \cdot kT} \right] \cdot \left(Z_{m+1,0} - Z_{m,0} \right)$$ (mean square displacement) *2M/h^2

time-dependent correlation function $b := \dfrac{\pi}{(Z_{1,0} - Z_{0,0}) \cdot 606.5}$

$$G(t) := \sum_{m=0}^{rows(Z)-2} \frac{Z_{m,1}}{Z_{m,0}} \left[i \cdot \sin\left(Z_{m,0} \cdot t \right) + \cos\left(Z_{m,0} \cdot t \right) \cdot \coth\left[h \cdot \frac{Z_{m,0}}{2 \cdot kT} \right] \right] \cdot \left(Z_{m+1,0} - Z_{m,0} \right)$$

$n := 0, 1 .. 1214$

$t_n := b \cdot (n - 606.5)$

$G_n := G(t_n)$

total dynamic structure factor convoluted with resolution function

$$D(\theta, \omega) := \frac{1}{2 \cdot \pi \cdot h} \cdot \exp\left[\frac{-1.008}{M} \cdot E \cdot \left[2 - h \cdot \frac{\omega}{E} - 2 \cdot \sqrt{1 - h \cdot \frac{\omega}{E}} \cdot \cos(2 \cdot \theta) \right] \cdot msd \right]$$

$$S(\theta, \omega) := D(\theta, \omega) \cdot \sum_{k=0}^{1213} \exp\left[-(t_k)^2 \cdot \frac{\Delta E(\omega)^2}{h^2} \right] \cdot \exp\left[-i \cdot \frac{\omega}{h} \cdot t_k \right] \cdot \exp\left[G_k \cdot \frac{1.008}{M} \cdot E \cdot \left[2 - h \cdot \frac{\omega}{E} - 2 \cdot \sqrt{1 - h \cdot \frac{\omega}{E}} \cdot \cos(2 \cdot \theta) \right] \right] \cdot \left(t_{k+1} - t_k \right)$$

$m := 10$

$$St(\omega) := \frac{1}{\theta 2 - \theta 1} \cdot \sum_{n=0}^{m} S\left[\theta 1 + n \cdot \frac{(\theta 2 - \theta 1)}{m}, \omega \right] \cdot \frac{(\theta 2 - \theta 1)}{m}$$

Output data

$r := 0, 1 .. rows(Se) - 1$

$E_r := Se_{r,0}$

$St_r := St(E_r)$

Appendix B Anisotropy error in phonon DOS measurement

The only error from anisotropy in experiments on isotropic polycrystals comes from a Debye-Waller factor weighting of the measured phonon DOS. It is well-known, however, that an isotropic Debye-Waller factor is a good approximation [1], especially at low temperatures and modest Q where the Debye-Waller factor is close to 1 for all directions of Q.

To settle definitively this point about the anisotropy of the Debye-Waller factor, we have obtained results from our lattice dynamics calculation. The anisotropic Debye-Waller factor second rank tensor in orthorhombic symmetry has three independent coefficients with principal axes parallel to the crystallographic a, b, and c axes. The three diagonal components ($\langle u_x^2 \rangle$, $\langle u_y^2 \rangle$, and $\langle u_z^2 \rangle$) can be determined from the projection of the partial phonon DOS along each of the principal directions. Using the force constant model of Crummett et al. [2] the partial DOS projected along each of the principal axes was calculated and the resulting components are $\langle u_x^2 \rangle$ = 0.015 Å^2, $\langle u_y^2 \rangle$ = 0.0047 Å^2, and $\langle u_z^2 \rangle$ = 0.0056 Å^2 at room temperature. The Q-range varies with energy and angle, but has a range from about Q = 1-3 Å^{-1} for the FCS instrument. The resulting Debye-Waller factors at the average Q = 2 Å^{-1} are $\exp(-Q^2\langle u_x^2 \rangle)$ = 0.941, $\exp(-Q^2\langle u_y^2 \rangle)$ = 0.981, and $\exp(-Q^2\langle u_z^2 \rangle)$ = 0.978. The average in the isotropic approximation is $\exp(-Q^2\langle u^2 \rangle/3)$ =0.967. In the low energy range the true average weighting for anisotropic α-U is about 0.960. This anisotropic weighting is a mere 0.7% lower than the isotropic value. At the highest energies where the x-component goes to zero, the result is only 1.3% higher than the isotropic value. Assuming the same lattice dynamics, this error is 3% at the highest temperature of the α-phase (913 K).

The error in the DOS itself is also negligible, as shown in the attached Figure A.1. Although the anisotropy of the phonons is not known for the tetragonal β-phase, we can say that the Debye-Waller factors themselves are close to 1, based on the measured DOS. The high temperature γ-phase is cubic, so there can be no anisotropy error for γ-U.

References

[1] S. W. Lovesey, *Theory of Neutron Scattering from Condensed Matter*, Oxford University Press, 1987, p. 109.

[2] W. P. Crummett, H. G. Smith, R. M. Nicklow, and N. Wakabayashi, Phys. Rev. B. **19**, 6028 (1979).

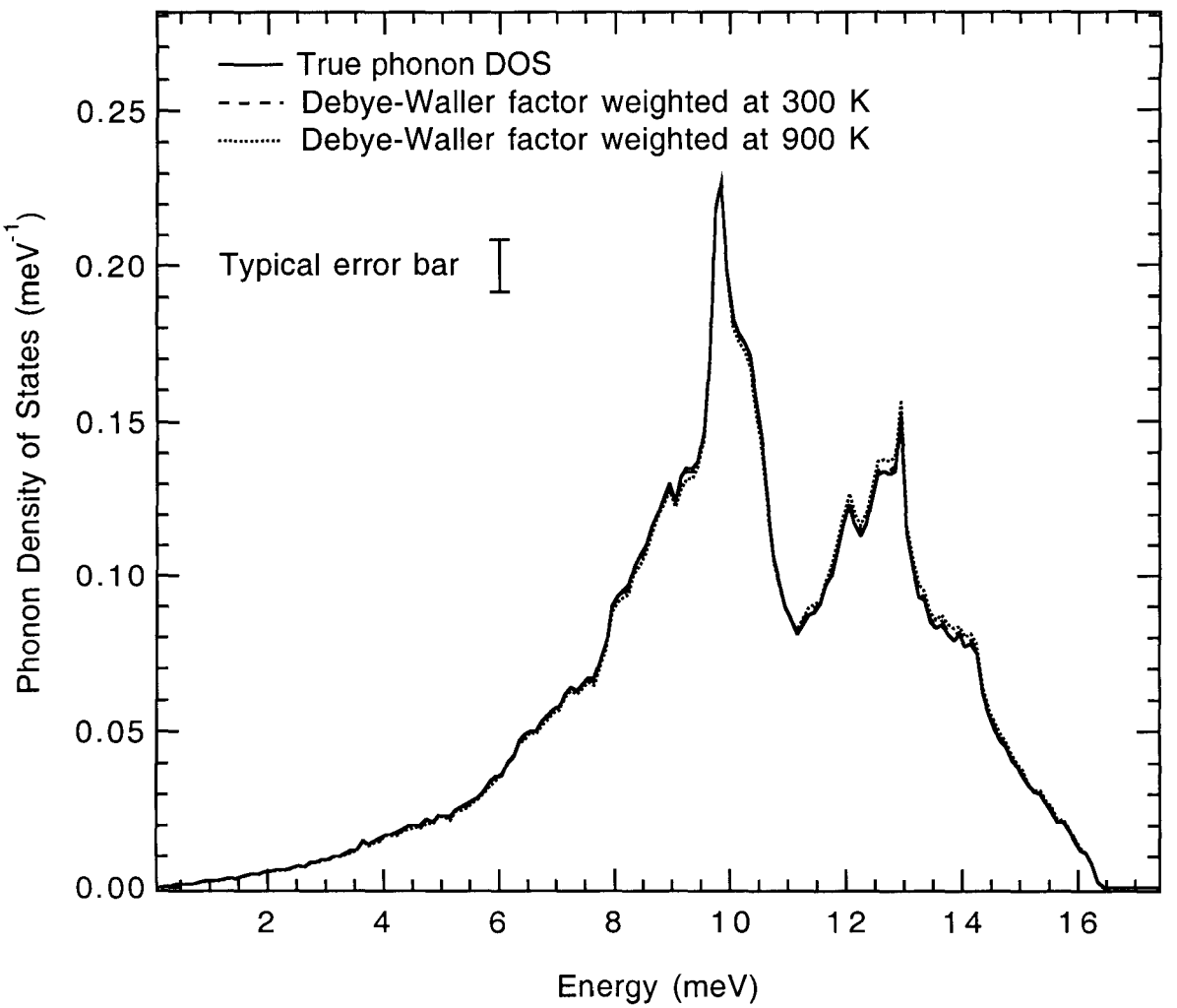

Figure A.1. Phonon DOS of α-uranium and the effect of anisotropic Debye-Waller factor weighting on the experimentally measured DOS. The difference between the black curve and the other two is the error of assuming isotropic Debye-Waller factors. The typical error bar was taken from the FCS instrument around 10 meV at 433 K.

Appendix C Comparison of harmonic and anharmonic oscillators

Runge - Kutta (Order Four)

Potential Coefficients:

$c := 5$ eV/A^2

$g1 := 28$ eV/A^3

$f := 10$ eV/A^4 $Eanh := 0.025$ eV $M := 1$

$$yanh := \begin{bmatrix} 0 \\ \sqrt{2 \cdot \frac{Eanh}{M}} \end{bmatrix}$$ initial conditions

$t0 := -40$

$tf := 40$

$npoints := 1000$ $r := 0, 1 .. npoints$ $l := 0, 1 .. \frac{npoints}{6}$

$$D1(t, y) := \begin{bmatrix} y_1 \\ \frac{\left[-2 \cdot c \cdot (y_0) + 3 \cdot g1 \cdot (y_0)^2 - 4 \cdot f \cdot (y_0)^3\right]}{M} \end{bmatrix}$$ Anharmonic problem

$Solanh := rkfixed(yanh, t0, tf, npoints, D1)$

$$kT := M \cdot \sum_{n=0}^{npoints} \frac{(Solanh_{n,2})^2}{npoints}$$ Determines Temperature $kT = 0.019$

Note:

Eanh > kT

Eh = kT

$$yh := \begin{bmatrix} 0 \\ \sqrt{2 \cdot \frac{kT}{M}} \end{bmatrix}$$

$$D2(t, y) := \begin{bmatrix} y_1 \\ -2 \cdot c \cdot \frac{y_0}{M} \end{bmatrix}$$ Harmonic problem

$Solh := rkfixed(yh, t0, tf, npoints, D2)$

Phase Space

Area

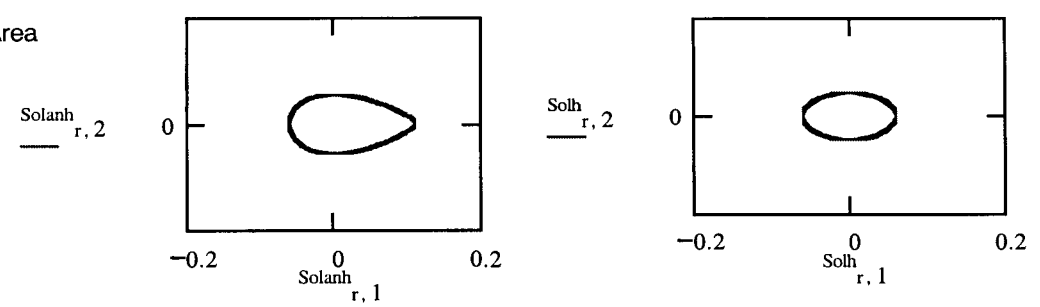

$$Aanh_l := \sum_{n=0}^{l} Solanh_{n,2} \cdot \left(Solanh_{n+1,1} - Solanh_{n,1}\right)$$

$$Ah := \pi \cdot \frac{kT}{\sqrt{c \cdot \frac{M}{2}}}$$

$Ah = 0.037$

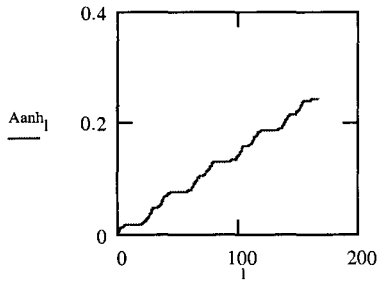

Phase space entropy difference calculation:

$$\Delta Sps := 3 \cdot \ln\left[\frac{.07396 - .01816}{Ah}\right]$$

$\Delta Sps = 1.25$

Position Versus Time

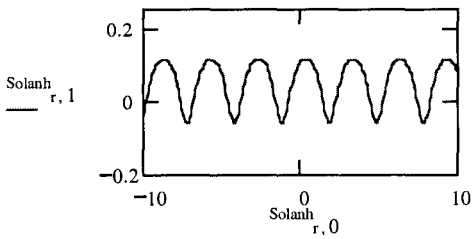

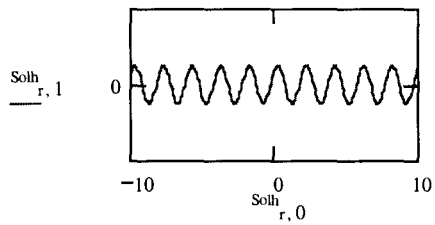

Velocity Versus Time

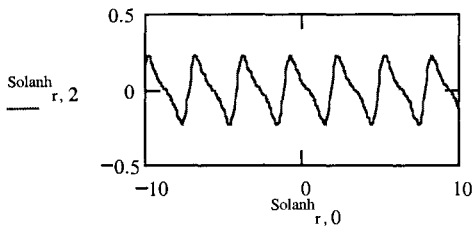

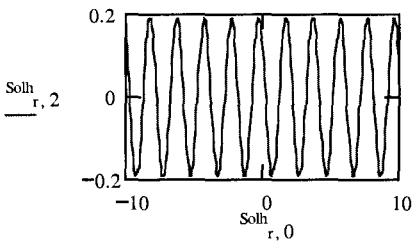

$\sigma := 15 \qquad w := 0, 1 .. 200$

Power Spectrum Analysis

$$Zh(\omega) := \sum_{n=0}^{npoints-1} Solh_{n,2} \cdot \exp\left(-i \cdot \omega \cdot Solh_{n,0}\right) \cdot \exp\left[\frac{-\left(Solh_{n,0}\right)^2}{\sigma^2}\right] \cdot \frac{(tf - t0)}{npoints}$$

$eh_w := 0.05 \cdot w$

$$gh_w := \left(\left|Zh\left(eh_w\right)\right|\right)^2 \qquad Nh := \sum_{m=0}^{rows(eh)-2} gh_m \cdot \left(eh_{m+1} - eh_m\right)$$

$$gh_w := \frac{1}{Nh} \cdot gh_w$$

$$Zanh(\omega) := \sum_{n=0}^{npoints-1} Solanh_{n,2} \cdot \exp\left(-i \cdot \omega \cdot Solanh_{n,0}\right) \cdot \exp\left[\frac{-\left(Solanh_{n,0}\right)^2}{\sigma^2}\right] \cdot \frac{(tf - t0)}{npoints}$$

$$ganh_w := \left(\left|Zanh\left(eh_w\right)\right|\right)^2$$

$$Nanh := \sum_{m=1}^{rows(eh)-2} ganh_m \cdot \left(eh_{m+1} - eh_m\right)$$

$$ganh := \frac{1}{Nanh} \cdot ganh$$

$kT = 0.019$

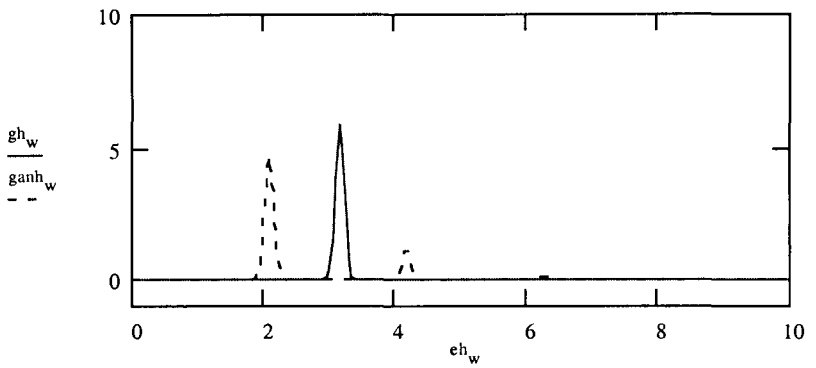

Entropy difference based on power spectra interpreted in the harmonic approximation:

$$\Delta S := \sum_{m=1}^{rows(eh)-2} -3\cdot\left[\left(ganh_m - gh_m\right)\cdot\left(eh_{m+1} - eh_m\right)\cdot\ln\left(eh_m\right)\right]$$

$\Delta S = 0.795$ k/atom

True entropy difference: $\Delta Sps = 1.25$ k/atom (from phase space)

Error comes from additional peak(s) at higher energies. Correct value is given in the quasiharmonic approximation by using first dashed peak only (renormalized)!

Appendix D Analytic solution to the deflection of a bi-metallic strip

Binding two states of a material together into a bi-metallic strip makes it possible to measure very small differences in thermal expansion between the two states. A small thermal expansion difference induces a curvature in the bi-metallic strip. Here we derive an expression for the curvature and show how this can be further amplified using an optical lever.

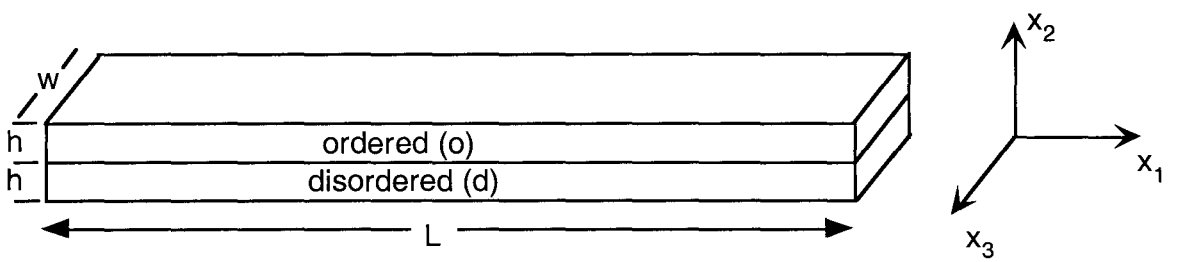

Figure D.1. Bi-metallic strip dimensions.

I. Start by constraining the beam shown in Figure 1 to be flat.

For equal cross sections, force balance requires the stresses to balance:

$$\begin{aligned} \sigma_{11}^{o} &= -\sigma_{11}^{d} \\ \sigma_{33}^{o} &= -\sigma_{33}^{d} \end{aligned} \tag{D.1}$$

Strain compatibility requires

$$\begin{aligned} &\Delta L^{o} = \Delta L^{d} \\ &\Rightarrow \frac{1}{E^{o}}\left(\sigma_{11}^{o} - \nu\sigma_{33}^{o}\right) + \alpha^{o}\Delta T = \frac{1}{E^{d}}\left(\sigma_{11}^{d} - \nu\sigma_{33}^{d}\right) + \alpha^{d}\Delta T \\ &\Delta w^{o} = \Delta w^{d} \\ &\Rightarrow \frac{1}{E^{o}}\left(\sigma_{33}^{o} - \nu\sigma_{11}^{o}\right) + \alpha^{o}\Delta T = \frac{1}{E^{d}}\left(\sigma_{33}^{d} - \nu\sigma_{11}^{d}\right) + \alpha^{d}\Delta T \end{aligned} \quad , \tag{D.2}$$

where we have neglected differences in the Poisson's ratio, ν.

Solving for the stresses

$$\sigma_{11}^{o} = -\sigma_{11}^{d} = \Delta\alpha\Delta T E\frac{(1+\nu)}{(1-\nu^2)}$$
$$\sigma_{33}^{o} = -\sigma_{33}^{d} = \Delta\alpha\Delta T E\frac{(1+\nu)}{(1-\nu^2)}, \tag{D.3}$$

where

$$\Delta\alpha = \alpha^{d} - \alpha^{o} \text{ and } E = \frac{E^{o}E^{d}}{E^{o}+E^{d}}. \tag{D.4}$$

II. Superimpose bending strains.

Can define a neutral bending axis (where stresses are zero):

$$\bar{x}_2 = h\left(\frac{1+\frac{1}{2}\left(1+\frac{E^{d}}{E^{o}}\right)}{1+\frac{E^{d}}{E^{o}}}\right), \tag{D.5}$$

then the bending strains can be written in terms of an imposed curvature, κ, as

$$\varepsilon_{11}^{o} = \frac{\sigma_{11}^{o}}{E^{o}} + \kappa(x_2 - \bar{x}_2) = \frac{A}{E^{o}} + \kappa(x_2 - \bar{x}_2)$$
$$\varepsilon_{11}^{d} = \frac{\sigma_{11}^{d}}{E^{d}} + \kappa(x_2 - \bar{x}_2) = \frac{-A}{E^{d}} + \kappa(x_2 - \bar{x}_2) \tag{D.6}$$

where

$$A = \Delta\alpha\Delta T E\left(\frac{1+\nu}{1-\nu^2}\right). \tag{D.7}$$

III. Minimize strain energy with respect to curvature, κ.

The strain energy from strain along the x_1-direction is given by

$$U = U^d + U^o = \frac{1}{2}E^d \int_0^h (\varepsilon_{11}^d)^2 dx_2 + \frac{1}{2}E^o \int_h^{2h} (\varepsilon_{11}^o)^2 dx_2 . \tag{D.8}$$

Substituting in the strain components,

$$\begin{aligned} U^d &= \frac{E^d}{2}\left[\left(\frac{A}{E^d}\right)^2 h - \left(\frac{A}{E^d}\right)\kappa\left((h-\bar{x}_2)^2 - \bar{x}_2^2\right) + \frac{\kappa^2}{3}\left((h-\bar{x}_2)^3 - \bar{x}_2^3\right)\right] \\ U^o &= \frac{E^o}{2}\left[\left(\frac{A}{E^o}\right)^2 h + \left(\frac{A}{E^o}\right)\kappa\left((2h-\bar{x}_2)^2 - (h-\bar{x}_2)^2\right) + \frac{\kappa^2}{3}\left((2h-\bar{x}_2)^3 - (h-\bar{x}_2)^3\right)\right] \end{aligned} . \tag{D.9}$$

Minimize with respect to curvature by setting

$$\frac{\partial U}{\partial \kappa} = 0. \tag{D.10}$$

Solving for the curvature and simplifying gives

$$\kappa = \frac{3}{2}\frac{\left[2(h-\bar{x}_2)^2 - \bar{x}_2^2 - (2h-\bar{x}_2)^2\right]E^{(1+\nu)}/(1-\nu^2)}{E^o\left[(2h-\bar{x}_2)^3 - (h-\bar{x}_2)^3\right] + E^d\left[(h-\bar{x}_2)^3 + \bar{x}_2^3\right]}\Delta\alpha\Delta T. \tag{D.11}$$

In general this gives a constant times $\Delta\alpha\Delta T$. In the special case where

$$E^o = E^d, \tag{D.12}$$

the curvature simplifies to

$$\kappa = -\frac{3}{4(1-\nu)h}\Delta\alpha\Delta T. \tag{D.13}$$

Furthermore, if we let ν=0.25 then we simply get

$$\kappa = -\frac{\Delta\alpha\Delta T}{h}. \text{ (downward curvature set positive)} \tag{D.14}$$

Now if we use an optical lever as shown in Figure 2, then the beam deflection angle is given by

$$\theta = \kappa L = \frac{L}{h}\Delta\alpha\Delta T. \tag{D.15}$$

The deflection of the optical beam is then

$$\delta = D\tan\theta \cong D\theta = \left(\frac{D}{h}\right) L\Delta\alpha\Delta T \text{ (for postive curvature up in Figure D.2).} \quad \text{(D.16)}$$

For free strips the thermal expansion difference is $L\Delta\alpha\Delta T$. Therefore, the bi-metallic strip and optical lever arrangement amplifies the observed displacement by $\left(\frac{D}{h}\right)$.

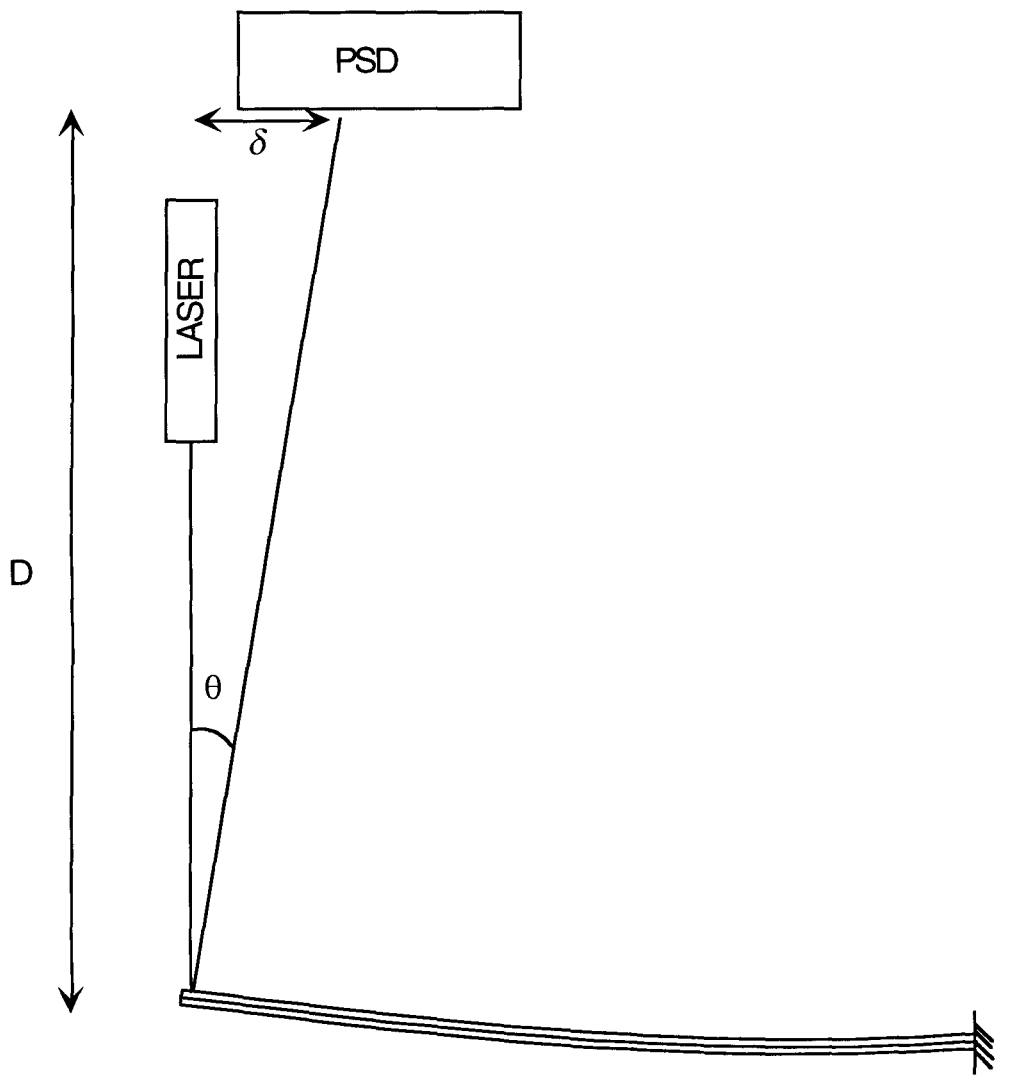

Figure D.2. Optical lever.

Appendix E Mathcad file for calculating microstrain from Peter Stephens' coefficients (orthorombic case only)

Lattice parameters:

$a := 2.909 \qquad b := 5.849 \qquad c := 5.043$

$\alpha := 90 \cdot \frac{\pi}{180} \qquad \beta := 90 \cdot \frac{\pi}{180} \qquad \gamma := 90 \cdot \frac{\pi}{180}$

Inverse metric tensor:

$$f := \begin{bmatrix} a^2 & a \cdot b \cdot \cos(\gamma) & a \cdot c \cdot \cos(\beta) \\ a \cdot b \cdot \cos(\gamma) & b^2 & b \cdot c \cdot \cos(\alpha) \\ a \cdot c \cdot \cos(\beta) & b \cdot c \cdot \cos(\alpha) & c^2 \end{bmatrix} \qquad G := f^{-1}$$

$$ca := \frac{G_{1,2}}{\sqrt{G_{1,1} \cdot G_{2,2}}} \qquad sa := \sqrt{(1 - ca^2)}$$

Define crystal to cartesian transformation matrix:

$$A := \begin{bmatrix} a & 0 & 0 \\ 0 & b & 0 \\ 0 & 0 & c \end{bmatrix} \qquad B := \begin{bmatrix} 1 & 0 & 0 \\ \cos(\gamma) & sa \cdot \sin(\gamma) & -ca \cdot \sin(\gamma) \\ \cos(\beta) & 0 & \sin(\beta) \end{bmatrix} \qquad L := (A \cdot B)^T$$

Define d-spacing: $M(H) := \left| H \cdot G \cdot H^T \right|$

Enter Shkl coefficients:

$S400 := 1.1 \qquad S040 := .22 \qquad S004 := .23 \qquad S220 := -.33 \qquad S202 := .44 \qquad S022 := -.086$

Define Peter Stephen's function for microstrain broadening:

$$\sigma M(H) := \left| \begin{array}{l} h \leftarrow H_{0,0} \\ k \leftarrow H_{0,1} \\ l \leftarrow H_{0,2} \\ S400 \cdot h^4 + S040 \cdot k^4 + S004 \cdot l^4 + 3 \cdot \left(S220 \cdot h^2 \cdot k^2 + S202 \cdot h^2 \cdot l^2 + S022 \cdot k^2 \cdot l^2\right) \end{array} \right.$$

The H dependent strain is (in units of 10^-6):

$$\text{difC} := 16532.8 \qquad S(H) := \frac{\sqrt{\sigma M(H)}}{M(H)\cdot \text{difC}}$$

$$i := 0, 1 .. 60 \qquad \phi_i := 6\cdot i\cdot\frac{\pi}{180} \qquad j := 0, 1 .. 60 \qquad \psi_j := 3\cdot j\cdot\frac{\pi}{180}$$

$$X_{i,j} := \sin(\phi_i)\cdot\sin(\psi_j) \qquad Y_{i,j} := \cos(\phi_i)\cdot\sin(\psi_j) \qquad Z_{i,j} := \cos(\psi_j)$$

$$I_{i,j} := \left[X_{i,j} \quad Y_{i,j} \quad Z_{i,j}\right]\cdot L \qquad P_{i,j} := S(I_{i,j})\cdot 10^6$$

$$X_{i,j} := (X)_{i,j}\cdot P_{i,j} \qquad Y_{i,j} := Y_{i,j}\cdot P_{i,j} \qquad Z_{i,j} := (Z)_{i,j}\cdot P_{i,j}$$